BENHA UNIVERSITY
SHOUBRA FACULTY OF ENGINEERING

Effect of Winglet on Wind Turbine Performance and Wake Characteristics

A thesis
Submitted for the Degree of Doctor of Philosophy
In
Mechanical Power Engineering

By
MINA GAMAL MOURAD
M. SC. In Mechanical Engineering

Presented to
Shoubra Faculty of Engineering
Benha University

SUPERVISED BY
Prof. Dr.
SAMIR SOBHY AYAD
Mechanical Engineering department, Shoubra Faculty of Engineering,
Benha University

Prof. Dr.
OSAMA EZZAT ABDELLATIF
Mechanical Engineering department, Shoubra Faculty of Engineering,
Benha University

Prof. Dr.
TAREK ABDELMALAK MEKHAIL
Mechanical Engineering department, Faculty of Engineering,
Aswan University

Dr.
IBRAHIM MAHMOUD MOHAMED MOHAMED SHAHIN
Mechanical Engineering department, Shoubra Faculty of Engineering,
Benha University

2020

Abstract

Winglet (WL) has recently been used to improve the performance of horizontal axis wind turbine (HAWT). The WL geometry is a key parameter for diverging blade tip vortices away from turbine blades and reducing their induced drag. The present study focuses on the effect of winglet height (H) and toe angle (α_w) on the turbine performance and turbine wake characteristics. Both computational and experimental investigations are carried out.

The performance of a three-bladed rotor of 1m diameter with SD8000 aerofoil is numerically investigated using ANSYS 17.2 CFD on a polyhedral mesh. The model is hence validated by comparing results for power coefficient (C_{pw}) with experimental values available in the literature. The pressure coefficient (C_p) results around blade aerofoil are compared to those of the literature. Four upwind WLs with different values of H are considered while keeping α_w constant at 0^o. The winglet of H=0.8%R is proved to be the best height for performance enhancement. It increases C_{pw} by 2.4% at tip speed ratio λ=7.

The toe angle effect is studied for upwind and downwind WLs while keeping H=0.8%R. The results show that C_{pw} increases as α_w increases up to $\alpha_w=+20^o$ at all values of λ. C_{pw} increases by 6% at λ=7. Downwind WL always reduces C_{pw}. The present results are well explained by the resulting vectors map near the blade tip. Using WL with the optimum H and α_w, causes 6% increase in C_{pw} as compared to rotor blades without WL.

The effects of four selected WLs namely H=8%R, H=0.8%R (α_w=0), $\alpha_w=+20^o$ and $\alpha_w=-30^o$ (H=0.8%R) on the wake up to X/R=5.4 downstream of the turbine are studied numerically at λ=7. The optimum WL (H=0.8%R and $\alpha_w=+20^o$) increases the velocity deficit in the mixing region as a result of thrust increase. It produces higher Reynolds's shear stress and wider mixing region by comparison to the other WLs. The results prove that optimum winglet plays crucial role in wake re-energizing process.

Experiments are performed using free-jet wind tunnel and three-dimensional printed model with the same CFD model dimensions. Four samples of WLs are manufactured for the experimental study. The WL of $\alpha_w=+20^o$ shows experimentally the same percent of power enhancement (6% at λ=7) that is previously predicted by the present CFD.

Acknowledgments

I would like to thank God for giving me an opportunity to pursue my Ph. D. degree in Mechanical Engineering.

I would like to thank my supervisor, Prof. Dr. Samir Sobhy Ayad, Professor of Mechanical Engineering, for his deep interest in the subject of this research, his guidance, revision, discussions and encouragement throughout this work.

I would like to thank my supervisor, Prof. Dr. Osama Ezzat Abdellatif, Professor of Mechanical Engineering, for his help, revision and encouragement throughout this work.

I would like to thank my supervisor, Prof. Dr. Tarek Abdelmalak Mekhail, Professor of Mechanical Engineering, for his encouragement throughout this work.

I would like to thank my supervisor, Dr. Ibrahim Shahin, Lecturer of Mechanical Engineering for his help in modelling the work by CFD and for selecting the suitable method of solution.

I would like to thank Eng. Abanoub Zaki, Demonstrator in Mechanical Engineering Department for his help and encouragement in the experimental work.

My special thanks to my parents and my wife for their encouragement to achieve the present work.

Table of contents

List of figures

List of tables

Nomenclatures

Symbols

A	Rotor swept area	m^2
a	Axial induction factor	
a'	Tangential induction factor	
C	Chord length	m
C_d	Drag coefficient	
C_L	Lift coefficient	
C_p	Pressure coefficient	$\frac{P - P_\infty}{0.5\ \rho\ U_\infty^2}$
C_{pw}	Power coefficient	
C_{pw}^{drag}	Drag power coefficient	
C_{pw}^{lift}	Lift power coefficient	
C_T	Thrust coefficient	
D	Rotor diameter	m
F	Axial thrust force	N
H	Winglet height	m
I	Electrical current	A
K	Turbulent kinetic energy	m^2/s^2
N	Rotor rotational speed	r.p.m
P_d^+	Pressure upstream actuator disc	Pa
P_d^-	Pressure downstream actuator disc	Pa
P_{elec}	Electrical power	W
P_{sh}	Shaft power	W
P_∞	Free-stream pressure	Pa
R	Rotor radius	m
Re	Reynolds number	
r	Radial distance from rotor axis	m
T_{net}	Net torque	N.m
T_{lift}	Lift torque	N.m
T_{drag}	Drag torque	N.m
U_∞	Free-stream velocity	m/s
U_d	Axial flow velocity at actuator disc	m/s

U_w	Axial flow velocity at wake	m/s
V	Electrical voltage	V
V_i'	Fluctuations in velocity	m/s
$\overline{V}_i$	Time averaged velocity	m/s
WC_{pw}	Power coefficient uncertainty	
WI	Electrical current uncertainty	A
WU_∞	Free-stream velocity uncertainty	m/s
WV	Electrical voltage uncertainty	V
X	Downstream distance from rotor	m

Abbreviations

ABS	Acrylonitrile Butadiene Styrene
AD	Actuator Disc
AL	Actuator Line
APG	Adverse Pressure Gradient
BC	Boundary Conditions
BEMT	Blade Element Momentum Theory
CAD	Computer Aided Design
CFD	Computational Fluid Dynamics
DC	Direct Current
GDP	Gross Domestic Product
DTU	Technical University of Denmark
HAWT	Horizontal Axis Wind Turbine
IRENA	International Renewable Energy Agency
ISES	Integrated Sustainable Energy Strategy
LES	Large Eddy Simulation
LSV	Laser Sheet Visualization
MRF	Moving Reference Frame
NREA	New and Renewable Energy Authority
NREL	National Renewable Energy Laboratory
PIV	Particle Image Velocimetry
PLA	Polylactic Acid

PVC	Polyvinyl Chloride
RANS	Reynolds Averaged Navier-Stokes
RMIT	Royal Melbourne Institute of Technology
RSM	Reynolds Stress Model
SST	Shear Stress Transport
UPVC	Unplasticized Polyvinyl Chloride
VAWT	Vertical Axis Wind Turbine
WL	Winglet
3D	Three Dimensional
2D	Two Dimensional

Greek letters

α	Angle of attack		
α_w	Winglet toe angle		
λ	Tip speed ratio	$\frac{\Omega R}{U_\infty}$	
λ_r	Local speed ratio	$\frac{\Omega r}{U_\infty}$	
ρ	Air density		kg/m^3
ϕ	Azimuth angle (Phase angle)		
Ω	Rotor angular velocity		s^{-1}
ω	Vorticity		s^{-1}

Chapter 1

Introduction

Global warming and fossil fuel emissions are the main drive and motivation for finding alternative sources of energy. Wind energy is one of the most viable alternative energy sources. Egypt is one of the most promising countries in the fields of renewable energy production, due to its favorable climate and special geographical location. It is the most populous country in North Africa and Arab region and home to one of the fastest-growing populations globally. The rabidly increasing number of habitants has led to rapid increase in energy demand.

Economic development of Egypt depends on the energy sector. It represents 13.1% of overall gross domestic product (GDP). The Egyptian government has acted on energy diversity strategy to meet the energy demand. It is the Technical Assistance to Support the Reform of the Energy Sector for Egypt (TARES) and made up to 2035 to ensure the steady stability of energy supply. Development of renewable energy and energy efficiency is the main part included in the strategy of TARES [1].

The installed capacity of renewable energy is 3.7 gigawatts (GW), including 2.8 GW of hydropower and about 0.9 GW of solar and wind energies in 2018. The Egyptian government has defined renewable energy targets of 20% of the electricity production by 2022 and 42% by 2035 as specified in the TARES [1].

International Renewable Energy Agency (IRENA) performed an accurate assessment of the country preparation to face the challenges and to achieve the mentioned targets by ISES. Based on REmap analysis, IRENA found that Egypt has the potential to supply 53% of its electricity from renewable energy by 2030.

1.1 Wind Energy in Egypt

Egypt is endowed with many wind energy resources, especially in the Gulf of Suez area according to Egypt’s Wind Atlas. It is one of the best locations in the world for harvesting wind energy due to its high stable wind speeds with average value around 10 m/s at a height of 200 m.

Beni Suif, Menya and El Kharga oasis are new discovered areas with average wind speed between 5 and 8 m/s and suitable for electricity production and water pumping. Figure 1.1 represent wind speeds in Egypt that measured at resolution of 1 km and a height of 200 m.

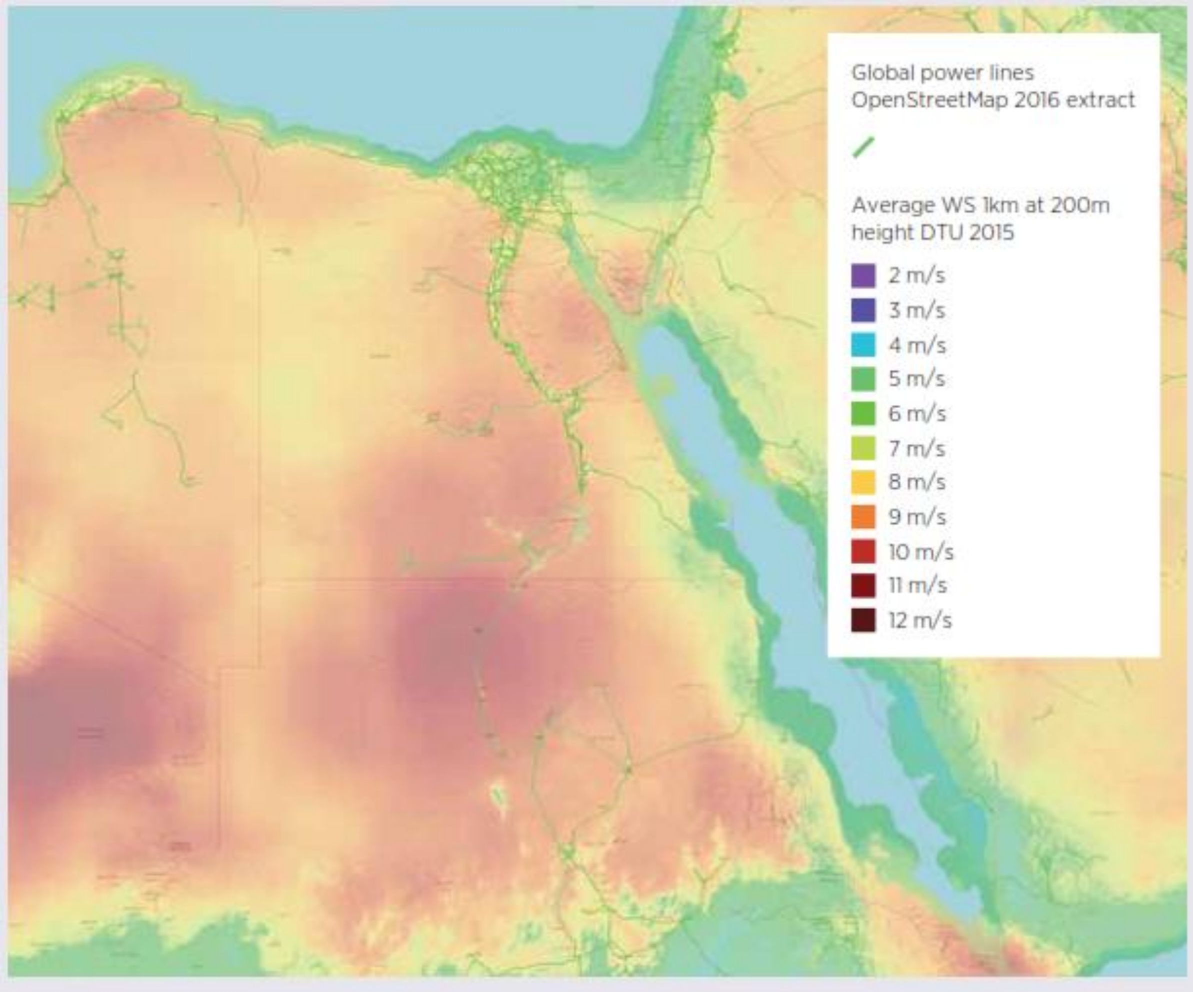

Figure 1.1: DTU Global Wind Dataset 1 km onshore wind speed at 200 meters height [1]

West coast of Red Sea shows wind speeds range between 8 and 10 m/s. Therefore the first wind farm in Egypt was established in Hurghada in 1993 with 42 units of different technologies and a total capacity of 5.2 MW. National Renewable Energy Authority (NREA) has established large scale wind farms since 2001 that with total capacity 545 MW increased to 750 MW in 2015 in both of Zaafarana (545 MW) and Gulf of El Zayat (220 MW).

1.2 History of Wind Turbines

Ancient Egyptians have used harvested wind previously in moving sail boats. Wind energy was used to move sail boats that carried huge rocks along Nile River to build pyramids. It had been also employed in more complicated machines to drive millstones to grind grains during the period of 900- 500 B.C as shown in Figure 1.2, [2]. Wind is a strong sustainable source of energy which can be converted to mechanical and electric energy by wind turbines.

Figure 1.2: Wind mills for grains grinding used by Persians [2]

Wind turbines are developed from grinding grains to electricity generation. In Denmark in 1891, Poul La Cour designed the earliest wind turbine which is considered the first device that produced electricity from wind as shown by Figure 1.3. Nowadays, daily electricity for more than 4500 homes can be generated by one turbine like Enercon E-126. It can generate 7 Megawatts of electric power at the rated wind speed.

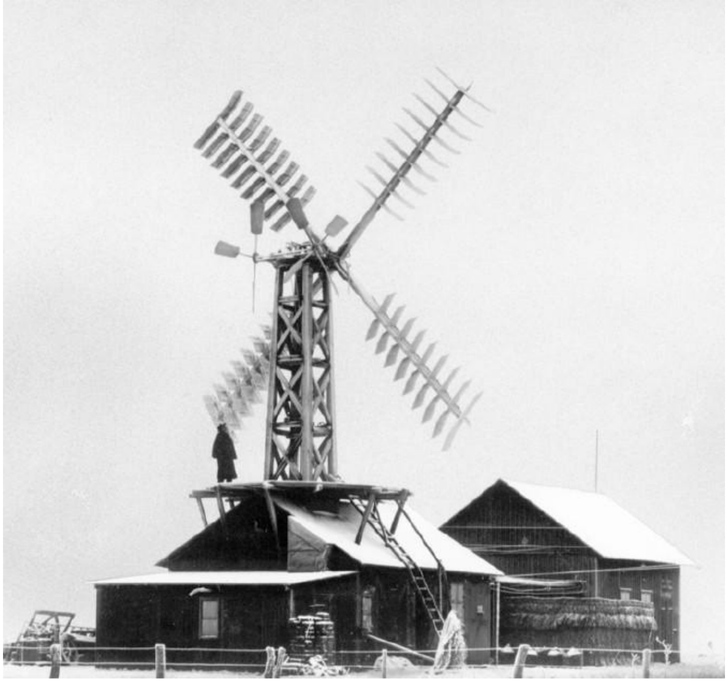

Figure 1.3: Poul La Cour's first electricity producing wind turbine in 1891 in Askov, *Denmark* [3]

Wind turbines are used in all over the world in large areas in the form of wind farms. Wind farms are classified into offshore and onshore wind farms. Offshore wind turbines are constructed at sea to obtain wind without any obstructs. They can be constructed with bigger sizes in order to harvest more energy. Offshore wind turbines have relatively higher initial cost beside electric transmission difficulty. Onshore wind turbines have relatively lower initial costs by comparison to offshore wind turbines. They can by constructed easily on long coasts in short time. The short distance between farms and customers allow for less voltage drops and shorter cables, however they may produce more noise for near communities.

1.3 Wind Turbine Orientation

Wind turbines can be classified into vertical axis and horizontal axis wind turbines according to their axis rotational orientation as shown by Figure 1.4. One of vertical axis wind turbine (VAWT) advantages that it can work without yaw system. Most of VAWTs are with constant chord and without twist and accordingly are easy to construct [4]. Gear box, brake and generator are located on the ground which make it's installation easier. HAWT is easier in aerodynamics control such as pitch angle variation and aerodynamic brake. It can harvest higher wind speeds due to it's high elevation from ground. Therefore, the overall efficiency of HAWT is higher than VAWT.

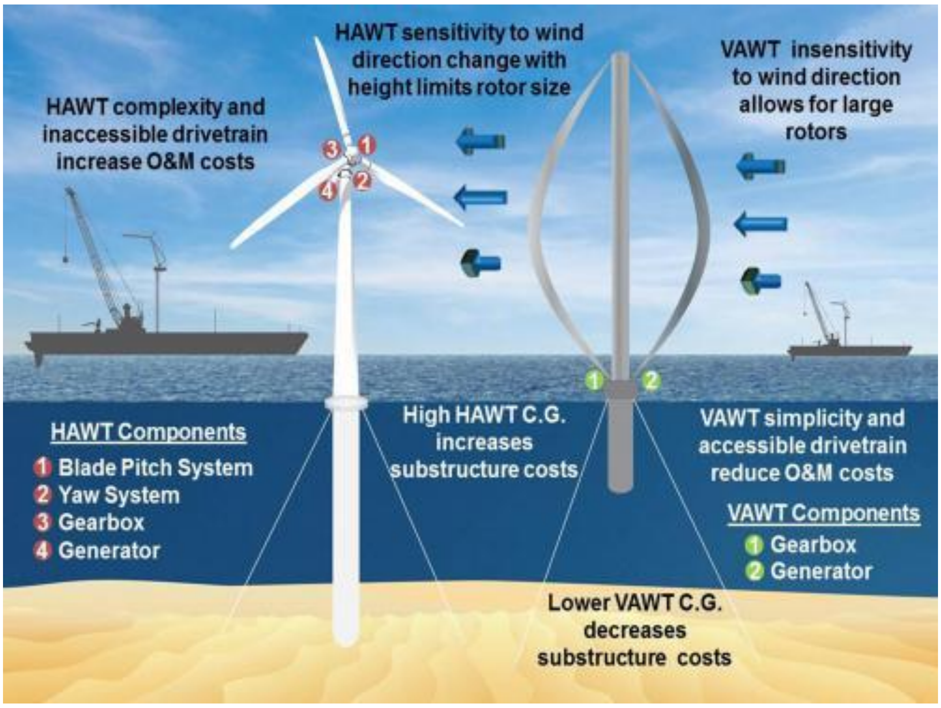

Figure 1.4: Wind turbines orientations [5]

1.4 Wind Turbine Aerodynamics

1.4.1 The Actuator Disc Concept

Actuator Disc Concept is the first concept that is used to describe aerodynamic behavior of flow over wind turbine without considering any specific design. Actuator disc is a theoretical general device that can extract energy from the flow as shown in Figure 1.5. It considers the stream tube made by stream lines that bound the turbine disc. The stream tube upstream the disc has smaller cross-sectional area than that of the disc. It expands downstream the disc and forms larger cross-sectional area far downstream the disc. The expansion occurs to satisfy the mass conservation equation. The turbine disc reduces the average velocity along the stream tube. The mass of air which passes through the stream tube is $\rho A U$ where ρ is air density, A is the cross-sectional area and U is the flow velocity.

$$\rho A_\infty U_\infty = \rho A_d U_d = \rho A_w U_w \qquad (1.1)$$

The symbols ∞, d and w refer to flow conditions at far upstream, the disc and far wake respectively.

Axial velocity variation induced by the action of the actuator disc is expressed by the axial flow induction factor (a) that is defined by Eq. (1.2). Therefore, the stream-wise velocity component of the induced flow at turbine disc becomes (1-a) U_∞.

$$U_\mathrm{d} = U_\infty \,(1 - a) \qquad (1.2)$$

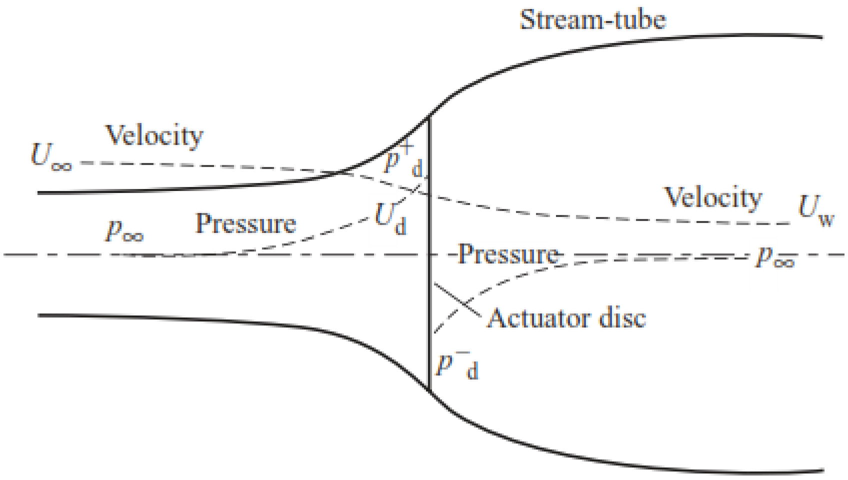

Figure 1.5: Extracted energy by actuator disc and stream tube [6]

The overall change in air velocities of the stream tube (U_∞ - U_w) produces a rate of change of momentum that is given by

$$\text{Rate of change of momentum} = \rho A_d U_d (U_\infty - U_w) \tag{1.3}$$

The thrust force on the turbine disc equals the rate of change of momentum and is given by Eq. (1.4). Therefore, pressure drop across the actuator disc causes the rate of change of momentum force.

$$(p_d^+ - p_d^-)A_d = (U_\infty - U_w)\rho\, A_d\, U_\infty\,(1-a) \tag{1.4}$$

Bernoulli's equation is applied to upstream and downstream sections of the stream-tube separately to obtain the pressure difference.

For upstream section it gives;

$$\frac{1}{2}\,\rho_\infty U_\infty^2 + p_\infty = \frac{1}{2}\,\rho_d U_d^2 + p_d^+ \tag{1.5}$$

Assuming that the flow is incompressible ($\rho_\infty = \rho_d$).

$$\frac{1}{2}\,\rho U_\infty^2 + p_\infty = \frac{1}{2}\,\rho U_d^2 + p_d^+ \tag{1.6}$$

For downstream section it gives;

$$\frac{1}{2}\,\rho U_w^2 + p_\infty = \frac{1}{2}\,\rho U_d^2 + p_d^- \tag{1.7}$$

By subtracting Eq. (1.7) from Eq. (1.6),

$$p_d^+ - p_d^- = \frac{1}{2}\,\rho(U_\infty^2 - U_w^2) \tag{1.8}$$

Substitute by Eq. (1.8) in Eq. (1.4),

$$\frac{1}{2}\,\rho(U_\infty^2 - U_w^2)\,A_d = (U_\infty - U_w)\,\rho A_d U_\infty\,(1-a) \tag{1.9}$$

And

$$U_d = \frac{U_\infty + U_w}{2} \tag{1.10}$$

And thus,

$$U_w = (1-2a)U_\infty \tag{1.11}$$

Power coefficient (C_{pw}) is defined as the ratio between the actual power extracted from wind and the theoretical power can be extracted from a wind stream of area equals the turbine disc and velocity U_∞.

$$C_{pw} = \frac{Power}{\frac{1}{2}\rho U_\infty^3 A_d} \tag{1.12}$$

Power extraction from air can be calculated from the concentrated force at the actuator disc. Where the work done by the force is FU_d.

The force F can be calculated by Eq. (1.4) and by the substitution of Eq. (1.11),

$$F = (p_d^+ - p_d^-)A_d = 2\,\rho\, A_d\, U_\infty^2\, a\,(1-a) \tag{1.13}$$

While$U_d = (1-a)U_\infty$,

The force on the actuator disc due to the pressure difference before and after the disc that given by Eq. (1.13) can be normalized to calculate the thrust coefficient (C_T).

$$C_T = \frac{F}{\frac{1}{2}\rho U_\infty^2 A_d} \tag{1.14}$$

$$C_T = 4a(1-a) \tag{1.15}$$

$$Kinetic\ power\ extracted = \frac{1}{2}\,\rho\, A_d U_d\,(\,U_\infty^2 - U_w^2) \tag{1.16}$$

From Eq. (1.12),

$$C_{pw} = 4a(1-a)^2 \tag{1.17}$$

Betz limit is the maximum value of C_{pw} can be obtained from the actuator disc, it occurs when,

$$\frac{dC_{pw}}{da} = 4(1-a)(1-3a) = 0$$

Which gives the maximum value at $a = \frac{1}{3}$

Hence,

$$C_{pw\,max} = \frac{16}{27} = 0.593 \tag{1.18}$$

The maximum value of power coefficient that can be achieved is known as Betz limit and equals to 0.593. There is no horizontal axis wind turbine that exceeds that limit. Betz limit isn’t based on a special design for wind turbine, while it depends on the stream tube expansion.

1.4.2 Local and Tip Speed Ratios (λ_r and λ)

The ratio between tangential velocity of the blade at any radius and the far upstream velocity (U_∞) is called Local Speed Ratio (λ_r). While Tip Speed Ratio (λ) is the ratio between blade tip tangential velocity and the far upstream velocity (U_∞).

$$\lambda_r = \frac{\Omega\, r}{U_\infty} \tag{1.19}$$

$$\lambda = \frac{\Omega\, R}{U_\infty} \tag{1.20}$$

Tip speed ratio variation for wind turbines affects the power coefficient values. The power coefficient has minimum values at lower and higher tip speeds ratios as shown in Figure 1.6. It is preferred to let turbine work in optimized focused area of tip speed ratios.

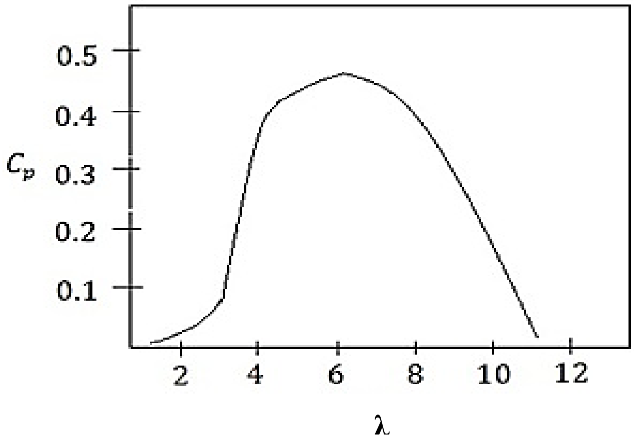

Figure 1.6: Variation of C_{pw} against λ [7]

At lower λ values, the angle of attack (α) is high which causes the stall phenomena for the flow. It isn't a desirable phenomenon where the flow passes over the blade with less interaction and thus less power production therefore, C_{pw} will decrease. The power coefficient decreases at higher tip speed ratios due to low angle of attack that increases drag effect and reduces lift.

Thrust coefficient increase by increasing λ. The disc acts as a solid body at higher values of λ that obstruct the air to move through the rotor. The flow moves around the disc and causes separation behind the disc. It is similar to that occurred in solid disc condition. Figure 1.7 shows the increase in C_T with λ increase in addition to a slight inflection in the curve. The inflection refers to the transition of the turbine between stalled and optimal conditions.

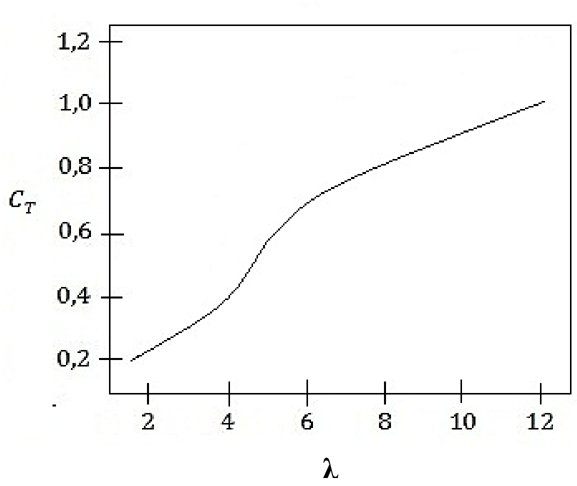

Figure 1.7: Variation of C_T against λ [7]

The extracted energy from air actually depends on the turbine design and number of the blades. Wind turbines are machines with number of rotating blades with angular velocity Ω about the turbine axis. The rotating blades with special design are responsible for the pressure difference across the rotor plane. The pressure difference is responsible for the decrease of axial momentum and of the energy transfer to turbine rotor. The torque on the turbine blades is exerted by the flow passing through it. A reaction torque acts on the flow causing it to rotate in an opposite direction of turbine rotation.

1.4.3 Wake Development

The wake can be divided into two sections, near and far wake. The transition area between the two divisions is approximately one rotor diameter downstream the rotor [8]. Flow field in the near wake is determined by the geometric properties of the rotor. Far wake region is less effected by the rotor design.

The actuator disc theory assumes that the wake is surrounded by control surface that separates the free-stream from the wake flow. Actually, a shear layer is created between the wake and free-stream due to velocity difference. The diameter of the far wake region is increased by the expanded shear layer as shown in Figure 1.8. For high rotor loading, a considerable amount of wind kinetic energy is converted into large scale turbulent motion. The turbulence in the wake is an efficient mixer. It mixes the low velocity fluid in the wake with high velocity fluid outside the wake. The wake expands and the velocity deficit is reduced.

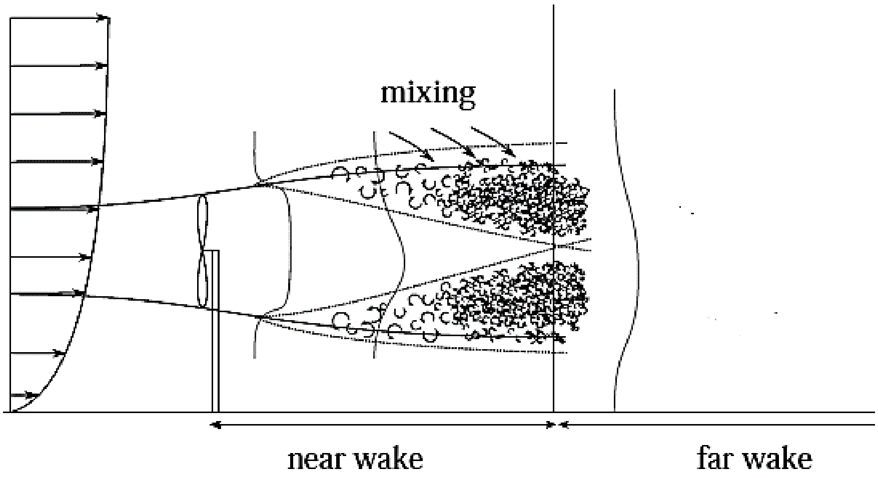

Figure 1.8: Transition between the near and far wake [8]

1.4.4 Wake Rotation

The torque effect on the rotor disc by flow passing through it needs and equal and opposite torque affects the air. Air in the wake rotates in a direction opposite to that of the rotor as a result of the reaction torque. The air in the wake gains angular momentum therefore, it has tangential velocity component as well as the axial component.

The exit flow from the disc rotates and remains in constant rotation while the entering flow hasn’t rotational motion at all. The transfer of rotational motion to the fluid occurs through the rotor thickness as shown in Figure 1.9. The change in tangential velocity is described by tangential induction factor (a`). The tangential velocity downstream the disc is 2Ωra`. The induced tangential velocity at the plane of rotation at a radial position r from the axis of rotation is Ωra`.

The flow is accelerating in the tangential direction as it is squeezed between the blades as shown in Figure 1.10. The rotation effect increases as the separation between blades is reduced, while the solid blockage that presented by the blades is increased.

1.4.5 Angular Momentum Theory

Tangential velocity and axial induced velocity aren’t the same for all radial positions. Aerodynamic analysis should be performed at an annular ring with radius r and radial width δr of the rotor disc in order to let velocities variation considered.

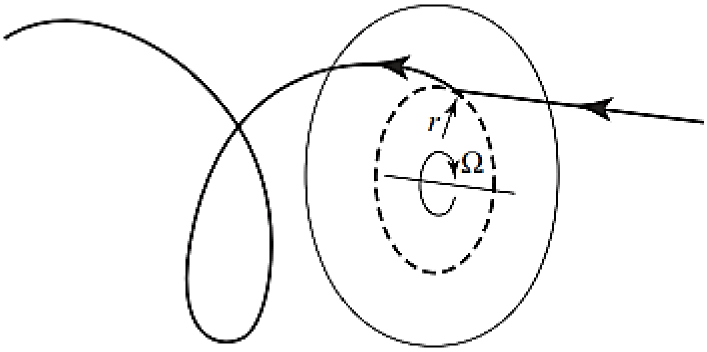

Figure 1.9: The trajectory of an air particle passing through the rotor disc [6]

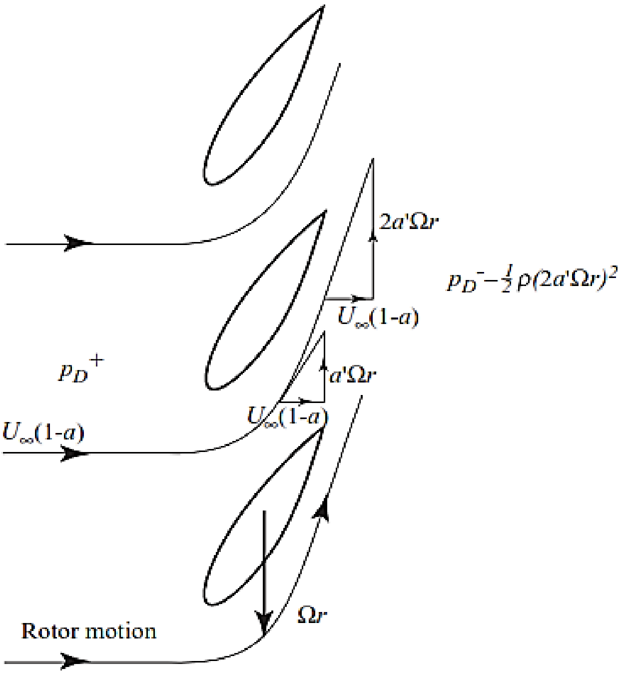

Figure 1.10: Tangential velocity grows across the disc thickness [6]

Imparting the tangential velocity component and reduction in axial velocity are result of the rotor torque and axial force increase respectively. The disc is divided into multiple rings.

The torque at each ring (δQ) equal to the rate of change of angular momentum of air passing through it.

$$\delta Q = \rho\, \delta A_d U_\infty (1 - a) 2\Omega a' r^2 \tag{1.21}$$

Where δA_d is taken to be the annular ring area

$$\delta P_{sh} = \delta Q \Omega \tag{1.22}$$

1.4.6 Blade Element Momentum Theory

Blade Element Momentum Theory (BEMT) is the most common analysis method used for wind and water turbines. According to BEMT assumptions, the rate of change of momentum of air passing through the annulus area created by blade element is a result of the force produced by the blade element. There isn't interference between the blade elements. The induced velocity effects near the tip and hub of the wind turbine rotor can be modelled by the Prandtl tip and hub loss models [6]. The extracted power augmentation means like winglets, flaps and blade tip geometry can't be modelled by BEMT.

Forces on blade elements at a given values of a and a` can be determined by knowing the variation of C_L and C_d with angle of attack (α). Wind speed, flow factors and rotor rotational speed determine the angle of attack.

1.5 Aerodynamics Losses of Wind Turbine

Small scale wind turbine swept area is small to extract more energy from wind. That causes a sensible reduction in the overall power generation. Tip loss is one of the main important losses that affect the power production. Blade tip behavior should be studied in order to understand the losses reasons. At first, the main concept of HAWT operation is aerodynamic lift force generation on the entire length of the blade. Lift force generation is a result of pressure difference between the upper and lower surfaces of the blade. At the blade tip, air moves from high pressure surface to low pressure surface and generates the tip vortex as shown in Figure 1.11. Vortex is a rotational motion of the fluid that forms strong low pressure region in the core [9].

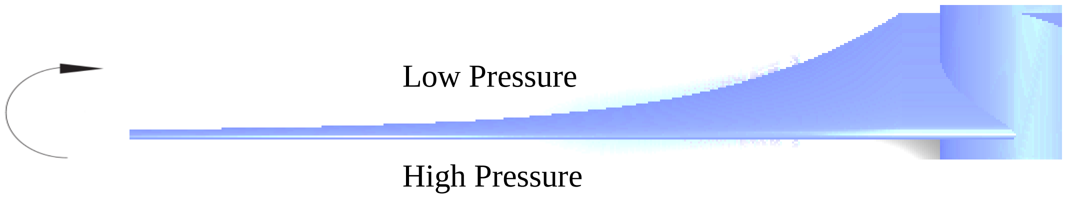

Figure 1.11: Air pressure distribution around the blade

Tip vortices are the main source of induced drag and reduction of lift force. Therefore, the concept of winglet (WL) has emerged. Its main function is to reduce the effect of wingtip vortices. These vortices are produced by pressure difference between lower and upper blade surfaces. Fluid particle traverse from higher pressure surface to lower pressure surface at blade tip thereby, the tip vortex is formed. WL shifts tip vortices away from blade tip to winglet tip or diverging them out of rotation plane. Farhan et al. [10] showed that winglet plays a crucial role in extracting more energy due to blade extension beside its influence on blade tip vortices.

1.6 Winglets Characteristics

Winglet concept was firstly used for plane wings by adding vertical surfaces to wing tip. It helps in fuel consumption reduction as a result of overall drag minimization. The main purpose of winglet is to reduce the induced drag due to tip vortices and to increase lift to drag ratio. Winglet addition to blade tip causes an additional drag which should be less than the reduction in the induced drag at the blade tip. Winglet works on tip vortex diffusion and pushes it far away from the blade tip. The pioneering research by Maughmer [11] was the first to consider the winglet as an effective passive solution for tip vortices in sailplanes. He showed that the design of WL can provide the greatest gain on overall performance and indicated that work remains to be done in finding the best tip treatment for unlimited span sailplanes. Winglet can be specified by six parameters; namely: winglet height, sweep angle, cant angle, curvature radius, toe angle and twist angle as shown in Figure 1.12.

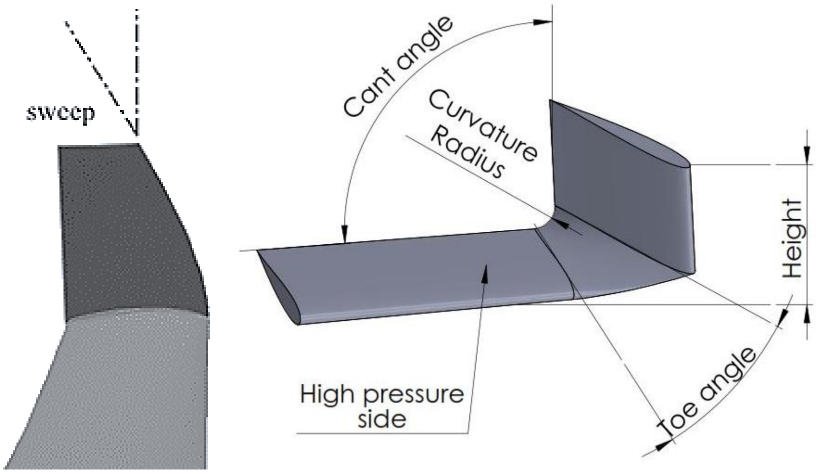

Figure 1.12: Geometrical parameters of winglet design

1.7 Thesis Layout

The thesis consists of the above introduction, literature survey, governing equations, numerical simulation, experimental procedures, results and conclusions. In addition, the list of references is also given.

Chapter 2

Literature Survey

Tip losses of wind turbine rotor are the main reason for using winglet. Tip losses don’t only appear in wind turbines or turbo-machines but they also appear in any finite blade or wing. Finite span wing theory was developed by Prandtl in the period 1911-1918 and the associated tip losses are given by Berhe [12]. Recently, many researchers investigated wind turbines performance improvements by studying aerodynamic characteristics of the blades.

2.1 Studies for the WL Effect on Rotor Performance

Many studies have been performed to study the effect of blade tip devices. Gyatt and Lissamann [13] used advanced tip devices that were used in aircraft applications. The authors performed tests on a 25kW Carter Wind Turbine in San Gorgonio Pass, California by using four winglets designs. The results of the study were compared to the analytical results of Wilson/Lissamann PROP code. In spite of the increase of produced power in the analytical study, there wasn’t sensible improvement occurred in the experimental work. The authors explained that discrepancy by the poverty of analytical and numerical methods that can predict the rotor performance and wake characteristics at that time.

A simple momentum theory for the configurations of tip winglets was developed by Van Bussel [14]. The theory mainly depended on the shift of tip vortex in downstream direction therefore, the power was augmented. The downstream extension of the winglet shifted the tip vortex. The theory showed significant power improvements at high tip speed ratios. The author tried to verify the theoretical results by experiments using MIE-vanes which was developed at MIE University in Japan at the blade tips. Imamura et al. [15] used a vortex lattice method with a free wake model to study the effectiveness of winglet on HAWT performance. Their winglet was simply an inclined extension of rotor blades. The study was a comparison between simple span extension and winglets made by cant angle variation. The results showed that adding winglet increases the generated power similar to the span extension. Free wake lifting line model is one of the used models to evaluate the effect of winglets. The model was used by Guanna and Johansen [16] and showed that downwind winglets were the most efficient. The results of the used model are validated by comparing with the CFD results of the study. A vortex cylinder analogy is performed in order to show the effect of winglet on tip losses reduction. Further numerical studies were performed by Johansen and Sørensen [17] to increase the power coefficient by using different winglets. Five winglet designs were studied by the authors and 2.8% of power coefficient was reached. It was noticed an increase in the produced power by curvature radius decrease and winglet height increase. The toe angle effect hadn't been investigated and thought to have a positive effect on the generated power. Congedo and De Giorgi [18] modeled wind turbine rotor by CFD using k-ω SST model to optimize its performance. The optimization process was performed by adding winglets and comparing the results to those of the baseline rotor. The study focused on the winglet curvature radius. It was found that the produced power increased as the winglet curvature radius increased.

Gupta and Amano [19] performed a CFD analysis for wind turbine blade using winglet. The study considered winglet bent towards high pressure side (upwind configuration) with different winglet heights and cant angles. The best design obtained was the winglet of 45° cant angle and height of 4%. It improved the generated power by about 20% as compared with power produced of straight blade.

Saravanan et al. [20] performed experimental study on small scale wind turbine to evaluate the effect of winglet curvature radius and height. The results showed that adding winglet makes the turbine start to rotate at lower wind speeds. The generated power increased by the increase of the winglet height and by the decrease of curvature radius. Gertz et al. [21] made experiments on wind turbine rotor by exchanging the outer 10% of the blade tip by winglet of cant angle 90°. The used winglet was downwind configuration and similar to the one of Gyatt and Lissamann [13]. The results showed that the power was increases by 5% to 8%.

Elfarra et al. [22] studied the blade tip tilting (winglet) by using four CFD turbulence models namely Spalart-Allmaras, Standard k-ε, k-ε Yang-Shih and SST k-ω models. The authors used four winglet configurations with height 1.5%R. The configurations were performed by tilting the blade tip extension towards high pressure side, low pressure side, leading edge and trailing edge. For the first two configurations, the authors tested the upwind and downwind configurations while for the last two configurations, the positive and negative sweep angle were tested. It was concluded that the upwind configuration produced more power and axial thrust at lower values of wind speed up to 9 m/s. Downwind configuration produced more power at higher wind speed values than 9 m/s up to 15 m/s.

Ali et al. [23] performed experimental study on a small scale wind turbine rotor to show the influence of upwind and downwind winglets on the rotor performance. The experiments were performed in RMIT industrial wind tunnel to measure the drag and lift forces produced on the blades. The results showed that lift to drag ratio increased by 26% in the case of upwind winglet while decreased by 27% in the case of downwind winglet.

Experimental flow visualization is very important to predict the flow around the blade tip. Therefore, an experimental study were done by Tobin et al. [24] to show the winglets effects of the wake and the rotor performance. The experiments were performed in wind tunnel by using Particle Image Velocimetry (PIV) to show the influence of downwind winglets. The results showed that the power and thrust coefficient increased by 8.2% and 15% respectively by use of the winglet. The tip vortex strength didn’t change significantly by the winglet effect.

Klimchenko and Jones [25] used PIV in experimental study to show the effect of winglets and serrations on the rotor performance and wake. The authors used a downwind winglet configuration. The results focused on the flow behavior around the tip and behind the rotor. The appeared tip vortices due to winglet addition were similar to those of the baseline rotor with more diffusion. There wasn’t any significant effect of the tip modifications on the time averaged velocity contours in the wake.

Recently, many researches worked on the winglet optimization for small scale wind turbines. Hansen and Mühle [26] obtained an optimized winglet shape by constructing Kiriging surrogate model. The authors used Spalart-Allmaras turbulence model to predict the turbine performance. Experiments were performed at the Norwegian University of Science and Technology wind tunnel to validate the simulated performance. The authors used three downwind winglets. The optimized one increased the turbine power and thrust by 7.8% and 6.3% respectively. The wind tunnel experiments showed that the power and thrust increases by 8.9% and 7.4% respectively. The authors found that by the wind tunnel turbulence increase the power and thrust increased by 10.3% and 14.9%. Optimization surrogate model is used by Zahle et al. [27] to optimize the blade tip for more power production. The authors compared the use of winglet with height 2% and cant angle 90° to the equivalent blade extension. They found that winglet can increase the power production by 2.6% while the ordinary blade extension increase the power by 0.76%.

The combined effect of winglet planform and airfoil on the rotor performance hasn’t been studied in the previous studies. Farhan et al. [10] focused on the combined effect of the winglet planform and airfoil. The study was performed on turbine rotor with diameter 10m in the National Renewable Energy Laboratory (NREL). The influence of the winglet was studied by using different turbulence models which validated with respect to the experimental data.

The best used design was of 15cm rectangular downwind winglet with S809 airfoil and 45^o cant angle.

Ostovan et al. [28] used PIV to show the tip vortex behavior downstream a wind turbine rotor with diameter 0.94 m. Phase-locked 2D measurements were performed for the rotor with and without downwind winglets. The measurements sheets covered 120^o of azimuthal angle of the vortex growth. The study focused on vortex convection, vortex core diameter and core expansion in addition to the induced drag on the rotor. The results showed that the wingletted rotor shifted the wake boundary radially outwards, vorticity and turbulent kinetic energy were reduced across the wake boundary. The winglets increased the tip vortex core size by about 3 times those of the baseline rotor.

Zhu et al. [29] made CFD study on the influence of downwind and upwind WLs in addition to using both of the two configurations together. The study was performed at different pitch angles of the rotor blade. The results showed that upwind WL increased the rotor power by 3.61% at λ=7 and pitch angle 15^o.While the downwind configuration increased the power by about 2.42% at the same conditions. The results showed that upwind WL was superior to the downwind WL. An opposite results were achieved at blade pitch angle of 25^o.

Khaled et al. [30] performed experimental and numerical studies to show the influence of upwind WLs with different heights and cant angles. The results showed that the power increases by the winglet height increase. The WL of height =7%R showed the maximum increase in the power coefficient by 8.28% at the design λ=5 and cant angle 90^o.

Khalafallah et al [31] carried out a numerical study by using k-ω SST turbulence model to show the effect of WL's cant angle and direction on the power coefficient. The results showed that the upwind WL with cant angle 40^o and twist angle 10^o was the best WL for power enhancement.

Most of the previous literature have shown winglet effect on both of power and thrust. Winglet effect on tip vortex and wake characteristics have been studied by limited number of researches as shown in literature [24], [25], [28]. The wake characteristics were studied in more details for rotors without tip modifications. They have been studied numerically by CFD and taking into consideration the suitable geometry and turbulence model. For experimental researches, the wake was studied by Particle Image Velocimetry (PIV) and other devices. PIV was and still the most suitable device that can explore entire the wake region without obstacles.

2.2 Studies for Wind Turbine Wakes

The wake can be divided into two regions: the near-wake and the far-wake regions as demonstrated before. The near-wake region is the region that found behind the rotor immediately. The influence of the rotor blades is more obvious at the near-wake region. The near-wake region may extend up to one rotor diameter downstream the rotor plane. The importance of near-wake region study comes from the presence of tip vortices. Their study is important because their crucial effect on the rotor vibration and noise according to Massouh and Dobrev [32]. The far wake study is important for wind turbines positioning in wind farm cases as presented by Vermeer et al. [33].

Grant et al. [34] used laser sheet visualization (LSV) technique to explore the trailing vortices trajectories. The authors carried out the experiments on a rotor of diameter 0.9 m under different conditions of turbine yaw and rotor azimuth angles. The results are compared to numerical wake model and showed the effect of the wind tunnel walls effects had to be included in the model.

Particle Image Velocimetry (PIV) was used in experimental study carried out by Xiao et al. [35] to show investigate the development of the tip vortex fir HAWT. It was noticed an inward move for the tip vortex takes short time which was followed by outward move with the wake expansion. The tip vortices propagation at the near wake had a linear expansion. Massouh and Dobrev [32] performed an experimental study on a rotor of diameter 0.5 m by using the previous technique. The study focused on the flow characteristics at the near-wake region. The vortex age from 0^o to 810^o was studied to show the vortex motion. The results were concluded in vortex core diameter, swirl velocity distribution and vortex diffusion as the vortex characteristics.

The previous flow visualization techniques produces qualitative and quantitative results and can give informations about different points at the same time. PIV and other laser techniques have high costs comparing to the other traditional techniques. It makes computational and numerical methods are developed to model the experiments considering small details in the fluid domain. The Blade Element Momentum Theory (BEMT) method, prescribed wake model, free wake model, actuator disc model (AD), actuator line model (AL) and Navier-Stokes codes are some of the models for wind turbine flow predictions as demonstrated by Snel et al. [36].

BEMT and Computational Fluid Mechanics (CFD) are the most common approaches that are used to calculate the aerodynamic forces [37]. BEMT is the basic theory of wind turbine blade design by combination between momentum theory and blade geometry. It solves set of equations at each blade element by balancing axial and angular momentum. It predict element forces, depending on lift and drag coefficients that were experimentally detected from 2D flow in wind tunnel. BEMT failed to predict the measured wind turbine torque when the wind speed is higher than 7 m/s as reported by Zhang [38]. The author referred the reason to dominant rotational effects.

The BEMT explained in chapter 1 assumes that the blade forces are constant on the annular element of the rotor. That can be applied on infinite number of blades. On other hand, finite number of blades is performed in reality. Therefore, tip loss effect is taken into consideration and Prandtl's tip loss factor is applied. Prandtl's tip loss correction is the most common one that brought BEMT closer to reality [39]. There are many others tip loss corrections [40] that are regarded as empirical corrections that depend on operating conditions such as tower effect and finite number of blades [33].

On other hand, CFD has become an admirable method in different engineering fields. It is able to solve the Navier-Stokes (N-S) equations which are based on basic different equation of mass, momentum and energy conservation. CFD can deal with different kinds of turbulence models in different conditions. It is able to show results of streamlines, velocity and pressure contours at any region around wind turbine. Latterly, CFD has become the main tool to predict performance of wind turbines. Because of its potential to model 3D effects, for instance tip vortices and wake characteristics.

Jimenez et al. [41] developed a CFD code based on a Large-Eddy Simulation (LES) approach. The turbine was simulated by concentrated drag forces, and was placed in an environment that has the same turbulence properties of the real atmosphere. The authors compared the CFD results with experimental data and analytical correlations. The CFD results were found in a good agreement with both of the experiments and the analytical correlations. Airflow around wind turbine of type ENERCON E66 was simulated by Wußow et al. [42] using LES turbulence model. The purpose of the study was to capture three-dimensional flow behind the wind turbine. It was found that the used turbulence model could provide enough data on spatial and temporal resolution to predict the loads in wake situations.

Davis [43] studied different CFD turbulence models to check their applicability for modeling wind turbine aerodynamics. At the first, the author studied the influence of turbulence models parameters variation on their performance by using different configurations of wind turbines and disks spaced at different intervals. The results showed that the grid refinement weren't enough for LES model. The RANS closure scheme didn't indicate a dominant model. The second part of the study used only the k-ω SST RANS model to simulate the wake development for an individual rotating turbine and for two inline rotating turbines. The results showed that the model were successful in wake development predicting as well as predicting velocity deficits. Vorticity results also showed an accurate wake structure.

The wind velocity distribution behind a wind turbine was predicted by a new analytical wake model which was derived by Bastankhah and Porté-Agel [44]. The wake model was derived by applying mass and momentum conservation equations as well as assuming Gaussian distribution for velocity deficit in the wake. The obtained results were compared to experimental and LES data of wind turbine wakes. It was found that the velocity deficit of the proposed new model was in a good agreement with those of experimental and LES. The new model showed more accurate power results than those of other analytical models.

Thé and Yu [45] performed simulations on wind turbine aerodynamics by hybrid RANS-LES method (HRLM). The method was used to bridge the gap between less accurate results of RANS and more computational costly LES method. The authors found that the hybrid method are better than RANS models in unsteady flow prediction.

2.3 Objective of the Study

Despite several previous studies of winglet influence. There is no agreement on the optimum winglet configuration. Winglet height is the most effective parameter that was studied in the literature. Studies [17], [22], [29] showed that smaller height WLs were enough to enhance the wind turbine power. While others [19], [23], [24], [30] found that larger height WLs were better for rotor power enhancement. The studies of winglet direction (upwind or downwind) showed different results. Most of studies in the literature [17], [19], [23], [29], [30], [31] found that upwind configurations are better for the rotor performance while few studies [18], [24], [22] found the opposite. To the author's knowledge, toe angle (α_w) hasn't been specifically studied, it is considered as the angle of attack of WL airfoil. Although increasing the toe angle causes extra drag on the winglet by itself but the objective is how successful is the whole winglet to push the tip vortex away from the turbine blade and eliminate the induced drag.

Chapter 3

Governing Equations and Turbulence model

3.1 Introduction

At the present chapter, the three-dimensional flow around modeled wind turbine rotor is studied numerically. The numerical study is performed by solving the steady, viscous and 3D governing equations (continuity and momentum) together by using k-ω SST turbulence model. Simulations are performed by ANSYS Fluent 17.2 software.

3.2 ANSYS Fluent

Fluent is a module of ANSYS software package, it solves mass and momentum conservation equations. Energy and chemical species equations can be considered in heat transfer and combustion cases. The fluent technique is based on discretized control volume hence, it is finite volume approach [46]. Simulation process takes place undergoing procedures as follows:

- Fluid domain division into discrete control volumes (Meshing Process)
- The governing equations on the discrete control volumes are integrated to construct algebraic equations for unknown variables, such as velocities, pressure and conserved scalars.
- Equations linearization and resultant linear equation system solution.

3.3 Numerical Solvers

Fluent is 2D/3D mesh solver, it considers multi grid solution algorithms. It depends two solution techniques as follows:

- Pressure-based solver
- Density- based solver

The pressure-based solver is suitable for low-speed incompressible flows while the density-based solver is suitable for high-speed compressible flows. Fluid flow in the present study is considered incompressible flow, hence the pressure-based approach is considered.

3.4 The pressure-based Solver

The pressure-based solver employs an algorithm which belongs to a general class of methods called the projection method. The constraint of mass conservation of the velocity field is achieved by solving a pressure equation. From continuity and momentum equations, the pressure equation can be derived in such a way that the velocity field which corrected by the pressure, satisfies the continuity. The governing equations are solved by iterations until the solution converges because the equations are nonlinear and coupled to one another [47]. There are three solver formulations that provided by Fluent as follows:

- Segregated
- Coupled implicit
- Coupled explicit

Implicit and explicit methods are the methods with which the governing equations are linearized with respect to the dependent variable.

- Implicit: The unknown variable in each cell is calculated using a relationship between both of existing and unknown values from neighboring cells. Hence, the unknown variable appears in more than one equation and these equations are solved simultaneously [47].
- Explicit: The unknown variable in each cell is calculated using a relationship between only existing values. Hence, each unknown variable appears in only one equation and the equations of unknown variables are solved one at a time [47].

Both of the previous methods provide accurate results for different flows. The governing equations can be solved sequentially from one another like what takes place in segregated pressure-based solver. The last algorithm is memory efficient, hence the equations are stored in the memory one at a time. The solution convergence is relatively slow in the algorithm. The pressure-based coupled algorithm solves a coupled system of equations by comprising the momentum and pressure-based continuity equations. The remaining equations (scalars) are solved in a decoupled method as in the segregated algorithm. Fluent used the segregated solver by default while it uses the coupled implicit solver instead in the cases of high-speed compressible flow, highly coupled flows with strong body forces and flows being solved on very fine mesh.

The segregated solver or the coupled explicit solver can be used in the case of insufficient memory machine instead of the coupled implicit solver. The coupled explicit solver can couple the flow and energy equations but it needs less memory than the coupled implicit solver. The coupled explicit solver usually take longer time in solution convergence than the coupled implicit solver [47].

3.5 The density-based Solver

In the density–based solver, the coupled system of equations (continuity, momentum, energy and species equations) can be solved using the coupled-explicit solver or the coupled-implicit solver. By choosing the implicit option, each equation in the coupled system can be linearized implicitly with respect to all dependent variables. Each equation in the coupled system is linearized explicitly [47].

3.6 Governing Equations

The basic equations used in Fluent are mass and momentum conservation equations in addition to the energy conservation equation if it is required. The basic equations are based on the absolute velocity formulation over the whole domain. Hence, the basic equations are expressed in a fixed frame of reference. The differential equations of laminar flow are expressed as follows [47]:

3.6.1 Mass and Momentum Conservation Equations

The mass conservation equation for steady flow is given by:

$$\frac{\partial}{\partial x_i}(\rho V_i) = 0 \qquad (3.1)$$

Where:

V_i : Velocity in the ith direction

x_i : Coordinate in the ith direction

ρ : Air density

i : Tensor indicating 1,2,3.

The momentum conservation equation in the ith direction for unsteady flow can be written as follows [47]:

$$\frac{\partial}{\partial x_j}\left(\rho V_i\, V_j\right) = \rho \bar{g}_j - \frac{\partial p}{\partial x_i} + \frac{\partial \tau_{ij}}{\partial x_j} \qquad (3.2)$$

Where: p is the static pressure, and τ_{ij} is the viscous stress tensor given by

$$\tau_{ij} = \mu\left[\frac{\partial V_i}{\partial x_j} + \frac{\partial V_j}{\partial x_i} - \frac{2}{3}\delta_{ij}\frac{\partial V_r}{\partial x_r}\right] \qquad (3.3)$$

Where:

μ : is the dynamic viscosity

i,j,r : are tensors indicates 1,2,3.

$$\delta_{ij} = \begin{cases} 1 & if \quad i = j \\ 0 & if \quad i \neq j \end{cases}$$

$\rho\bar{g}_j$ is the gravitational body force.

3.6.2 Turbulence modelling

Turbulent flow is characterized by velocity field fluctuations. The transported quantities such as momentum and energy are mixed by the fluctuation effect which fluctuates independent parameters as well. The instantaneous governing equations are time averaged to remove the small scales resulting in a modified set of equations that are computationally less expensive to be solved. The Navier-Stokes equations are transformed to such a modified form by using Reynolds's averaging.

3.6.3 Reynolds averaging of the conservation equation

In Reynolds averaging, each solution parameter $\emptyset$ in the instantaneous Navier-Stokes equations is decomposed into the mean time averaged and fluctuated components. That can be expressed mathematically as follows:

$$\emptyset = \overline{\emptyset} + \emptyset` \qquad (3.4)$$

Where $\overline{\emptyset}$ is the time averaged value of $\emptyset$ which is defined as

$$\overline{\emptyset} = \frac{1}{\Delta t}\int_{t}^{t+\Delta t} \emptyset \, dt \qquad (3.5)$$

Δt is a time scale larger than the largest time scale of turbulent fluctuations. They are assumed to be random as follows

$$\overline{\emptyset`} = 0 \qquad (3.6)$$

By substitution in the instantaneous continuity and momentum equations (3.1) and (3.2) in addition to time integration over sufficient time interval. That leads to Reynolds Averaged Navier-Stokes (RANS) equatio*ns. The continuity and momentum equations take the following form respectively* [47].

$$\frac{\partial}{\partial x_i}(\rho \bar{V}_i) = 0 \tag{3.7}$$

$$\frac{\partial}{\partial x_j}\left(\rho \bar{V}_i \bar{V}_j\right) = \rho \bar{g}_j - \frac{\partial \bar{p}}{\partial x_i} + \frac{\partial}{\partial x_j}\left[\mu\left(\frac{\partial \bar{V}_i}{\partial x_j} + \frac{\partial \bar{V}_j}{\partial x_i} - \frac{2}{3}\delta_{ij}\frac{\partial \bar{V}_i}{\partial x_j}\right)\right] + \frac{\partial}{\partial x_j}\left(-\rho \overline{V_i^{`} V_j^{`}}\right) \tag{3.8}$$

The previous two equations (3.7) and (3.8) are the same as the instantaneous continuity and Navier Stokes equations while they contain variables that represent time averaged values instead of instantaneous values. The additional term in the momentum equations (3.8) represents the effect of turbulence, namely Reynolds Stresses$\left(-\rho \overline{V_i^{`} V_j^{`}}\right)$. The function of turbulence model is to provide closure models that allow the estimation of these Reynolds stresses in terms of flow quantities.

3.7 Eddy-viscosity turbulence models

In the eddy-viscosity turbulence models, the Reynolds stresses are assumed to be proportional to the mean velocity gradients with the proportionality constant. The constant is namely turbulent viscosity and the assumption is known as Boussinesq hypothesis.

The Boussinesq hypothesis is used to relate the Reynolds stresses to the mean velocity gradients [47] as follows:

$$-\rho \overline{V_i^{`} V_j^{`}} = -\frac{2}{3}\rho K \delta_{ij} + \mu_t \left[\frac{\partial \bar{V}_i}{\partial x_j} + \frac{\partial \bar{V}_j}{\partial x_i} - \frac{2}{3}\delta_{ij}\frac{\partial \bar{V}_i}{\partial x_j}\right] \tag{3.9}$$

Where K is the turbulent kinetic energy given by

$$K = \frac{1}{2}\sum \overline{V_i^{`2}} \tag{3.10}$$

Equation (3.7) for Reynolds stresses is identical to that describes the instantaneous shear stresses (Eq. (3.3)) with the turbulent viscosity μ_t instead of the viscosityμ. Hence, the form of the Reynolds averaged momentum equation (Eq. (3.8)) remains identical to the form of laminar momentum equation (Eq. (3.2)) except that μ is replaced by and effective viscosity μ_{eff}, which can be expressed as a sum of both absolute and turbulent viscosities as:

$$\mu_{eff} = \mu + \mu_t \tag{3.11}$$

Equation (3.8) can take its final form as:

$$\frac{\partial}{\partial x_j}\left(\rho \bar{V}_i \bar{V}_j\right) = \rho \bar{g}_j - \frac{\partial \bar{p}}{\partial x_i} + \frac{\partial}{\partial x_j}\left(\tau_{ij}\right)_{eff} \tag{3.12}$$

The stress tensor $\left(\mathrm{\tau_{ij}}\right)_{eff}$ is calculated using viscosity μ_{eff} and is given by

$$\left(\tau_{ij}\right)_{eff} = \mu_{eff}\left(\frac{\partial \bar{V}_i}{\partial x_j} + \frac{\partial \bar{V}_j}{\partial x_i}\right) - \frac{2}{3}\mu_{eff}\frac{\partial \bar{V}_i}{\partial x_j}\,\delta_{ij} \tag{3.13}$$

Eddy-viscosity models approximate the effect of the turbulence on the mean motion by introducing the effective viscosity in Eq. (3.11). The eddy-viscosity models have different classes that are distinguished by the number of additional differential equations. The additional equations are solved to determine the turbulent viscosity. The turbulent viscosity is the product of the density, velocity scale and length scale as suggested by dimensional analysis. The velocity scale can be obtained by the turbulent kinetic energy. Transport equation of turbulent kinetic energy dissipation rate is the commonly used approach to determine the length scale. The rate of kinetic energy dissipation is defined as

$$\varepsilon = \nu \frac{\partial V_{\grave{i}}}{\partial x_j}\frac{\partial V_{\grave{i}}}{\partial x_j} \tag{3.14}$$

Where: ν is the kinematic viscosity

3.7.1 Turbulence model selection:

The used version of ANSYS Fluent uses different turbulence models as follows:

- Spalart-Allmaras model
- K- ε models (standard, renormalization-group(RNG), realizable)
- K-ω models (standard, shear-stress transport (SST))
- Reynolds stress models (RSM)
- Large eddy simulation (LES) model

Turbulence model choice is very important since, it significantly affects the solution accuracy. Many researches are performed to evaluate the different turbulence models for wind turbine aerodynamics prediction. It was observed that k-ω SST turbulence model is one of the most suitable models for predicting the flow physics around the wind turbine rotor. It is able to consider all three-dimensional secondary flow effects. The model gives a good predictions for the adverse pressure gradients and separating flow. The k-ω SST model is employed in the study as a result for its advantages as shown previously.

3.7.2 Shear Stress Transport (SST) k-ω model

The k-ω model is a two-equation model, one equation is for turbulent kinetic energy (k) while the second equation is for the specific turbulent dissipation rate (ω). One of the most known versions of k-ω is the Wilcox k- ω model [48]. The Wilcox model is numerically more stable than k-ε model in the viscous sub-layer near the wall. However, its results are extremely sensitive to the free-stream value of ω in free shear layer and adverse pressure gradient boundary layer flows. Hence, the k- ω model isn't the best model for wake region applications. On other hand, the k- ε model behaves better in the wake regions. Therefore, the combination between the two models is the best to model the flow characteristics near the wall and in the wake of the boundary layer as mentioned by Menter [49]. Accordingly SST *k-ω* turbulence model is considered as the most suitable model to predict aerodynamic flows.

The two transport equations of the SST model are as follow:

$$\frac{\partial \rho k}{\partial t}+\frac{\partial \rho u_j k}{\partial x_j}=\frac{\partial}{\partial x_j}\left[\left(\mu+\sigma_k \mu_t\right)\frac{\partial k}{\partial x_j}\right]+P_k-\beta^* \rho \omega \tag{3.15}$$

And

$$\frac{\partial \rho \omega}{\partial t}+\frac{\partial \rho u_j \omega}{\partial x_j}=\frac{\partial}{\partial x_j}\left[\left(\mu+\sigma_k \mu_t\right)\frac{\partial \omega}{\partial x_j}\right]+\gamma P_\omega-\beta \rho \omega^2+2(1-F_1)\rho \sigma_\omega 2\frac{\mu_t}{k}\frac{\partial k}{\partial x_j}\frac{\partial \omega}{\partial x_j} \tag{3.16}$$

β^* is a constant of value 0.09. The right hand side term of eq. (3.16) is a cross diffusion term which is activated only outside the boundary layer. F_1 is the blending function which is designed to blend the model coefficients of the original k- ω model in the boundary layer zones with the transformed k- ε model in free shear layer and free-stream zones.

The constants that appeared in Eq. (3.15) and (3.16) are expressed in a general compact form as:

$$\emptyset = F_1 \emptyset_1 - (1-F_1)\emptyset_2 \tag{3.17}$$

Where $\emptyset_1$ represents the constants that are associated with the k- ω model (when F_1 =1), and $\emptyset_2$ represents the constants that are associated with the k- ε model (when F_1 =0).

Now, γ, β, σ_k and σ_ω are defined by blending coefficients as:

- Inner model constants: $\gamma_1 = 0.5532$, $\beta_1 = 0.075$, $\sigma_{k1} = 0.5$, $\sigma_{\omega 1} = 0.5$
- Outer model constants: $\gamma_1 = 0.4403$, $\beta_1 = 0.0828$, $\sigma_{k1} = 1.0$, $\sigma_{\omega 1} = 0.856$

The blending function F_1 is defined by:

$$F_1 = tanh\left\{min\left[max\left(\left(\frac{\sqrt{k}}{\beta^*\omega d},\frac{500\,\mathbf{v}}{\omega d^2}\right),\frac{4\rho\sigma_{\omega 2}k}{CD_{kw}d^2}\right)\right]\right\} \tag{3.18}$$

With:

$$CD_{kw} = max\left(2\rho\sigma_{\omega 2}\frac{1}{\omega}\frac{\partial k}{\partial x_j}\frac{\partial \omega}{\partial x_j}, 1.0\ e^{-20}\right) \tag{3.19}$$

d: is the distance to the nearest surface.

For the k-ω model, the boundary condition on the solid wall is as follow:

$$\omega_{wall} = \frac{16\,\mathbf{v}}{\beta_1 d^2} \tag{3.21}$$

$$k_{wall} = 0 \tag{3.20}$$

Chapter 4

Numerical Simulation

The used turbulence model in the present study is k-ω SST model for the advantages that are mentioned in the previous chapter (Chapter 3). ANSYS Fluent 17.2 is the used software for the model solution. The software is used for modeling fluid flow, heat transfer and chemical reactions. The governing equations of mass, momentum and turbulence model are solved by Fluent which is based on control–volume technique [47]. The used main steps to solve the case are as follows:

- Geometry construction for walls and fluid domains which are considered the control-volume of the study.
- The control-volume is divided into discrete control volumes using a suitable computational grid.
- The governing equations of individual control volumes are integrated in order to form algebraic equations for dependent variables.
- The equations are linearized and solved to get updated values of the dependent variables.

The pressure-based segregated solver is selected for the fluid flow solution. Each iteration consists of steps as follows:

- Initialization of fluid properties based on the current solution.
- The current values of pressure and face mass fluxes are used to solve the momentum equation to update the velocity field.
- The continuity equation may not be verified by the velocity values that are obtained in the previous step. Pressure correction equation is derived from the continuity equation and solved to obtain the pressure and the face mass fluxes corrections.
- The previously updated variables are used to solve equations for scalar quantities.
- Convergence check of the equations is performed.

4.1 Three-Dimensional Wind Turbine model

4.1.1 Wind Turbine Rotor

The present study uses 3-bladed rotor designed according to Blade Element Momentum Theory (BEMT) that is explained in Chapter 1. The design was performed by Lee et al. [50]. The same design is considered in the present study in order to use their experimental values of power coefficient for our model validation. The rotor and hub diameters are 1 m and 0.16 m respectively.

Figure 4.1 shows the used rotor in the study which modelled by SolidWorks CAD software. The rotor blade length is 0.4 m with constant airfoil SD8000. Different chord lengths with different pitch angles are imported and converted to 3D model by loft feature as given in Table 4.1.

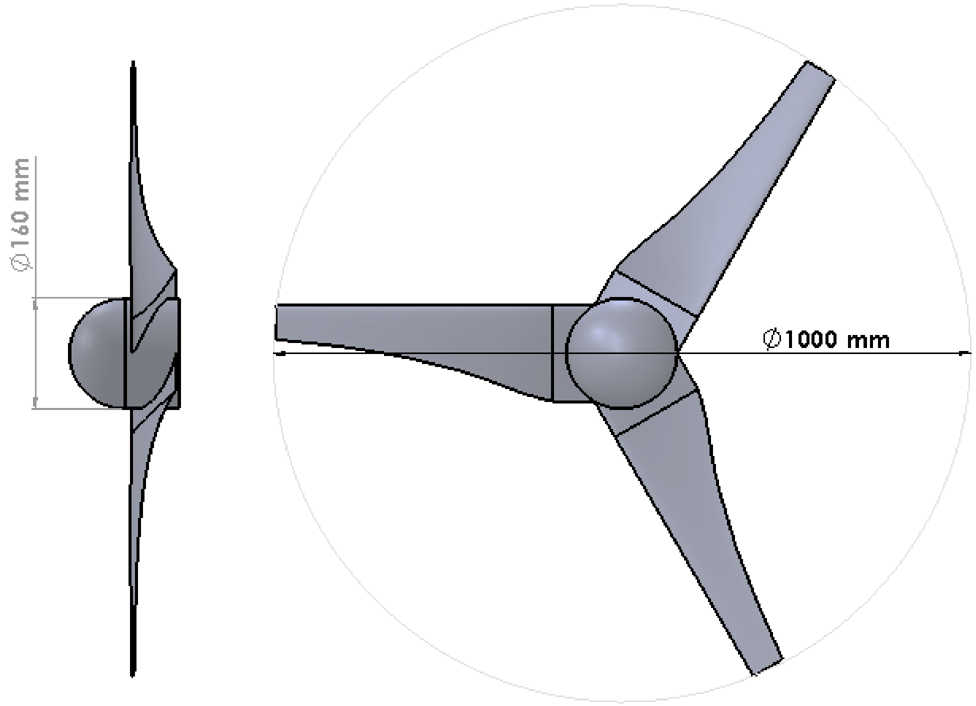

Figure 4.1: Wind turbine rotor used in CFD simulations

Table 4.1: Blade design parameters according to BEMT [50].

Blade Geometry			
Section	**r/R**	**Chord length (m)**	**Pitch angle (deg.)**
1	**0.2**	**0.153**	**25**
2	**0.29**	**0.133**	**18.1**
3	**0.38**	**0.113**	**13.6**
4	**0.47**	**0.096**	**10.5**
5	**0.56**	**0.084**	**8.2**
6	**0.64**	**0.074**	**6.5**
7	**0.73**	**0.066**	**5.2**
8	**0.82**	**0.059**	**4.1**
9	**0.91**	**0.054**	**3.3**
10	**1**	**0.049**	**2.5**

Figure 4.2 demonstrates that the blade is divided into 10 equal sections according to Table 4.1. The used airfoil SD8000 (Figure 4.3) is kept the same airfoil with different chord lengths. The air foil was used by Lee et al. [50] , since it is classified as a low Reynolds number (Re) airfoil [51].

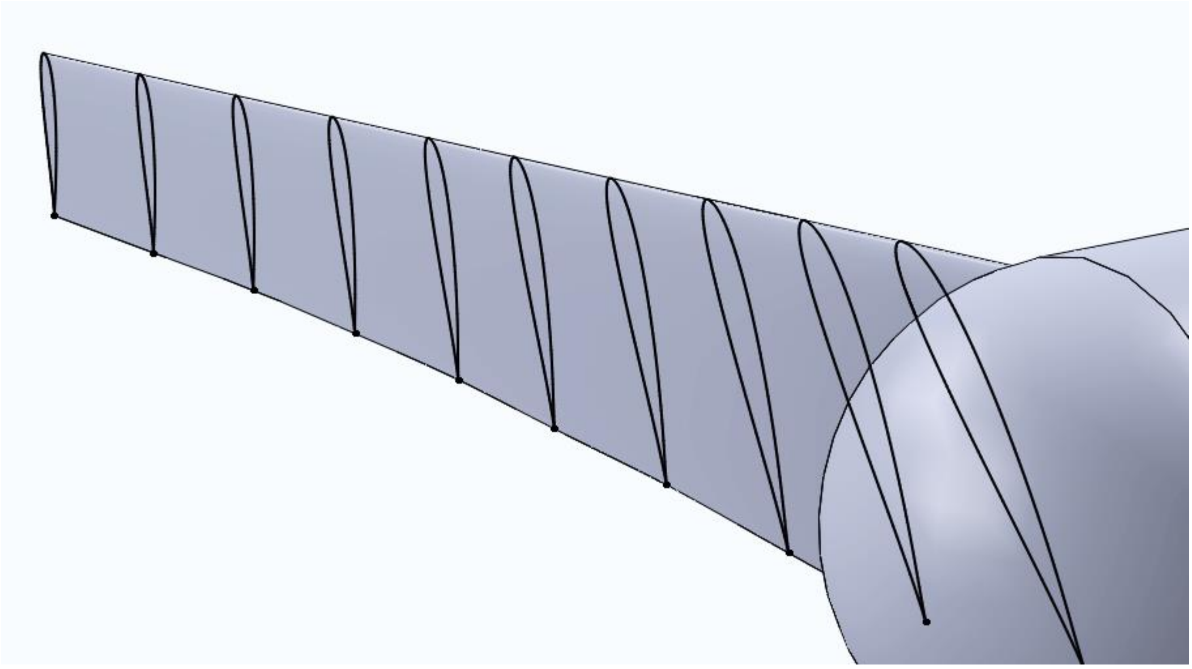

Figure 4.2: Different sections of the used blade with SD8000

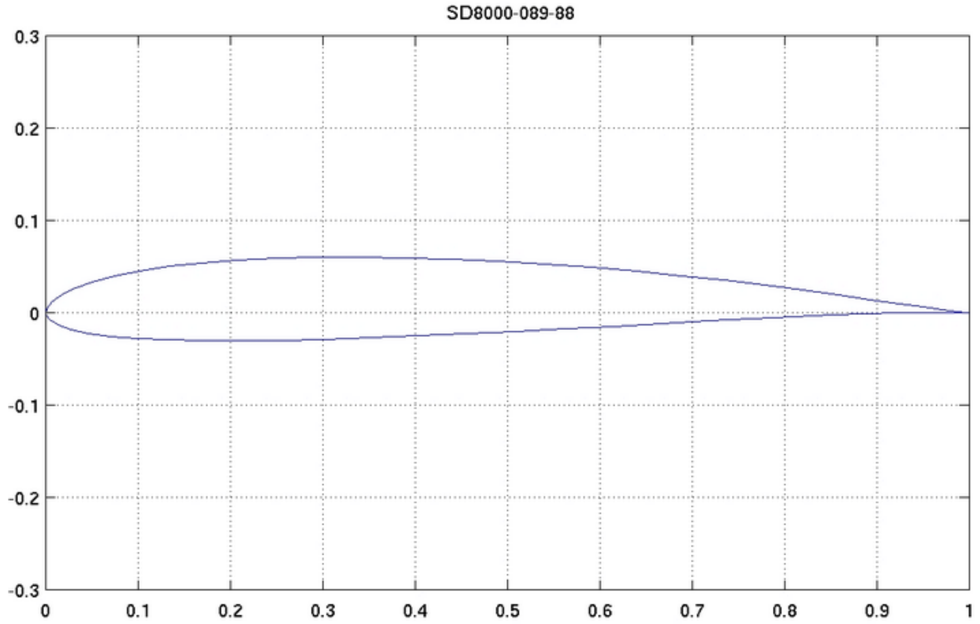

Figure 4.3: Airfoil SD8000 geometry and coordinates [51]

Low Re airfoils are thinner than the traditional airfoils which operates at high Re. The thin airfoils are selected to decrease the suction peak near the leading edge of the airfoil [[52] [53] [54]]. Therefore, the adverse pressure gradient (APG) decreases on the upper surface [[55] [56]]. The laminar flow doesn't separate from the surface as a result for APG decrease.

4.1.2 Winglet Design

Winglet is small device added to blade tip constructed from the same airfoil used in the blade or other airfoil. Its main function is to reduce the induced drag due to tip vortex. The added winglet produces another drag due to increased surface area and winglet shape. The optimum winglet should minimize the resultant drag; [11].

The main parameters used to design WL are height (span of winglet), sweep angle, cant angle, twist angle and toe angle as shown in Figure 1.12. Sweep and twist angles are selected to be zero in the present study.

The present research is performed to investigate the effect of WL's height (H) and toe angle (α_w) at upwind and downwind configurations. Present results are validated by comparison with experimental values for power coefficient and numerical flow parameter results by Lee et al. [50].

Ten winglets with the same thickness of wind turbine tip are considered in the numerical study (Table 4.2). CFD simulations are performed to investigate the effect of four upwind winglets with different heights namely 8% R, 4% R, 2% R and 0.8% R. Toe angle parameter was studied by keeping the winglets heights are constant at 0.8% R. Three upwind winglets with different toe angles namely +10°, +20° and +30° are considered in the study in addition to other three downwind winglets with toe angles namely -10°, -20° and -30°. For all winglets, the curvature radius is equal to 0.8%R which is considered the minimum height of the winglets. Twist and cant angles are kept constant for all designs to be 0° and 90° respectively.

Table 4.2: Cases data for CFD simulations

Case No.	Winglet name	Winglet Height (H) (% Radius)	Toe Angle (α_w) (deg.)	Direction
1	Rotor	-	-	-
2	WL 1	8	0	Upwind
3	WL 2	4	0	Upwind
4	WL 3	2	0	Upwind
5	WL 4	0.8	0	Upwind
6	WL 5	0.8	+10	Upwind
7	WL 6	0.8	+20	Upwind
8	WL 7	0.8	+30	Upwind
9	WL 8	0.8	-10	Downwind
10	WL 9	0.8	-20	Downwind
11	WL 10	0.8	-30	Downwind

4.2 Computational domain and boundary conditions

4.2.1 Computational Domain

Three-dimensional computational fluid dynamics (CFD) analysis was performed on the 3-bladed rotor model of diameter 1 m and blade length 0.4 m. The full 3-bladed model is considered in the simulations for all cases with and without winglets. The torque that generated due to flow around the rotor blades is the goal for the CFD simulations. It is used to determine the power extracted from the rotor (Eq. (4.1)). The tip vortices and flow characteristics are considered too in the CFD model.

$$P = T.\omega \tag{4.1}$$

Where: P: the generated power in Watts

T: the generated torque from the rotor in N.m

ω: the angular velocity of the rotor in rad/s

Full fluid domains are modelled in the study around the wind turbine rotor as shown in Figure 4.4. The main computational fluid domain is with diameter 2.8 D and expands up to 5.25 D downstream the rotor. A long rotating fluid domain with diameter 1.6 D expands up to 3.2 D downstream the rotor. The rotating domain is considered long enough in order to show the helical paths of tip vortices and flow characteristics in the wake of the rotor. The boundary conditions are set around the main fluid domain. The rotating domain is an interior fluid domain around the rotor surface. It rotates as a moving reference frame about the rotor axis of rotation in a direction opposite to the rotation direction of the rotor. By keeping the rotor blades at rest. The rotating fluid rotation in addition to the inlet flow boundary condition give the same effect of the rotor rotation by wind flow action. The moving reference frame (MRF) is easier than

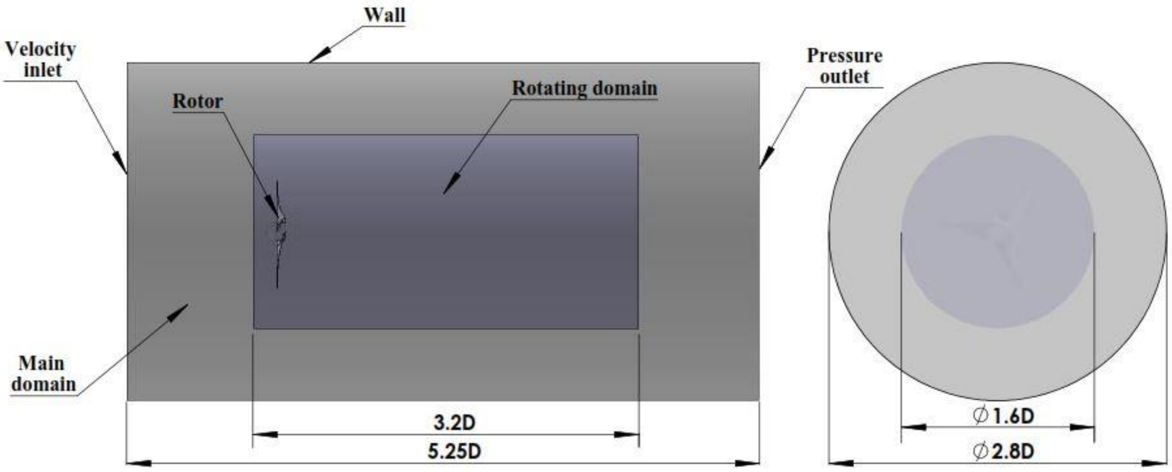

Figure 4.4: Rotor and complete domain with boundary conditions geometry

moving mesh which requires complex dynamic meshing thereby needs more computational power.

4.2.1.1 Boundary conditions (BC)

After the creation of fluid domains around the rotor surfaces, the flow boundary conditions are required to be specified for the main fluid domain. Three boundary conditions are used in the study namely velocity inlet, pressure outlet and walls.

4.2.1.1.1 Velocity inlet

It is a boundary condition used to define the inlet flow velocity and turbulence intensity across the inlet section of the fluid domain. It is intended for incompressible flow and has to be applied as far away from the rotor surface as possible. Fluent can define the mass flow rate by defining the inlet velocity. The velocity inlet value is set to be 8 m/s at the present study.

4.2.1.1.2 Pressure outlet

It is an outflow boundary conditions based on the flow gauge pressure at outlet. The flow velocity and characteristics are calculated based on the fluxes. The pressure outlet is set to be zero gauge pressure for the present study.

4.2.1.1.3 Wall (no-slip)

It is used to bound fluid domains and to be the boundary condition for the rotor surfaces.

4.3 Mesh generation

The used grid and number of elements determine the accuracy of solution. There are different types of mesh methods according to elements shapes like tetrahedral, hexahedral and polyhedral mesh.

Polyhedral mesh is employed along the computational domain. It is selected due to its lower run time and faster convergence. It handles large computational domains and produces maximum orthogonal skeweness much lower than that produced by tetrahedral mesh. Polyhedral elements have got less attention in the past because of the unavailability of mesh generation algorithms in CFD codes as mentioned by Iqbal and Chan [57]. Recently, polyhedral mesh has been widely used. Peri [58] and Garimella et al. [59] concluded that polyhedral elements can overcome divergence associated with tetrahedral elements using fewer elements. Three mesh elements sizes are used in the study for the two fluid domains and the rotor surface.

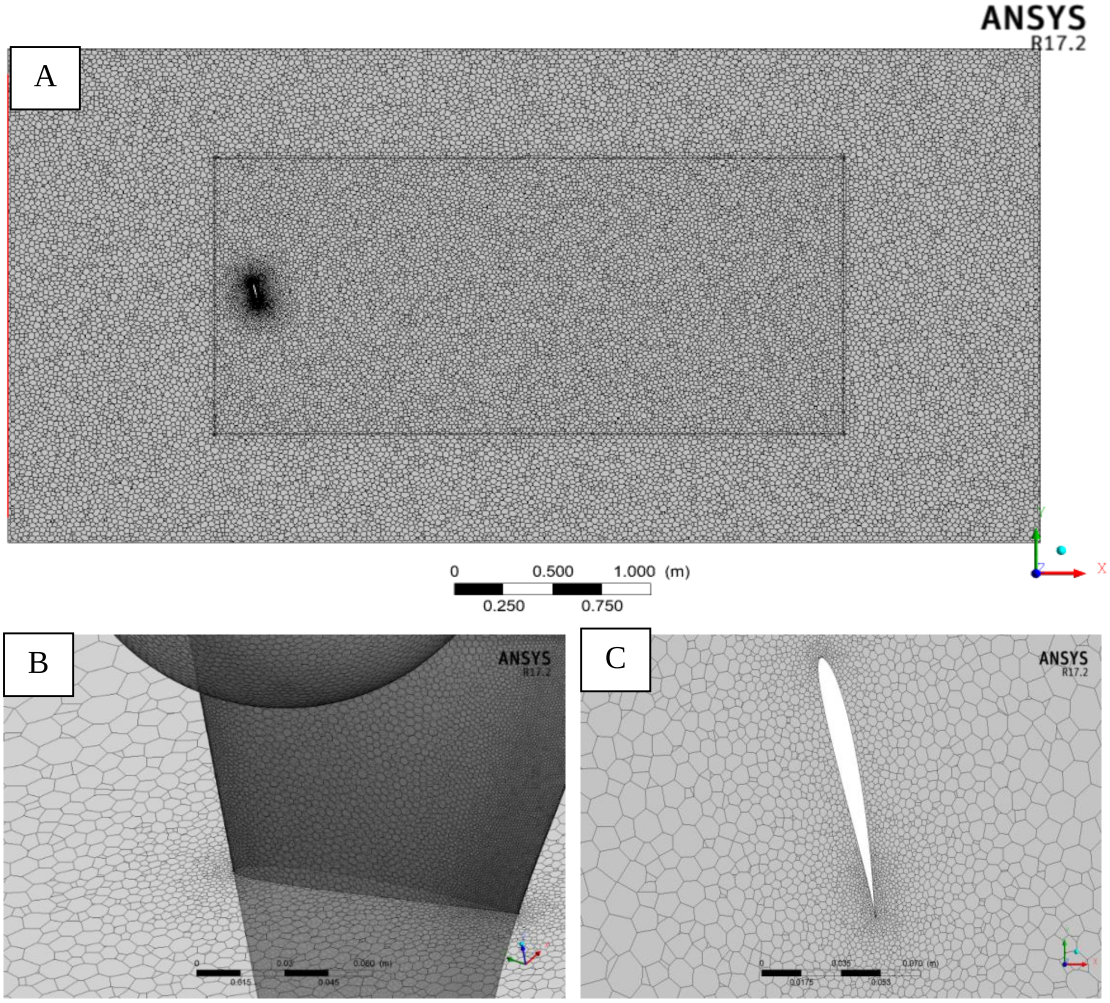

Figure 4.5: Polyhedral mesh generation

A: Complete domain, B: Hub-blade root region, C: Blade airfoil

Polyhedral mesh improves mesh quality at complicated geometries such as the presented rotor at the study. For the present rotor mesh, the maximum orthogonal skeweness is 0.45 while tetrahedral mesh produced 0.85 maximum orthogonal skeweness. Figure 4.5 demonstrates polyhedral elements shape, propagation and elements flexibility to form the wall around the airfoil.

4.3.1 Mesh sensitivity

Since the accuracy of the numerical results depends on the number of elements used, the present results are checked for elements number independency. It is carried out for one of the cases of the present study. Figure 4.6 shows the effect of the number of mesh elements on the rotor torque which is the most effective parameter for power estimates. The figure shows that the results are almost independent of mesh elements number for all values of number of elements equal or above 3.8 millions. Accordingly this number is used for all results reported in the thesis.

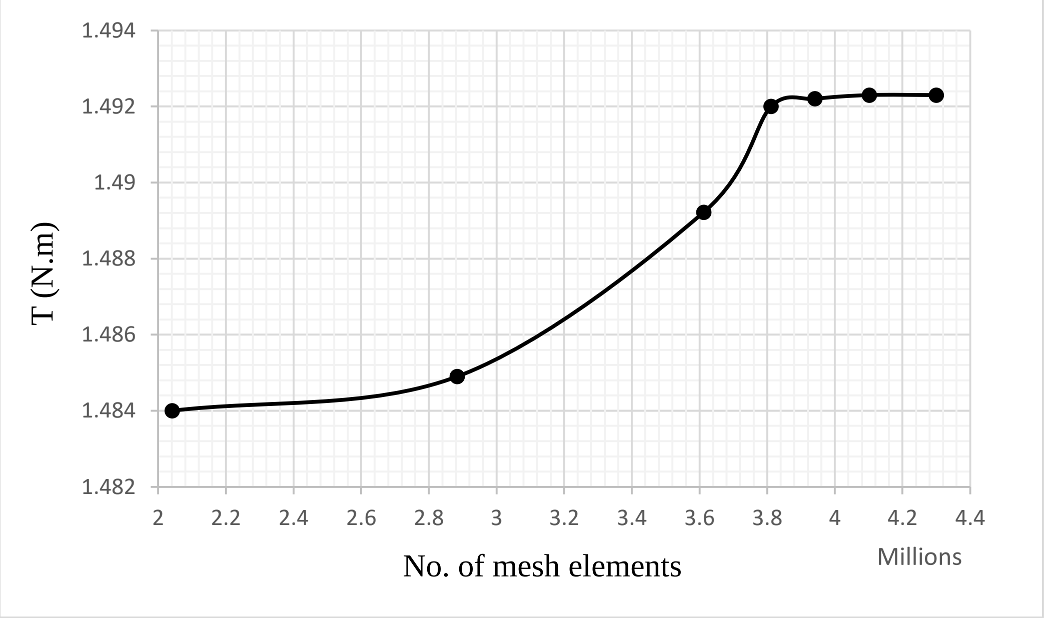

Figure 4.6: Number of mesh elements effect on the torque value of the rotor without WL at λ=4

Chapter 5

Experimental Procedures

5.1 Introduction

Experimental work is very important for CFD results verification especially for the modifications which were performed on blade tip. Experiments prove the ability of adding winglet to the blade tip and its effect in wind power augmentation. Wind turbine blade manufacturing is the most difficult process in the turbine production. It needs high accuracy in manufacturing in order to apply the typical proposed design. Blade material is very crucial parameter in blade manufacturing especially for large scale wind turbine. Blade manufacturing technique depends on wind turbine size. Small wind turbine blade construction requires an accurate technique to show the small design details. Three-dimensional (3D) printer is the most accurate technique that is used in manufacturing small models. It requires a three-dimensional geometry for the model which is required to be constructed. For the present study, the 3D geometry is performed by Solidworks software.

Figure 5.1 shows a schematic drawing for the experiment main components. The rotor is assembled from 3 blades and fixed on rotating disc which is fitted to the shaft of the DC generator. The rotor tower is placed at distance 2 m from the wind tunnel outlet section.

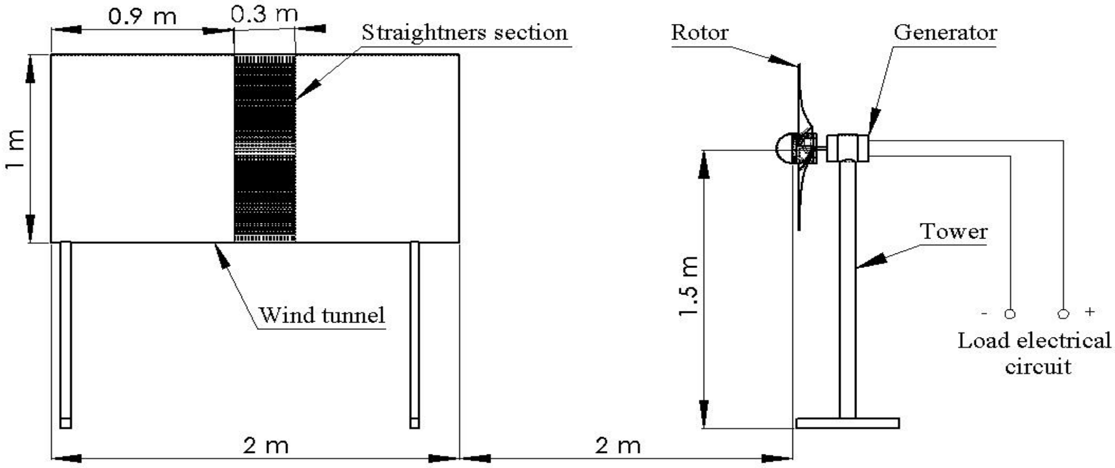

Figure 5.1: Schematic drawing for the experiment

5.2 Wind turbine rotor

Figure 5.2 shows exploded view for the rotor assembly. The rotor is assembled of three blades which are fastened to hub plate by three through bolts. The three blades are bounded by hub nose and fastened by three through bolts as shown in Figure 5.2 and Figure 5.3. The blade base is considered as a part of the hub in order to strength the blade root. The rotor is fitted to the DC generator shaft as shown by Figure 5.4.

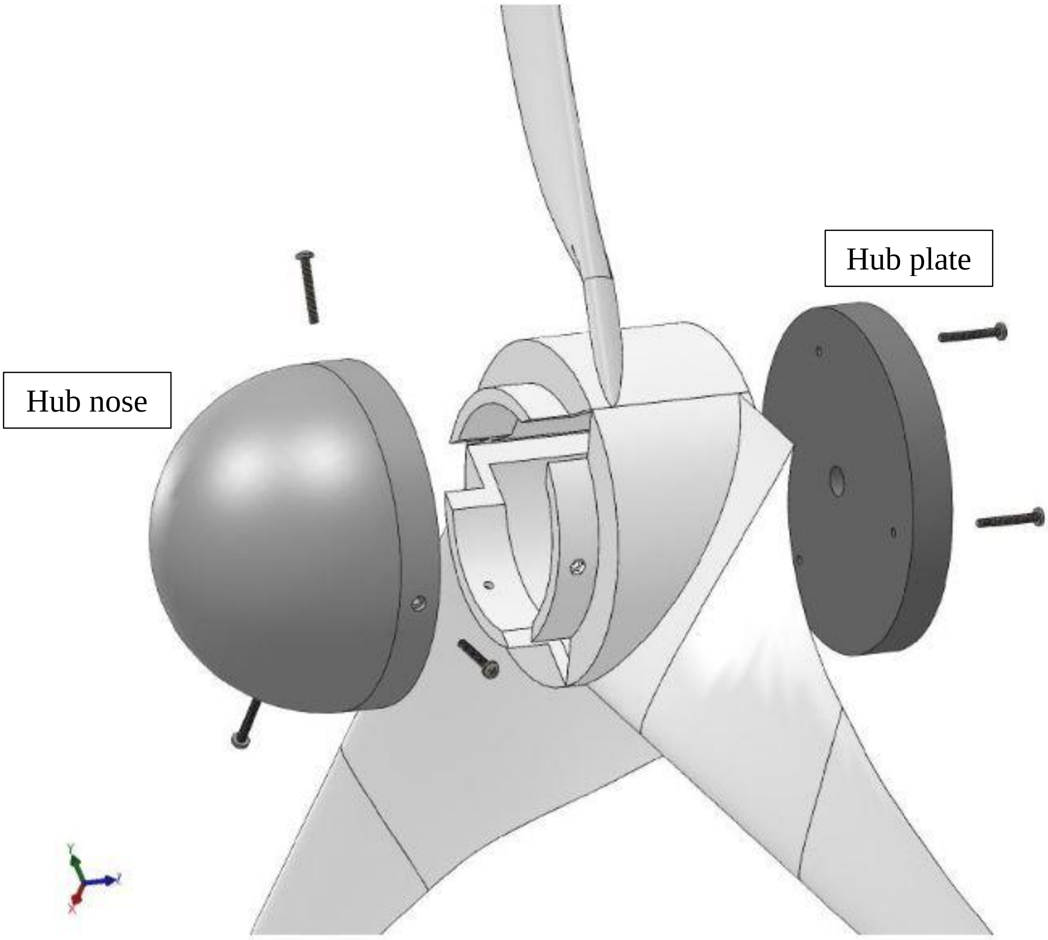

Figure 5.2: Exploded view for the wind turbine rotor

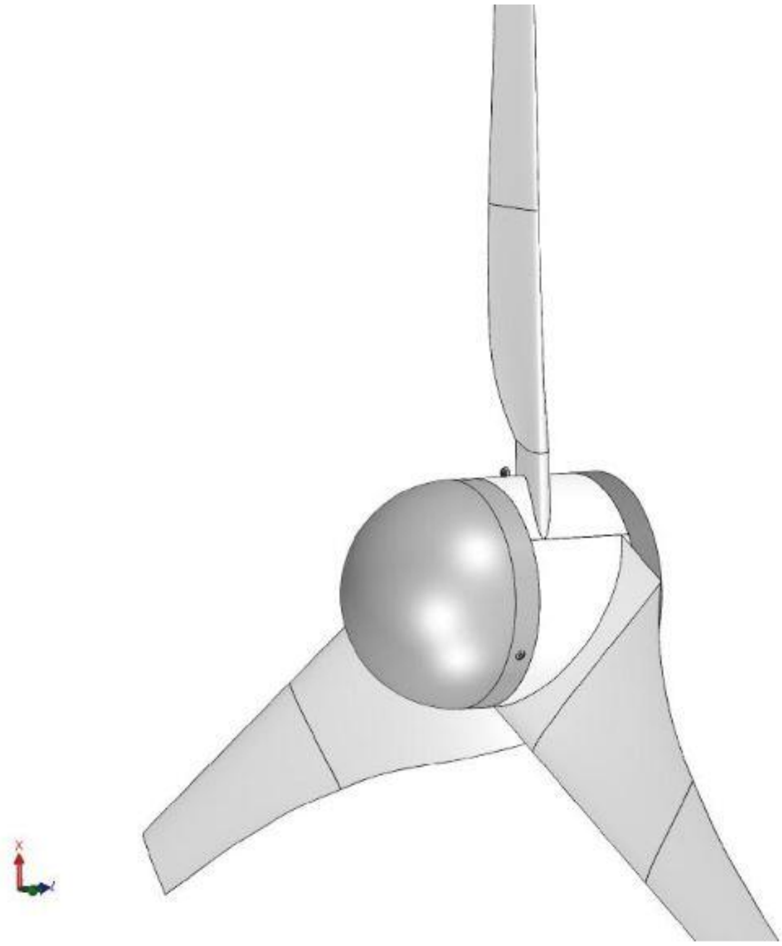

Figure 5.3: Complete wind turbine rotor

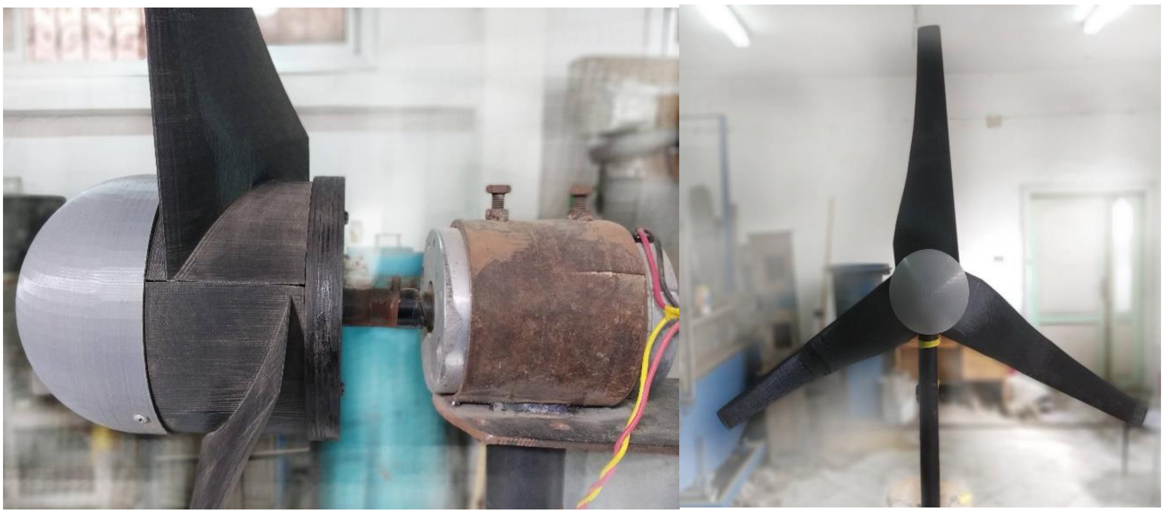

Figure 5.4: Actual assembled rotor to generator

5.3 Wind turbine blade material

Wind turbine blade should be made from durable and light material. The blade should withstand fatigue and dynamic loads which is occurred due to wind fluctuations. Wind dynamic loads should be considered especially in large scale wind turbine. Fiber glass is the most common material that is used in wind turbine blade production due to its good mechanical properties.

For small-scale wind turbine blades, several materials can be used like wood, PVC, carbon glass, epoxy glass and aluminum. There are different materials can be used by 3D printing technology only like ABS, PLA and nylon. Each material has a certain mechanical and thermal properties. 3D printing is the most accurate technology for manufacturing small models with the same drawing accuracy.

5.4 Manufactured wind turbine model

The wind turbine model which is designed by Lee et al. [50] is performed with the same scale of the modeled rotor in CFD simulations (Chapter 4). For manufacturing simplicity, the model is assembled from six parts namely hub plate, nose, three blades and DC generator.

5.4.1 Blade

The blade is assembled from two parts namely blade base and blade tip. The blade base includes a part of the model hub. It is manufactured at two parts due to the 3D printer dimensions limitation. The whole blade length includes the base is 460 mm while the maximum dimension can be modeled by the 3D printer is 400 mm. The two parts of the blade are supported by three steel studs in order to strength the connection between the two parts as shown in Figure 5.5. The bond between the two parts is performed by using epoxy glue (resin + hardener). The blade tip is supported by two holes in order to fix the WLs studs as shown by Figure 5.6.

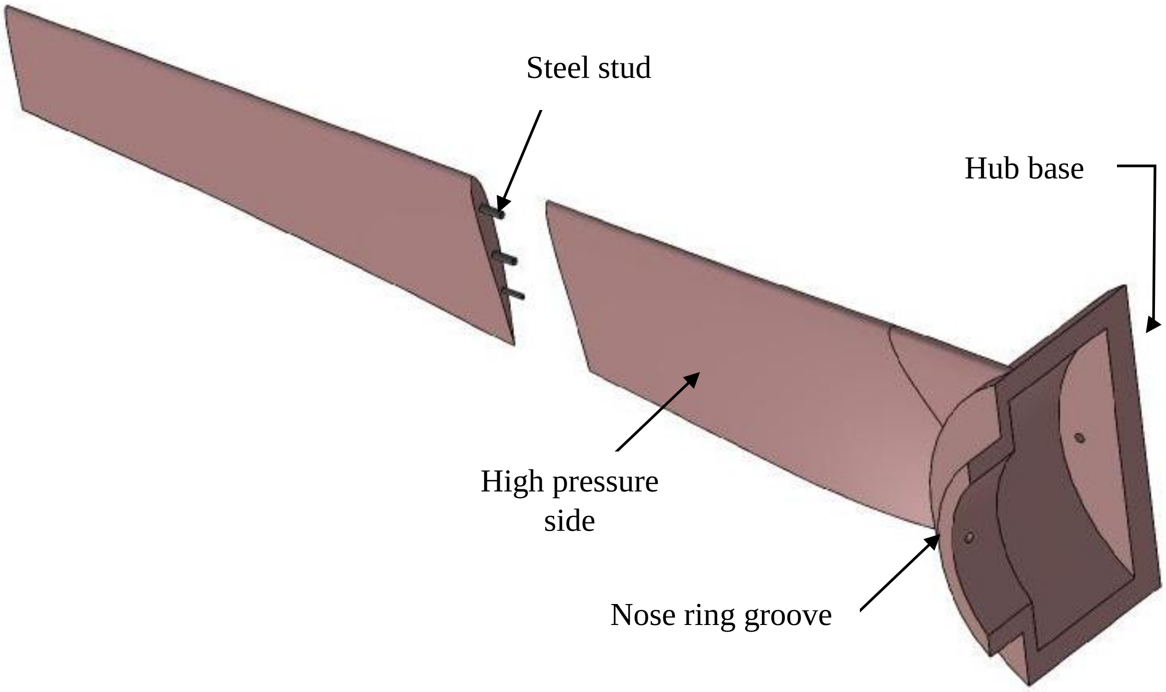

Figure 5.5: Blade assembly of the model

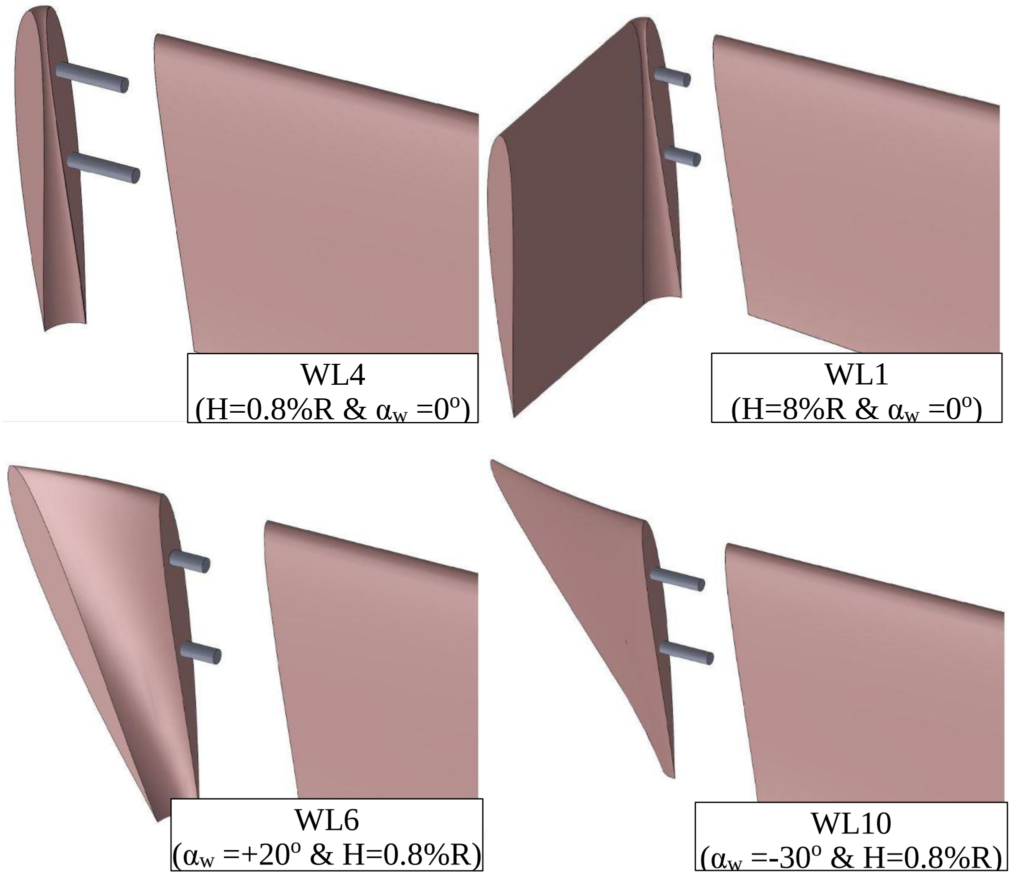

WL4 ($H=0.8\%R$ & $\alpha_w=0^o$)

WL1 ($H=8\%R$ & $\alpha_w=0^o$)

WL6 ($\alpha_w=+20^o$ & $H=0.8\%R$)

WL10 ($\alpha_w=-30^o$ & $H=0.8\%R$)

Figure 5.6: WLs fixation method to the rotor tip

5.4.2 Nose

The nose enhances the wind turbine aerodynamic performance and prevent stagnation at the turbine head. Therefore it has a semispherical shape with diameter 160 mm and is made from PLA material using 3D printing technique. The designed nose of the wind turbine model has other function beside its aerodynamically enhancement. It includes a ring which is responsible for the circumferential assembly for the three blades as shown in Figure 5.7.

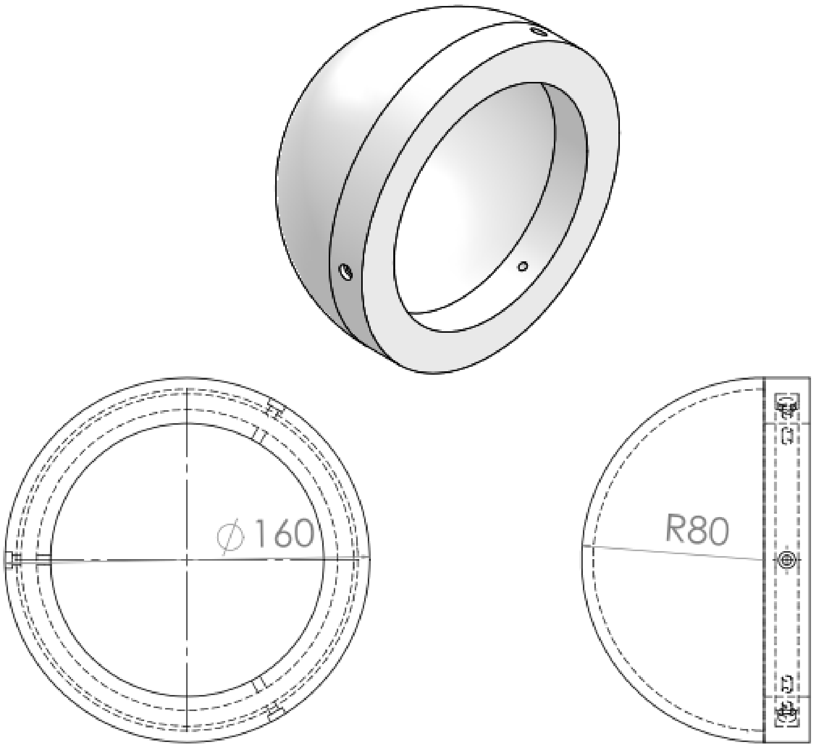

Figure 5.7: Schematic drawing for the model nose

5.4.3 Hub plate

It is a wooden circular plate with thickness 20 mm and diameter 160 mm (Hub diameter). It is adjusted to be suitable for the fixations of the three blades bases. Its axis is fixed on the generator shaft by suitable coupling. The hub plate is adjusted with a groove suitable for hexagonal nut M14 which is considered the lock for the plate towards the thread coupling as shown in Figure 5.8. The coupling is a thread with M14 from one side and the opposite side is a sleeve in order to fit with the generator shaft.

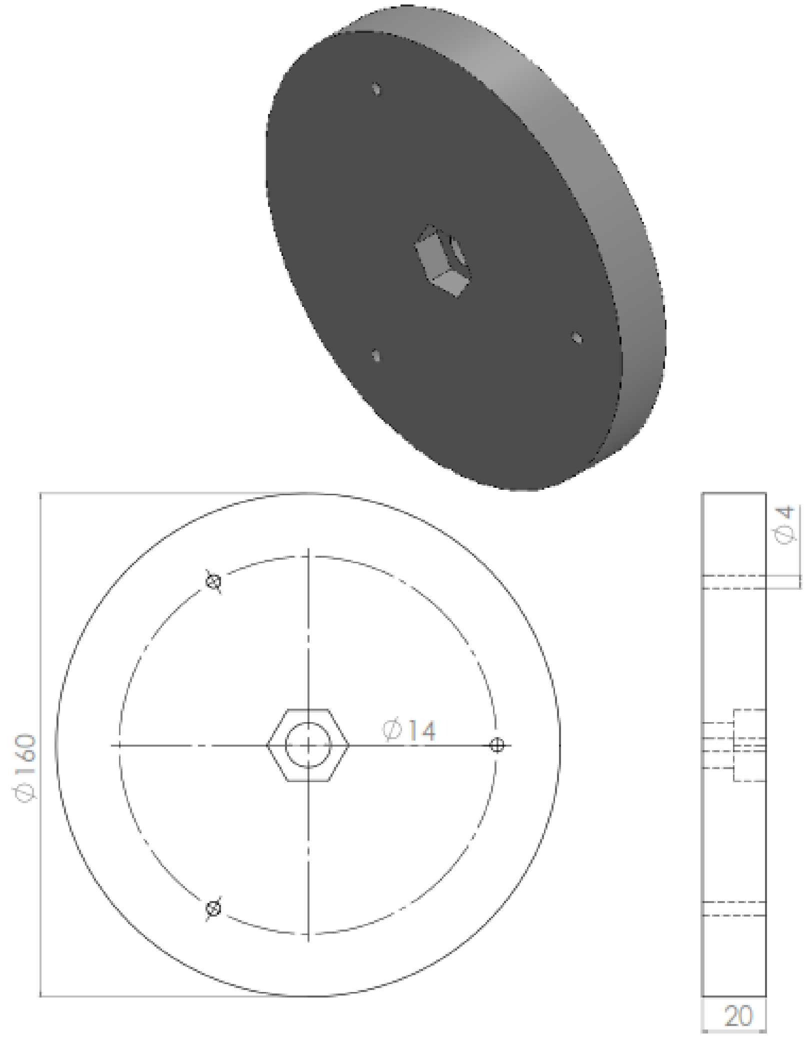

Figure 5.8: Schematic drawing for the hub plate

5.4.4 Permanent magnet DC generator

Direct current is better in measurements and control. Therefore the use of permanent magnet DC generator is a good choice for power generation in the study. The generator is connected directly to the rotor shaft. It is selected due to its lower rated speed 1200 rpm which is suitable for the used speed range. Since for the present study, the maximum rotor speed should be 1200 rpm in order to achieve the maximum tip speed ratio ($\lambda = 7$) at wind speed 8 m/s. The used generator is AMETEK 07980 with nominal voltage of 40 V. For power generation application, it needs torque of 0.31 N.m to produce current of 1A at maximum load condition based on the manufacturer data [60]. For the present study the maximum torque is achieved at 3.19 A and 746 r.p.m, therefore the mechanical torque transported to the generator is estimated to be =0.9889 N.m and thus the mechanical power is 77 watts. The actual electrical power generated at the mentioned point is 34.65 watts. Therefore the mechanical transmission efficiency is around 45%.

Figure 5.9: Permanent magnet DC generator

5.5 Experimental setup

5.5.1 Free-jet wind tunnel

The experiments were carried out by the free-jet wind tunnel facility (Figure 5.10) at hydraulics laboratory, Shoubra faculty of engineering, Benha University, Egypt. It includes an axial fan with 1 m diameter which is assembled to circular duct with the same diameter and of length equal 2m. The used axial fan model is Wolter BXV 1000 with adjustable pitch of the blades and directly driven by AC 5.5 kW, 3-phase motor. The center of the tunnel section is above the ground by 1.5 m which is the same height of the wind turbine model tower. The axial fan generates axial flow rate with swirling motion. Therefore the use of air straightener section became very necessary. It was installed at the middle section of the tunnel and made of UPVC tubes of diameter 32 mm. The tubes were attached together to form circular disc of tubes with the same diameter of the tunnel. The wind tunnel fan motor is controlled by digital frequency inverter as shown by Figure 5.11. It is used to control the fan speed and thus control the air velocity.

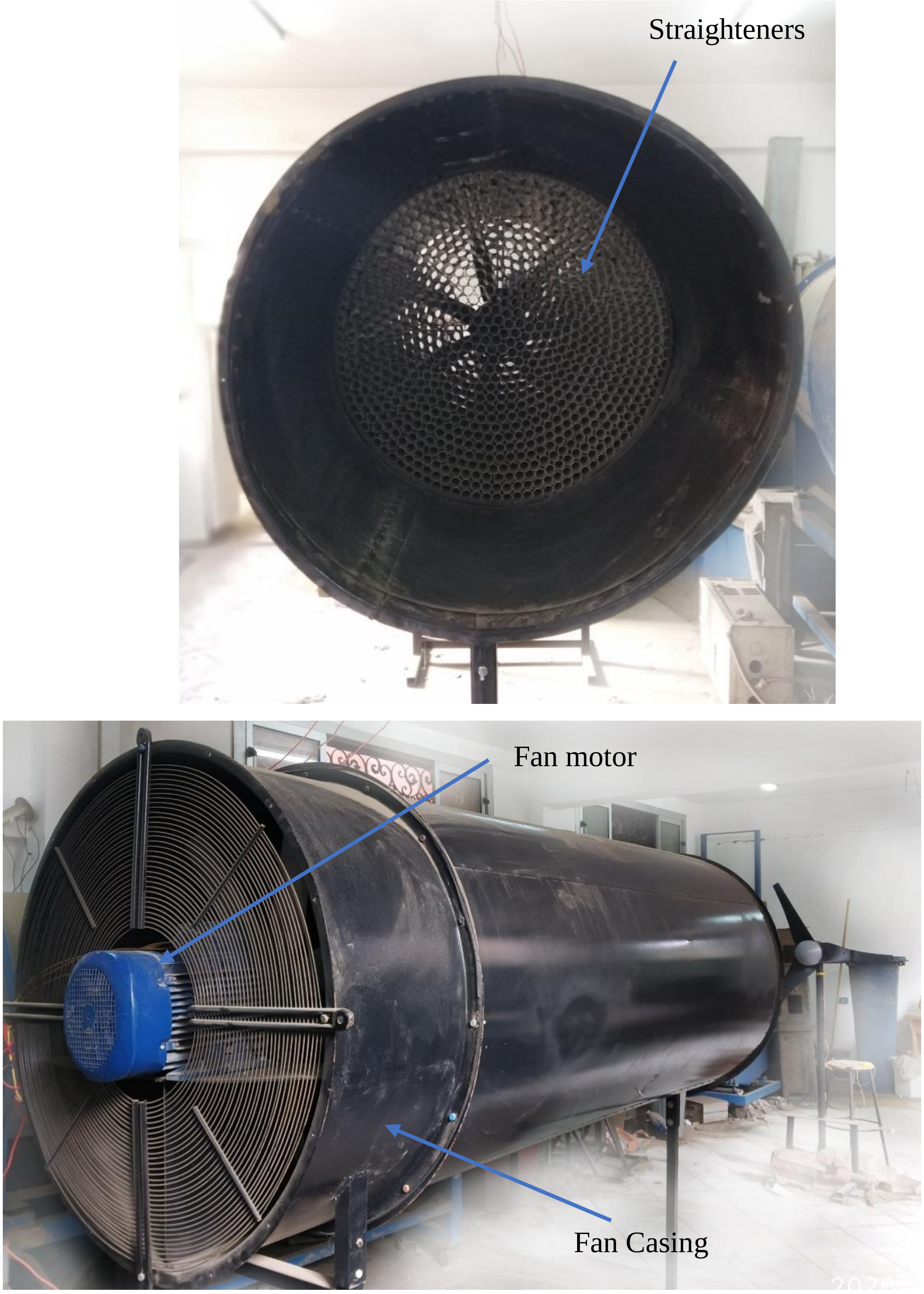

Figure 5.10: Free jet wind tunnel with the straighteners section

The digital frequency inverter is adjusted at 30 HZ to produce mean wind velocity U=8 m/s. The velocity distribution across the wind tunnel section is recorded at different radial positions as shown in Figure 5.12. The mean velocity is calculated from the measured velocities, it is about 8.3 m/s. The difference between the mean velocity and the minimum value is about 1.8 m/s.

Figure 5.11: Digital frequency inverter

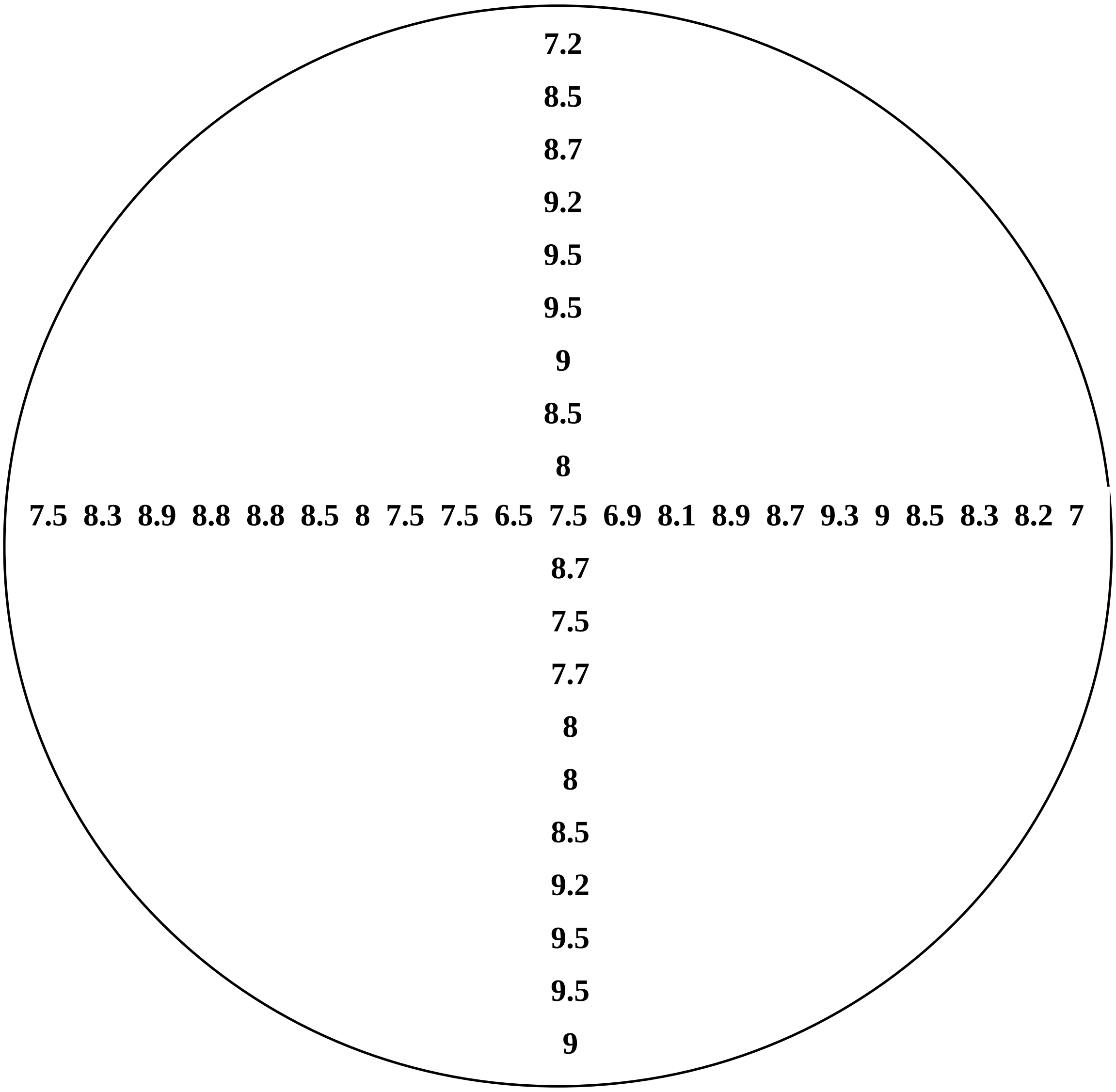

Figure 5.12: Wind tunnel velocities distributions at distance 2m in front of the tunnel

5.5.2 Measurements devices

Tachometer

The rotor rotational speed is measured by an optical digital tachometer device. The device works by the laser bean direction towards a reflector on the rotating part. It can perform its function by accounting the number of reflecting laser receiving times per one minute. Lutron optical tachometer (Figure 5.13) supports wide measuring range from 0.5 to 100000 r.p.m.

Figure 5.13: Lutron photo tachometer

Pitot tube manometer

The air velocity is measured by Pitot tube which is connected to a digital manometer as a transducer as shown by Figure 5.14. The calculated air velocity is an average value for the different values that were measured across the tunnel section.

Figure 5.14: Pitot tube and digital differential manometer

Voltameter

It is connected in parallel to the generator output in order to measure the generated voltage at different electrical loads.

Ameter

It is connected in series to the loads circuit in order to measure the current at different electrical loads.

5.5.3 Loads electrical circuit

It is a simple electrical circuit operated by the output power from the generator as shown in Figure 5.15. The used loads are presented in resistance elements with 0.22 Ω for each element (Figure 5.16). The resistance elements are considered variable load system. The load variation is very necessary for controlling the rotation speed of the rotor. Therefore the tip speed ratio variation is considered by rotor speed variation while the generated air speed is kept constant with 8m/s for all experiments. The Ameter is installed in series with the circuit load while the Voltameter is installed in parallel to the circuit. Other circuit with switch and constant resistance of 1 Ω is attached in parallel to the main circuit. It is considered an emergency circuit to avoid the extra rotational speeds of the rotor during changing the main load. Since, the circuit is open at the period during changing the load. The emergency circuit is normally opened in case of experiment with specific load while it is closed during changing the load.

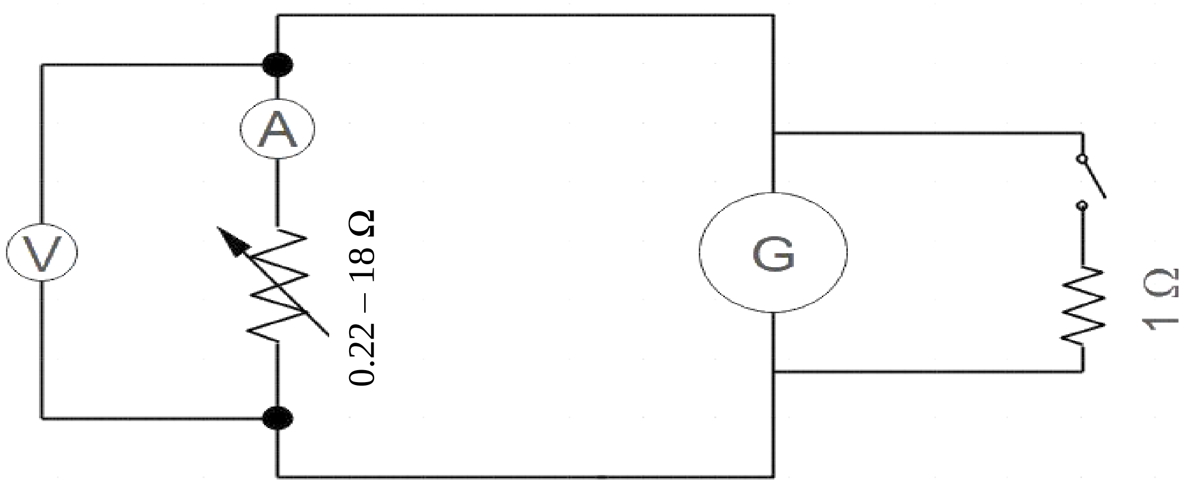

Figure 5.15: The used electrical circuit in the study

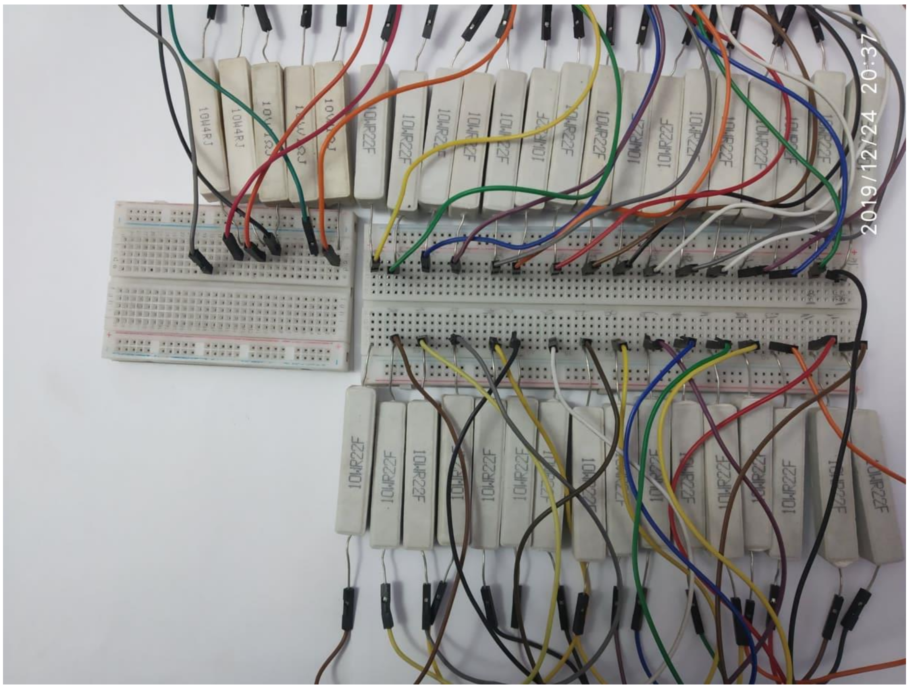

Figure 5.16: Electrical heat resistors connected to bread board

Chapter 6

Results and Discussion

6.1 Introduction

The present chapter represents the computational and experimental investigations that are performed in the study. At first, CFD validation is performed with the CFD and experimental results of Lee et al. [50]. Then, CFD results of all cases of the present study are explored. Finally, experimental results are performed for some of cases to verify the effect of using WL.

6.2 Numerical model validation

The present CFD together with turbulence model and complete geometrical model are validated by comparing the present results of C_{PW} with experimental values of Lee et al. [50]. Computations are carried out at wind velocity of 8 m/s and λ between 3 and 8. Figure 6.1 shows a good agreement of the present results with those of Lee et al. [50]. The maximum discrepancy amounts to about 7%. It can be explained by transmission efficiency and friction.

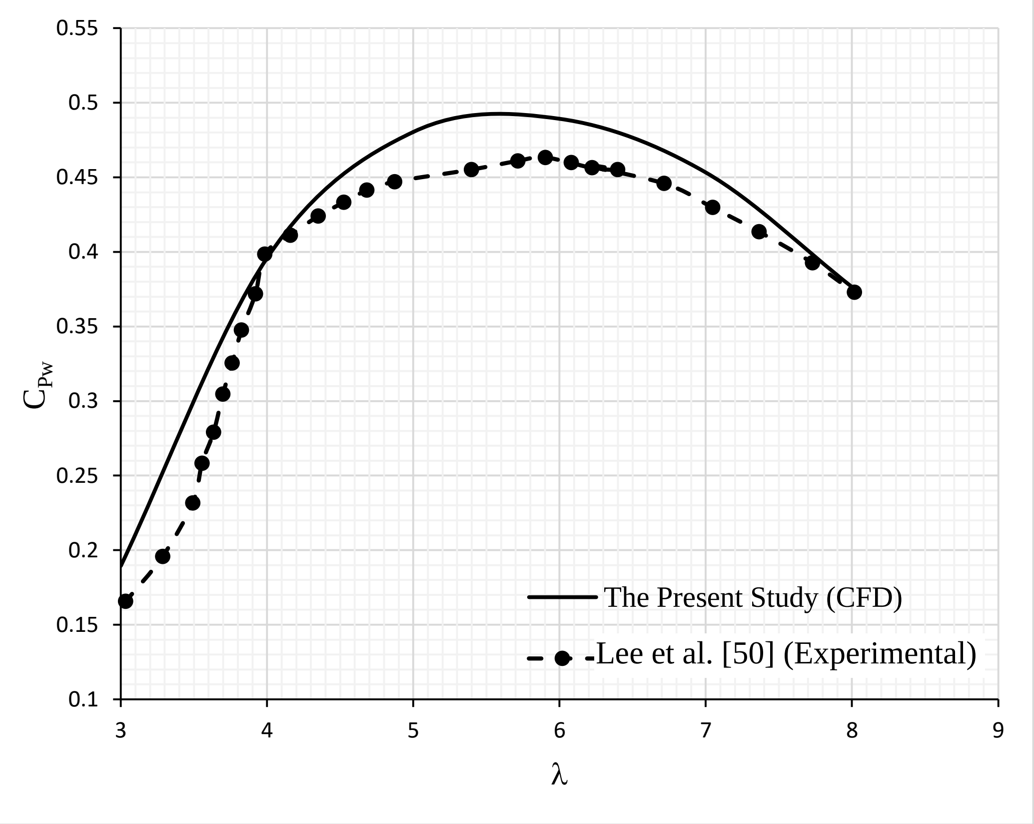

Figure 6.1: Comparison between the present results and experimental values by Lee et al. [50] for power coefficient.

For more validation details, results of pressure coefficient distribution (C_P) over different sections of the blade are obtained and compared with the numerical values by Lee et al. [50] at the same value of wind velocity (U=10m/s) and tip speed ratio (λ=5.236). Figure 6.2 shows that C_P distribution of the present study is generally in a good agreement with those of Lee et al. [50]. Results at section r/R= 0.38 show some discrepancies, as the maximum deviation in C_P is noticed to be about 5 %. This deviation appears near the root of the blade. It may be explained by the large pressure gradient near the hub and thus more nodal points are needed to capture the pressure variations. The comparisons show that the present model is accurate both for local values of pressure coefficient along the blades and integrated power output of the turbine.

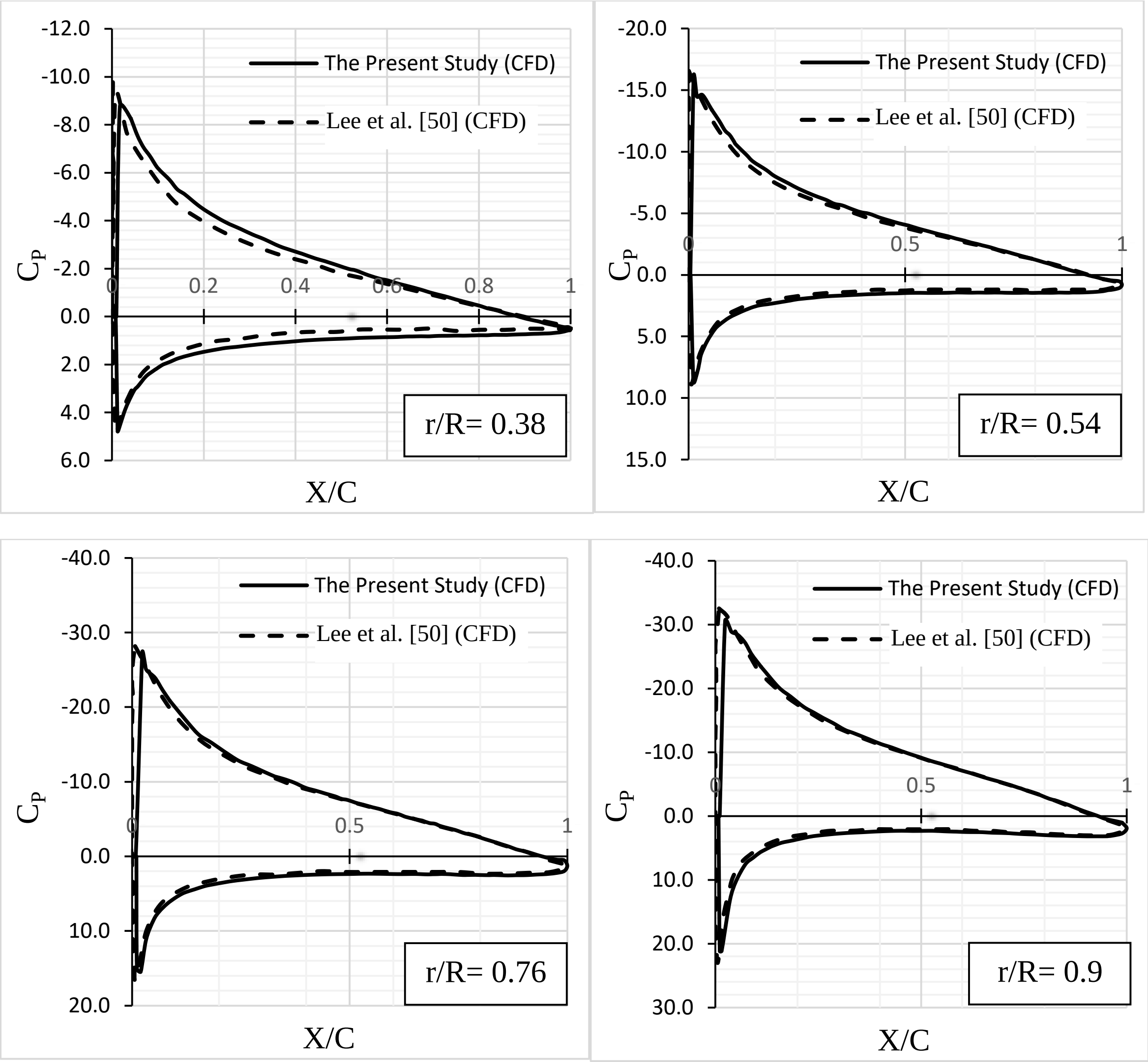

Figure 6.2: Comparisons of pressure coefficients with those by Lee et al. [50] at λ=5.236 and U=10 m/s

6.3 Numerical results

6.3.1 Tip vortex effect on the pressure coefficient

For understanding of tip vortex effect on the rotor performance, the pressure coefficient distributions over five sections near the blade end are studied as shown in Figure 6.3, Figure 6.4, Figure 6.5 and Figure 6.6. The figures show the dangerous effect of the tip vortex on the rotor performance. Starting from position r/R=0.94, the difference in C_p values on high and low pressure surfaces decreases and vanishes at the blade tip (r/R=1). The upper and lower values of the graph transferred to negative position due to tip vortex effect. Although the high positive pressure concentration at the leading edge for all sections of the blade span, section r/R=1 shows higher negative pressure concentration at the leading edge up to 0.1 of the chord length with respect to whole of the chord length especially for higher values of λ. Therefore, the next section about the tip vortex origin gives more explanation about the phenomenon.

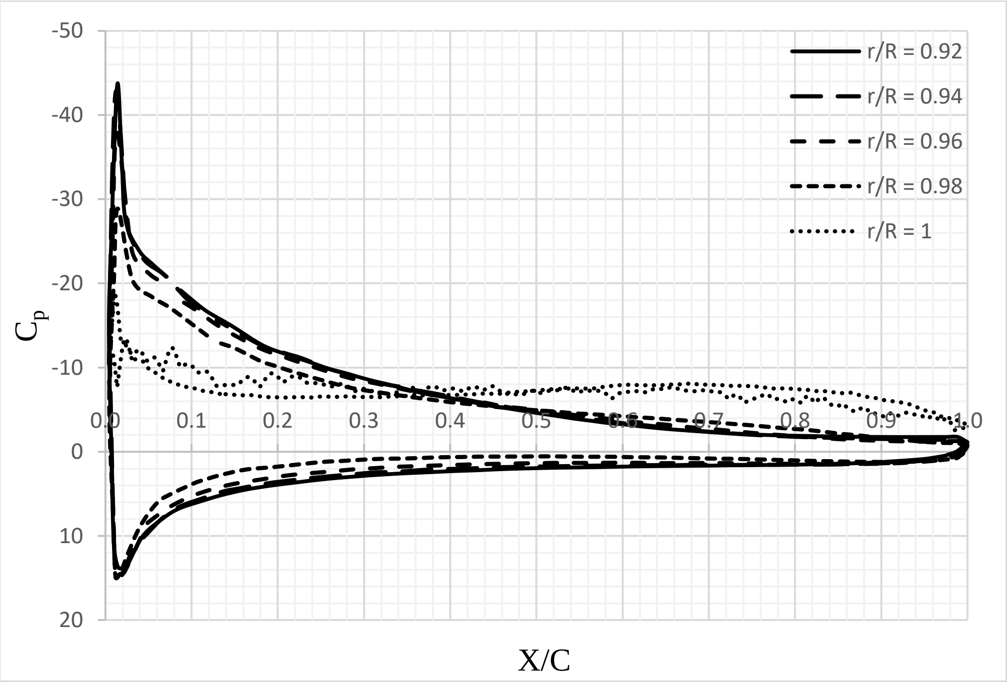

Figure 6.3: Pressure coefficient distribution over different sections at U=8m/s and λ=4 for blade without WL

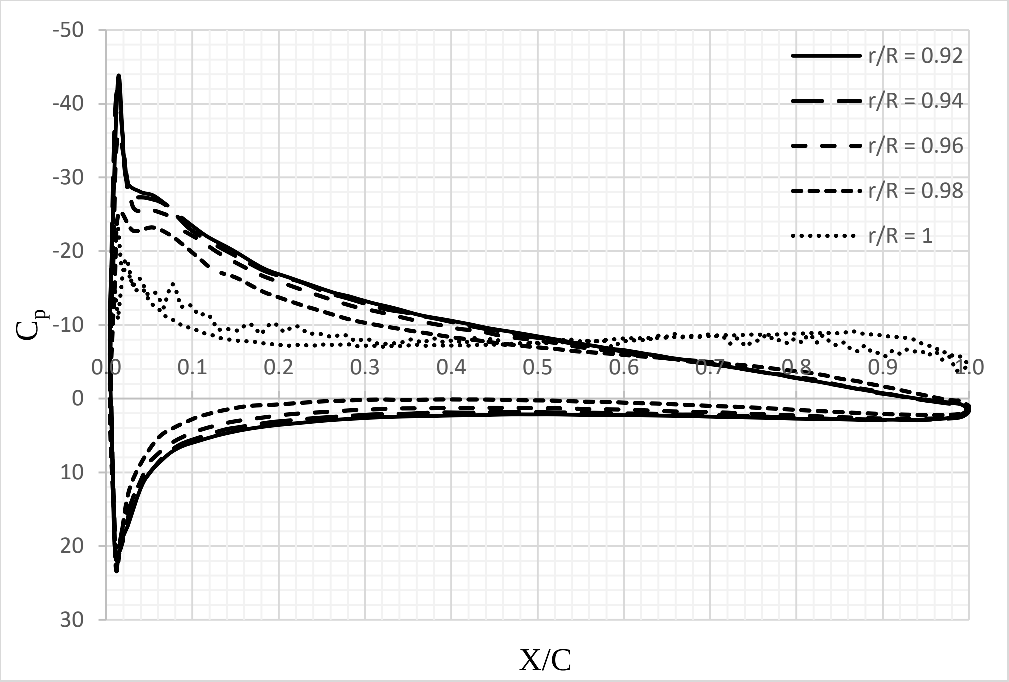

Figure 6.4: Pressure coefficient distribution over different sections at U=8m/s and λ=5 for blade without WL

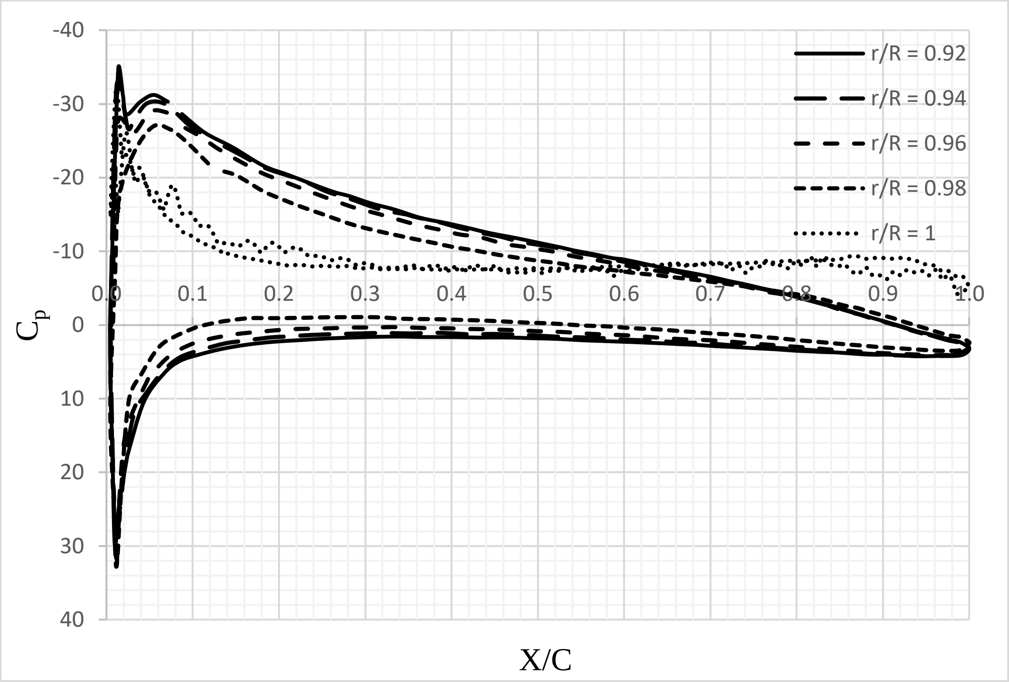

Figure 6.5: Pressure coefficient distribution over different sections at U=8m/s and λ=6 for blade without WL

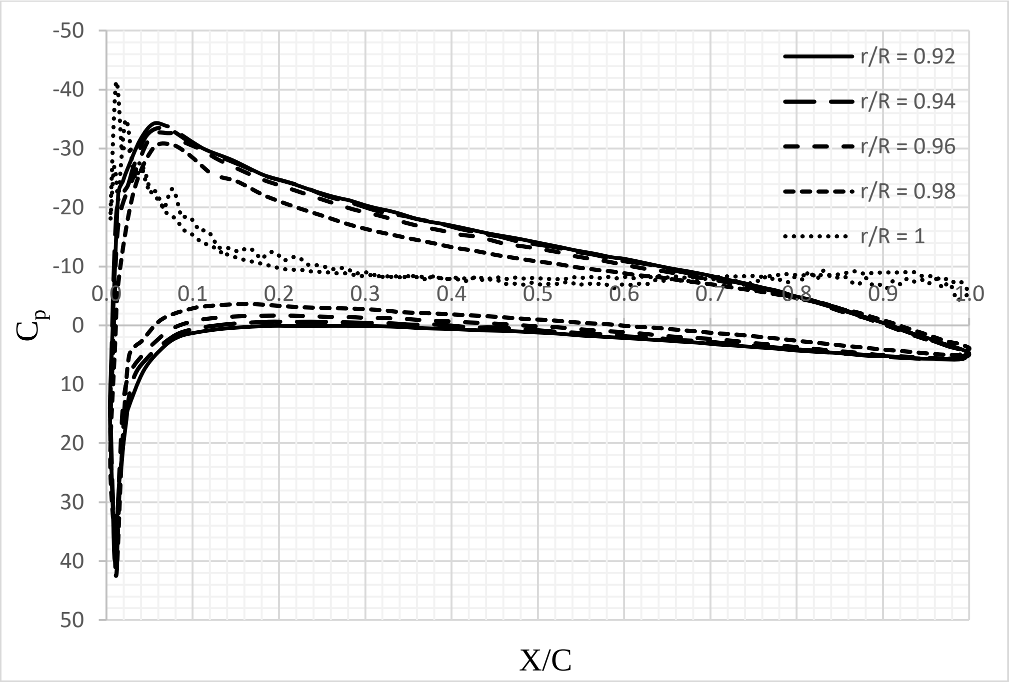

Figure 6.6: Pressure coefficient distribution over different sections at U=8m/s and λ=7 for blade without WL

6.3.2 The origin of tip vortex

Tip vortex generation starts from the leading edge of the blade tip. Its intensity and core location depend on the wind speed and tip speed ratio. The tip vortex variation along the blade thickness should be observed in order to study its origin. It is considered a direct signature of the chord-wise bound vorticity effect [61]. The tip vortex age (phase) can be described by azimuth angles (ϕ). Its formation starts from the leading edge as mentioned before while the complete vortex starts to leave the trailing edge is considered at azimuth angle =0^o. Therefore the vortex formation phases are considered a negative azimuth angles. Figure 6.7 shows the chord-wise vorticity component at ϕ = -5^o which is considered at the first 10% of the chord length. The figure shows a comparison between both λ=4 and λ=7 cases. For λ=4 case, one clockwise vortex is concentrated at the high pressure side and extends up to the low pressure side. For λ=7 case, there are one clockwise vortex is concentrated at the high pressure side while other counter clockwise is concentrated at the low pressure side. The rotor blade causes an inboard radial flow (towards the blade root) and it increases by the rotation speed increase as in the case of λ=7. This effect is maintained after vortex leaving the trailing edge and counteracts the expansion caused by the wake as mentioned by Micallef et al. [61]. Therefore, the appearance of two vortices in the case of λ=7 can be more explained by the radial velocity contours as shown Figure 6.8.

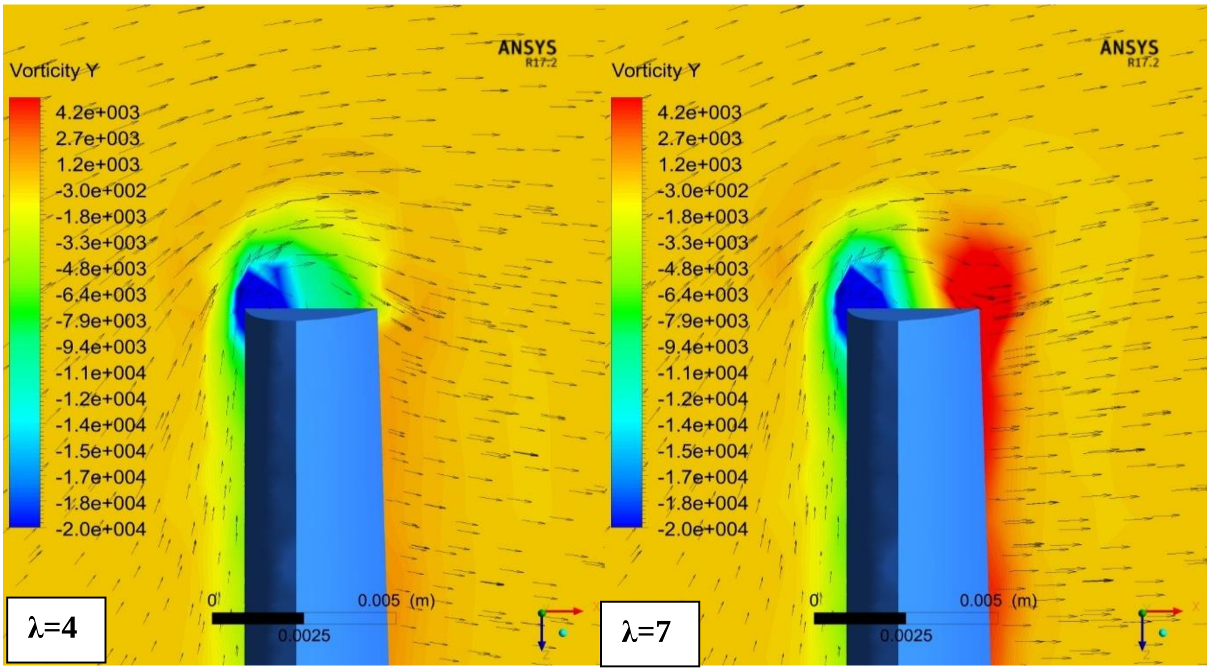

Figure 6.7: Chord-wise vorticity contours at -5º azimuth angle for rotor without WL

Figure 6.8 shows a concentration of an inboard radial velocity component of the flow at the middle of the tip thickness. The mentioned radial flow forces the clockwise vortex to concentrate at the high pressure side. It forms the counter-clockwise vortex due to relatively lower inboard radial flow downstream the rotor. Therefore the negative pressure concentration increases at the high pressure side of the blade. Thereby the tip vortex effect increases by the increase of λ as discussed before.

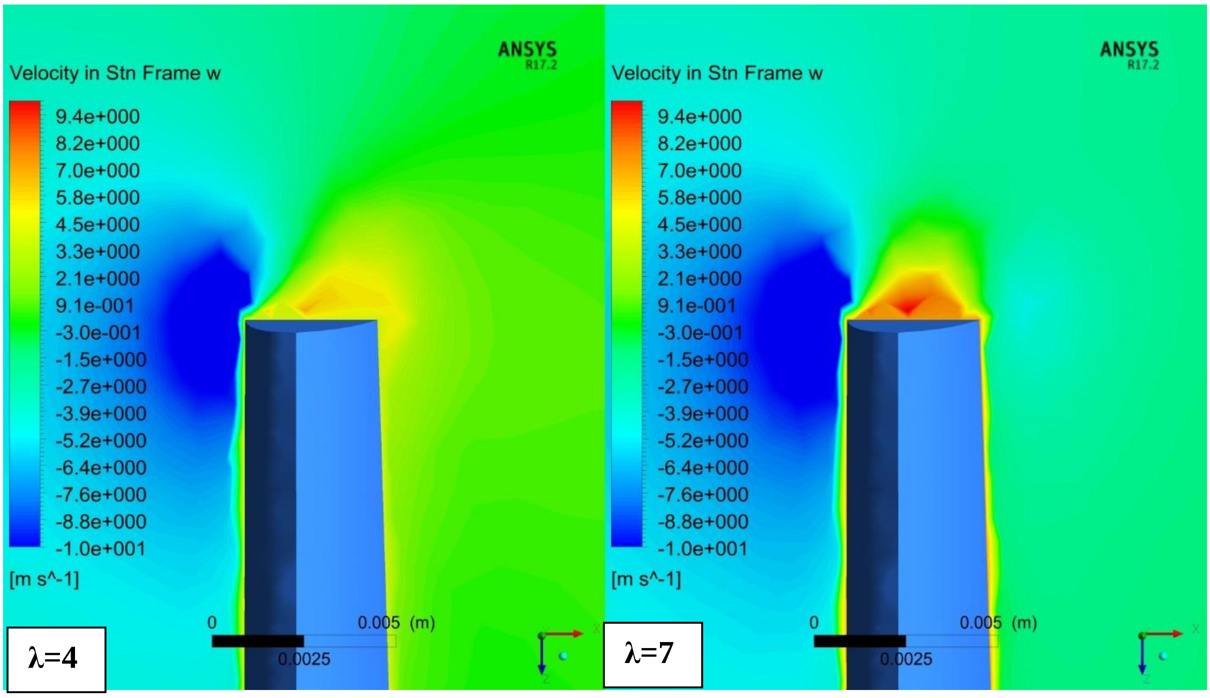

Figure 6.8: Radial velocity component contours at -5º azimuth angle for rotor without WL

At azimuth angle -3°, the counter-rotating tip vortices for λ=7 case are appeared as a one clockwise vortex as shown in Figure 6.9. The figure shows the vorticity shape and size for both of λ=4 and λ=7 cases. The vortex is appeared with a smaller size and higher intensity in the case of λ=7. Since, the inboard radial velocity component position moves downstream the rotor with smaller distance by comparison to the case of λ=4 as shown in Figure 6.10.

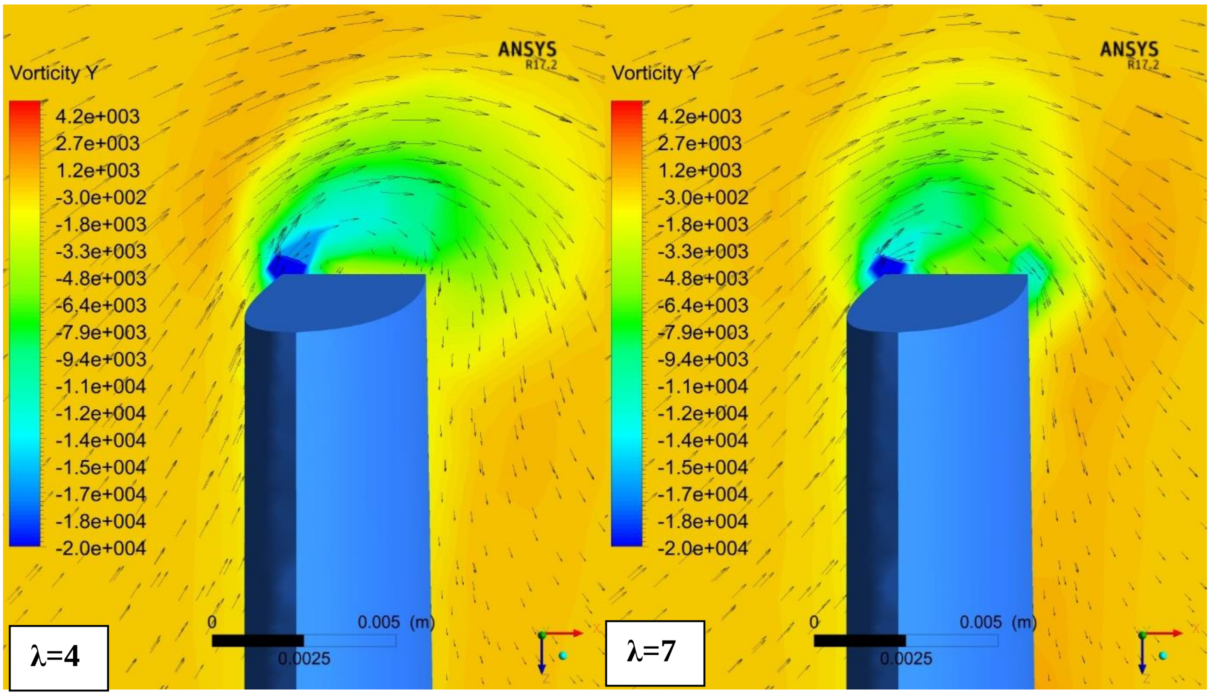

Figure 6.9: Chord-wise vorticity contours at -3° azimuth angle for rotor without WL

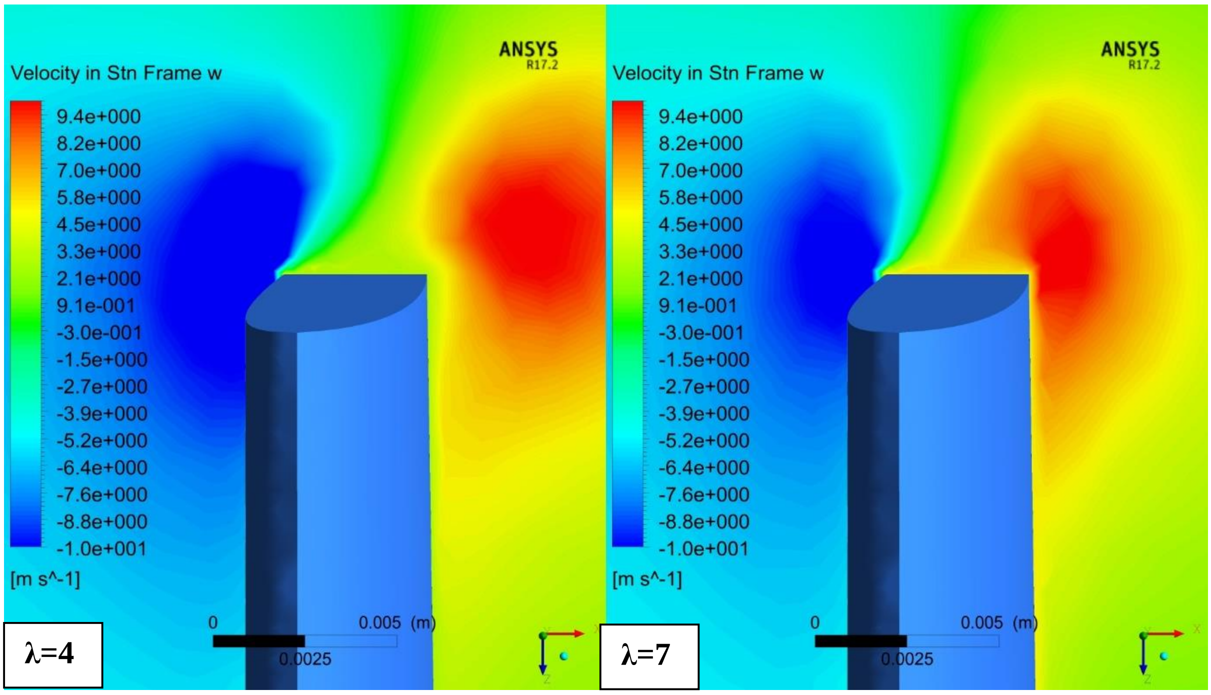

Figure 6.10: Radial velocity component contours at -3° azimuth angle for rotor without WL

At 0° azimuth angle, the tip vortex starts to leave the trailing edge for both of λ=4 and λ=7 cases as shown in Figure 6.11. The figure shows that the vortex of λ=7 case has smaller size and higher vorticity by comparison to the case of lower λ. The phenomenon was explained before by the closure of the inboard radial velocity components to the rotor. Since, the rotor panels effect increases by the increase of l as mentioned by Micallef et al. [61].

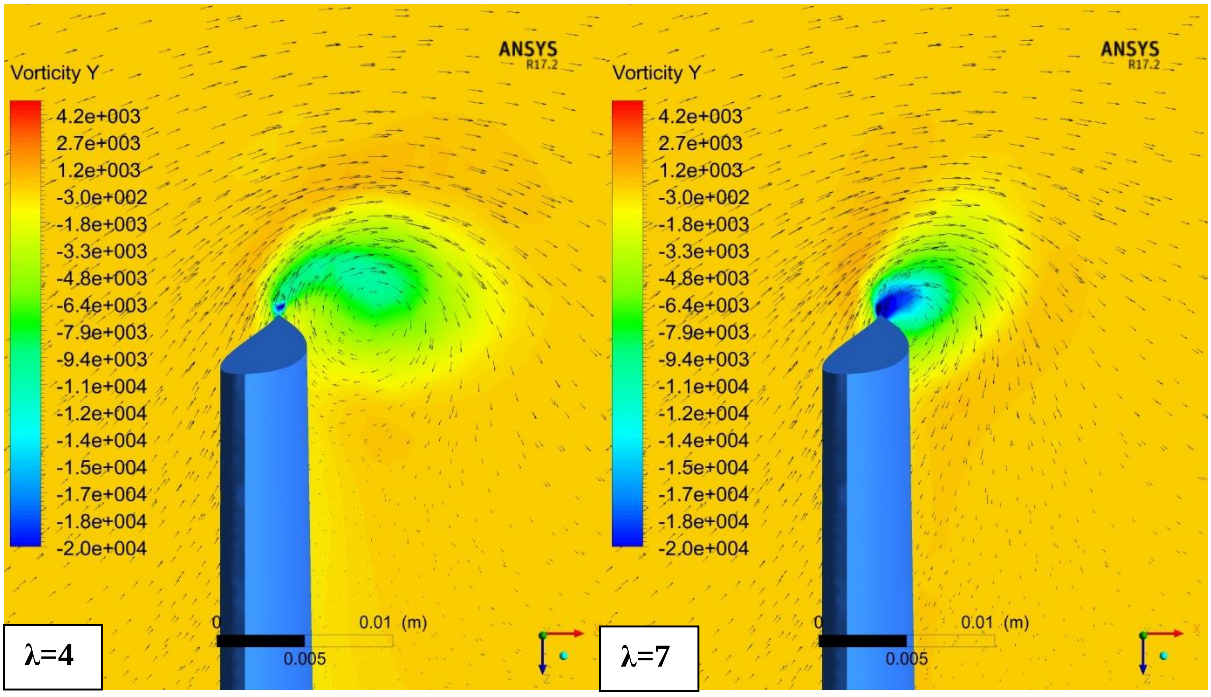

Figure 6.11: Chord-wise vorticity contours at 0° azimuth angle for rotor without WL

Therefore, the need of a device to reduce the effect of tip vortex is shown to be very important. Winglet is a successful device used to overcome such reduction in the lift at the tip of the blades as it will be demonstrated in Figure 6.26 . The concept of adding WL to the blade tip is used in order to diverge and push the tip vortex away from the blade tip. The WL height is selected to be studied firstly to get the optimum height that is suitable for the vortex size. On other hand, adjusting WL toe angle is selected to be the diversion tool for the tip vortex from the vortex origin, since, the vortex core is concentrated at the high pressure zone of the leading edge.

6.3.3 Effect of winglet height (H) on the rotor performance

The present study starts with WL height effect on power augmentation as an important parameter while keeping a constant cant angle of 90^0. The 90^0 cant angle is preferred in order to ensure that the power augmentation is only due to tip vortex divergence. Figure 6.12 represents the four upwind WLs with different heights and constant $\alpha_w = 0^o$ namely H=8%R, H=4%R, H=2%R and H=0.8%R. The used range is the most common range performed by many researches [17], [19] and [22].

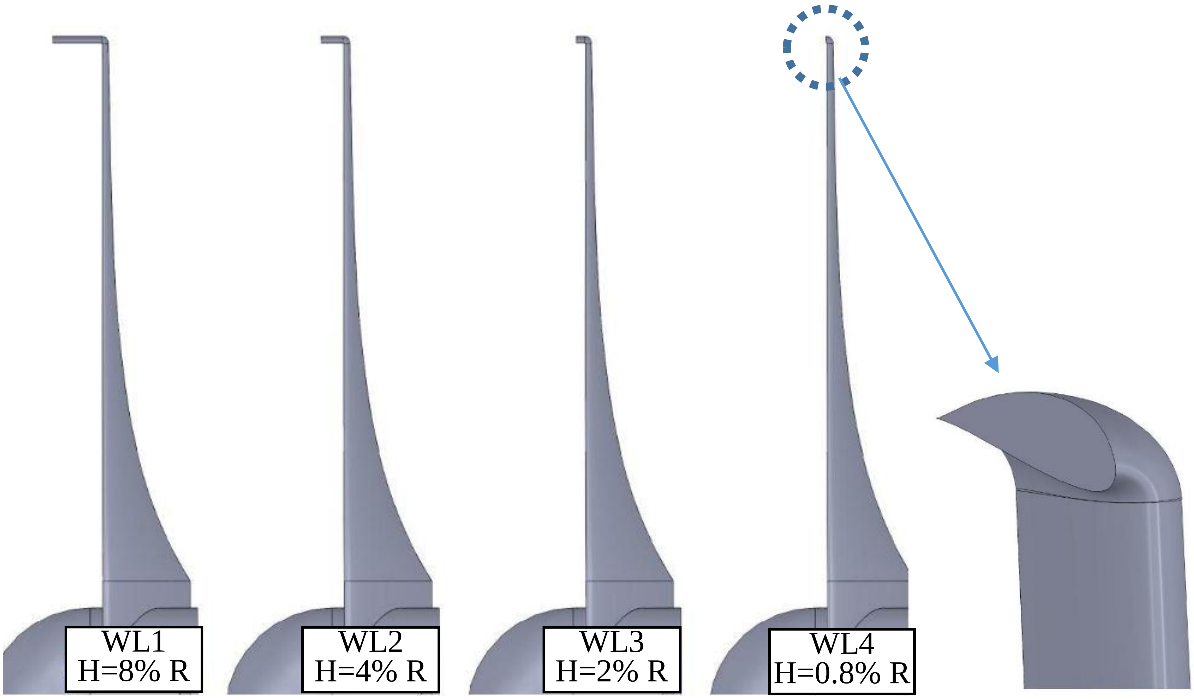

Figure 6.12 : WL configurations with different H and $\alpha_w = 0^o$

The purpose of WL height is to separate high pressure side from low pressure side at the blade tip. The WL reduces the tip vortex intensity and keeps the high pressure wind on the pressure side especially for upwind configurations. The extra surface of an increased WL height causes increased drag force. Upwind configurations increase axial thrust by comparison to downwind configurations. Power and thrust coefficients are studied at four tip speed ratios 4, 5, 6 and 7 to show the effect of each configuration. It is the most common range for small scale HAWT rotors. Tip speed ratio variation is performed by rotation speed variation at constant wind velocity 8 m/s.

Figure 6.13 shows C_{pw} variation at different values of λ for different H. For λ=4, WLs of H= 8% R, H=4%R and H=2%R show a little increase in C_{pw} by about 0.6 % while WL of H=0.8% R shows increase in C_{pw} by 2.2%. The four WLs show better performance at λ=5 while starting from λ=6 WL of heights 8%R decreases C_{pw}. At the same value of λ, WL of H=4% R shows a decrease in augmentation of C_{pw} to be 1% while both of WLs of H=0.8% and H=2%R maintain the percent of augmentation. Both of 8%R and 4%R WLs continue to cause a decrease in C_{pw} by λ increase while 0.8%R and 2%R WLs increase C_{pw} by 2.4% and 1.2% at λ =7 respectively. There are a clear decrease in C_{pw} due to the use of larger height WLs at higher tip speed ratios. The reason for that is the increase of drag due to the use of WL with larger surface area (larger heights) at higher angular velocities. It is worth mentioning that the previous results of C_{pw} is obtained by normalizing the net power ($T_{net}\,\Omega$) with respect to the theoretical power can be gained from the swept area and free-stream velocity.

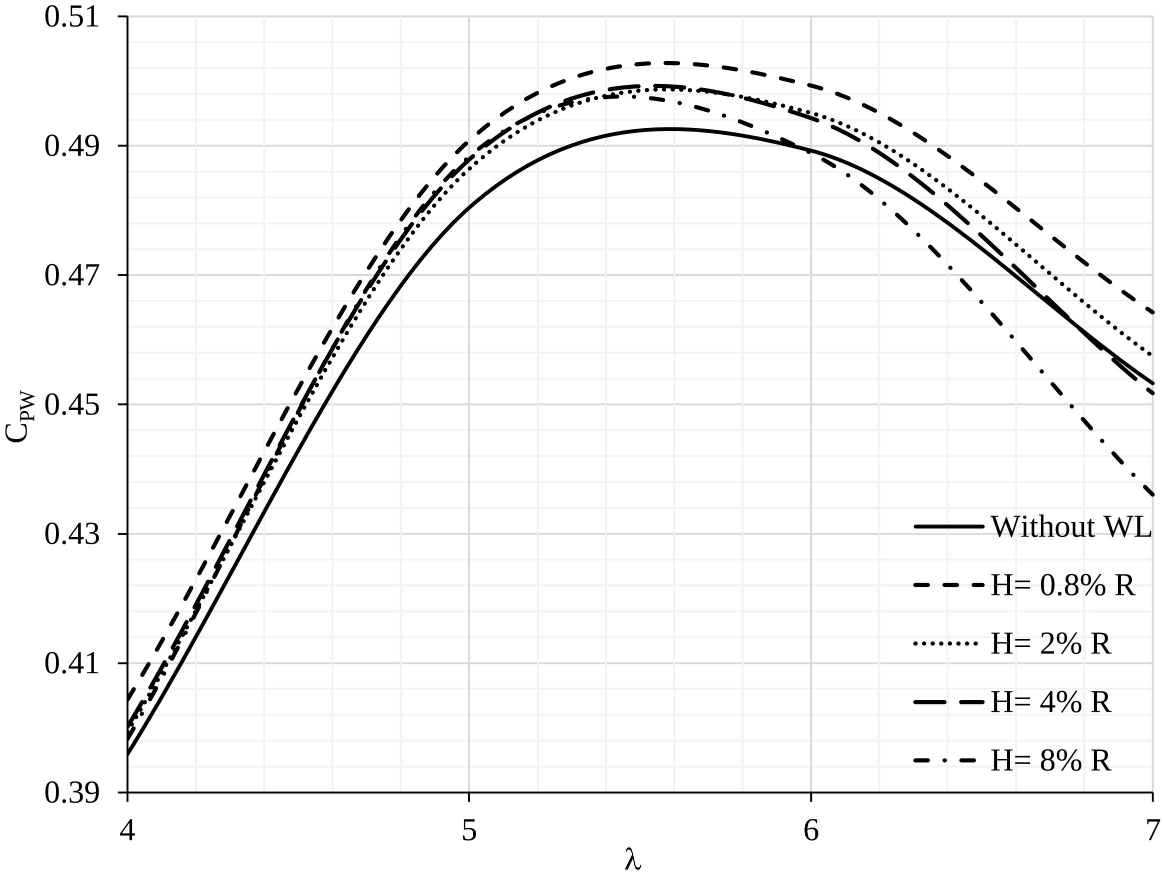

Figure 6.13: Power coefficient for WLs with different heights and α_w=0° at various values of λ

$$C_{pw} = \frac{T_{net}\,\Omega}{\frac{1}{2}\,\rho U_{\infty}^{3}\,A_d} \tag{6.1}$$

Where,

$$T_{net} = T_{lift} - T_{drag} \tag{6.2}$$

To show the influence of increasing the WL height on power coefficient reduction, the opposite torque due to drag is presented at the used range of λ. It is demonstrated in Figure 6.14 by friction power normalized with respect to the theoretical power.

$$C_{pw}^{drag} = \frac{T_{drag}\,\Omega}{\frac{1}{2}\rho U_{\infty}^{3}\,A_d} \tag{6.3}$$

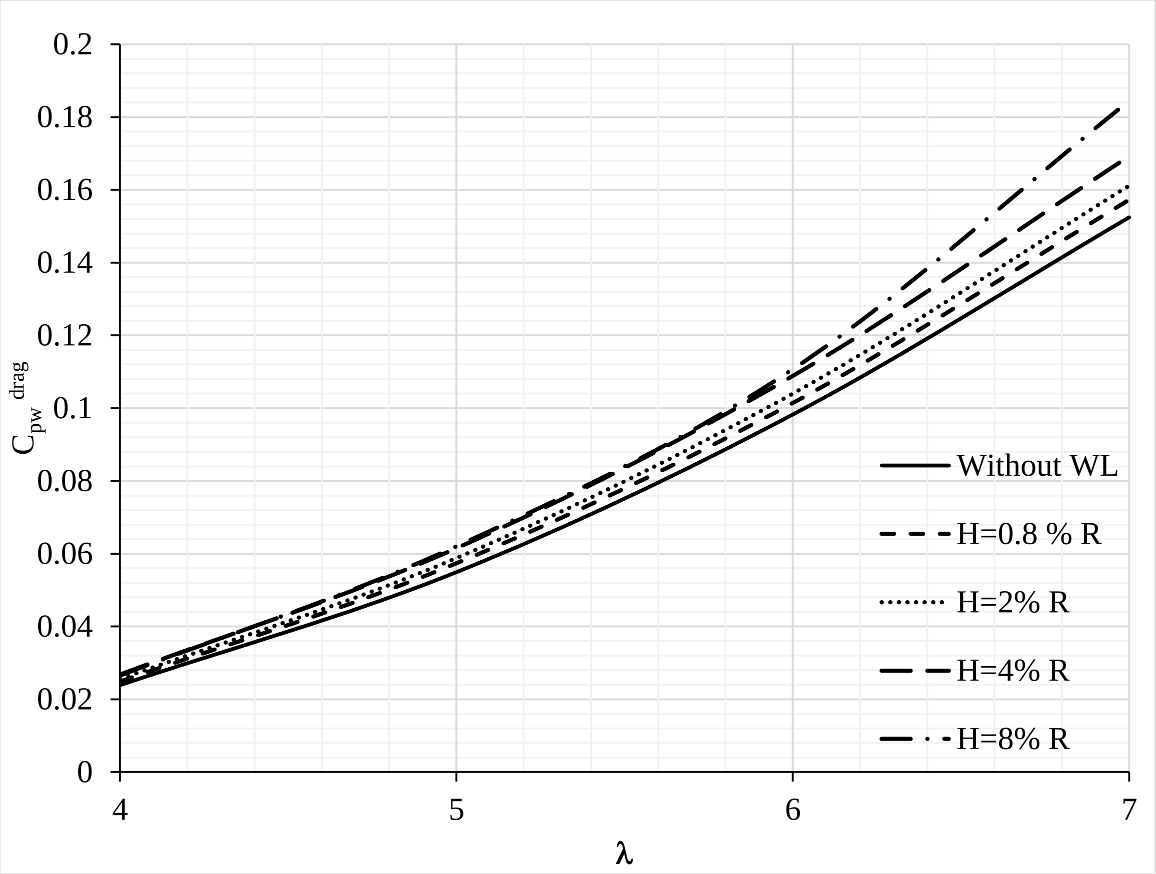

Figure 6.14: Power coefficient losses for WLs with different heights and α_w=0° at various values of λ

Addition of WLs with heights 0.8% R and 2% R increase the drag losses in power coefficient by about 3 % and 5.7 % respectively with respect to the drag C_{pw} of the nominal rotor at λ =7. WLs of heights 4%R and 8%R show the same effect till λ=6 since they increase the losses by 8%. The WL with H=8%R produces power coefficient reduction 21% at λ=7. The four used WLs increase the lift C_{pw} with the same percent at all values of λ approximately. It is possible to say that once adding any airfoiled WL with cant angle 90° and toe angle 0°

increase the pressure C_{pw} by 2.48% with respect to the pressure C_{pw} of the nominal rotor. It is concluded that increasing the height of the WL reduces the improved performance of adding the WL, due to the extra drag.

Considering the performance improvement by using WL without taking its influence on thrust coefficient into consideration isn't fair. Adding upwind WL increases thrust on the rotor while it improves the pressure distribution at the tip. The thrust increase due to the use of WL is shown in Figure 6.15 and had been demonstrated by several authors. Thrust coefficient increases by the increase of λ since, the rotor acts as a solid body that obstructs the flow at high tip speed ratios. Adding upwind WL concentrates extra positive pressure at the blade tip and increases the pressure difference across the rotor. Figure 6.15 shows that the WLs of H=0.8%R and H=4% R increase the thrust coefficient by 2.2% at λ=4 while the one of H=8%R increases C_T by 3.1 %. Thrust coefficient increases by λ increase as mentioned before since, WLs of H=0.8%R and H=8%R increase the C_T by 2.9% and 5.6% respectively at λ=7. It is noticed that C_T increases by the increase of WL height at all values of λ.

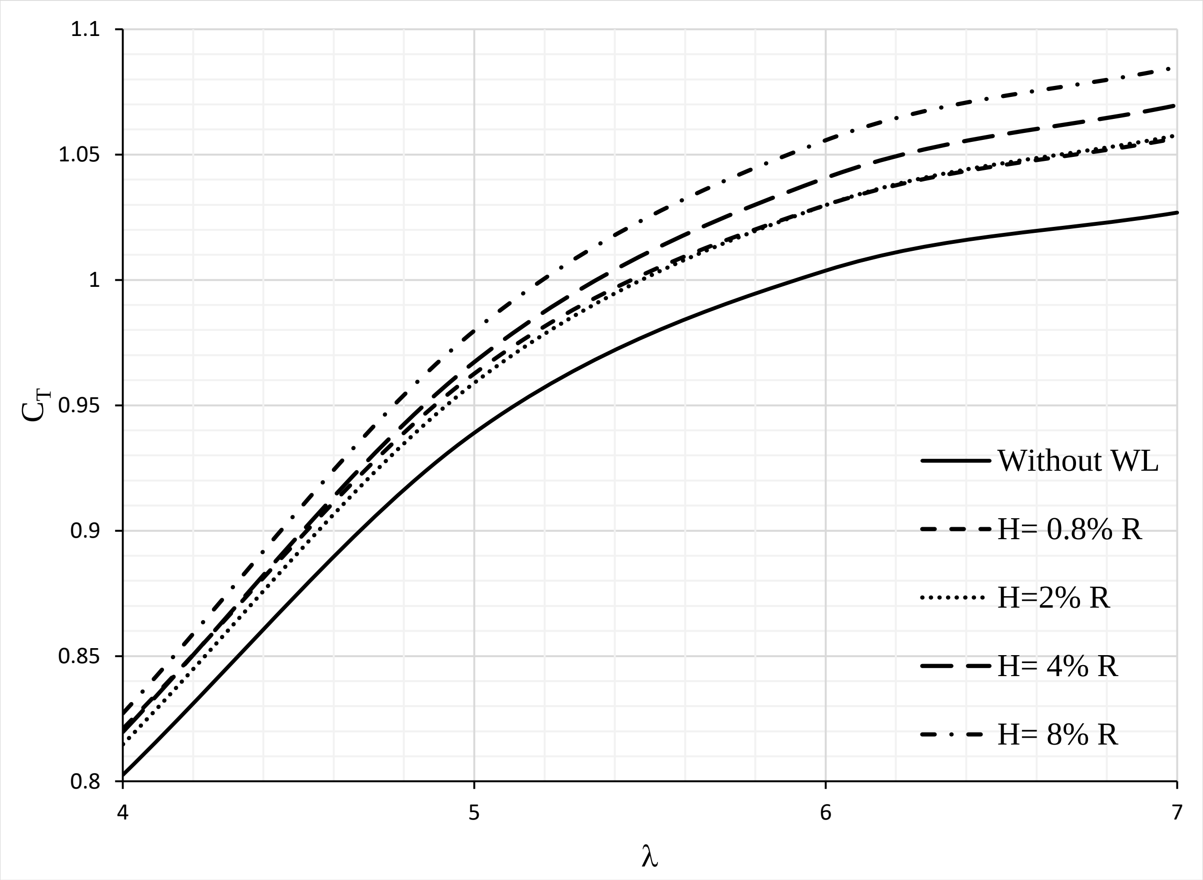

Figure 6.15: Thrust coefficient for WLs with different heights and α_w=0° at various values of λ

6.3.4 Effect of winglet height on the flow characteristics

The main purpose of using WL is to minimize the effect of the tip vortex or taking it away from the blade tip. Actually, the tip vortex consists of two regions, inner region and outer region. The part at which the viscous forces are dominant is called the inner part. The inner part rotates as a rigid body and the tangential velocity tends to zero at vortex center. At the outer part, the flow is similar to the potential vortex since, the tangential velocity decreases with the increase of radial position. The inner part is the vortex core. Its radius equals the distance between the vortex center and the position of maximum tangential velocity. The vortex center is the place at which tangential velocity tends to zero. Vortex definition and characteristics are given by Maalouf et al. [62]. The vortex core can be shown by the results of the present computations. It is described by the region with the low pressure values. Pressure contours are extracted at a blade tip from the CFD results of the present study and are shown in Figure 6.16. The vortex core is presented by the dark blue color at the blade tip or at the tip of the winglet. The figure shows the phenomena of low pressure region extends to upwind the rotor tip without WL. The tip vortex transfer the low pressure flow from downwind the rotor to its upwind side in the last 10% of the span. The problem is solved by adding WL with the minimum height of 0.8%R since it takes the vortex away from the blade tip and maintained the pressure difference on the blade surfaces.

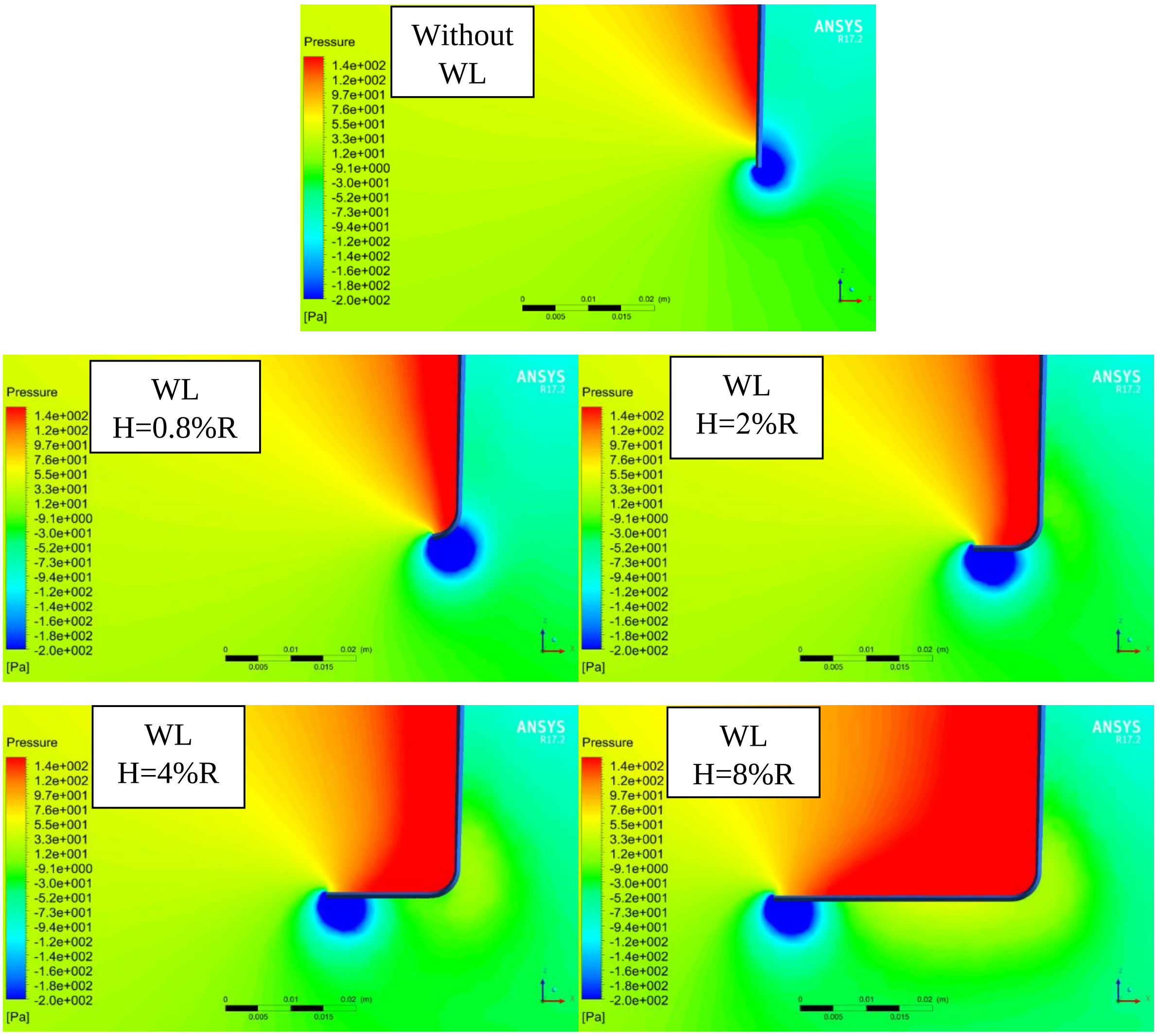

Figure 6.16: Pressure contours upwind and downwind the rotor with WLs of different heights and α_W=0^o at λ=7

Upwind WLs with longer heights make higher positive pressure concentration upwind the rotor as shown in Figure 6.16. Extra WLs heights will increase the induced drag and concentrate the positive pressure upwind the rotor as shown in the figure. The WL induced drag causes power losses and higher thrust values that are caused by high pressure difference across the rotor.

Although the WL of H= 2% R expected to have higher thrust relative to the WL of H=0.8% R, the results of C_T (Figure 6.15) showed that the WL of H=2% R has lower thrust relative to the WL of H=0.8%R at λ=4. Figure 6.17 for pressure contours at λ=4 gives a reason for the mentioned phenomena. The figure shows that the WL geometry of smaller height (H=0.8% R) moves the tip vortex core downstream the blade tip. Thereby very low pressure region is created downstream the blade tip which increases the pressure difference across the rotor and thereby increases the thrust. The demonstrated phenomena isn’t found at higher tip speed ratio case (λ=7) which is showed previously by Figure 6.16. At low tip speed ratio, the axial wind speed overcomes the radial velocity components of the flow and bends the tip vortex downstream the blade tip. The opposite is occurred in the case of high tip speed ratio which is known by wake expansion phenomena. Since, the wake expansion increases by the tip speed ratio increase.

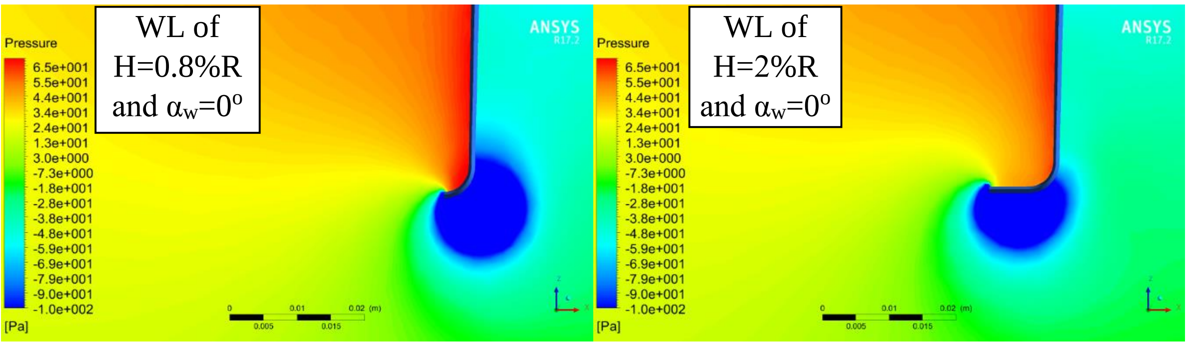

Figure 6.17: Pressure contours upwind and downwind the rotor at λ=4

Outer part of the tip vortex is considered a potential vortex as mentioned before. It can be noticed in more details by using tangential velocity vectors as shown by Figure 6.18. The figure gives more informations about vortex rolling direction too. It explores the effect of adding WL to the blade tip. The higher tangntial velocity values are presented by the dark red converged vectors. The tangential velocity decreases with distance outward the blade tip. Both of Figure 6.16 and Figure 6.18 show that the tip vortex diameter is less than the minimum WL height of 0.8% R. Therefore, the improvement in C_{pw} that mentioned before in Figure 6.13 is independent of WL height increase. WL takes the tip vortex away from the blade tip without any change in its formation.

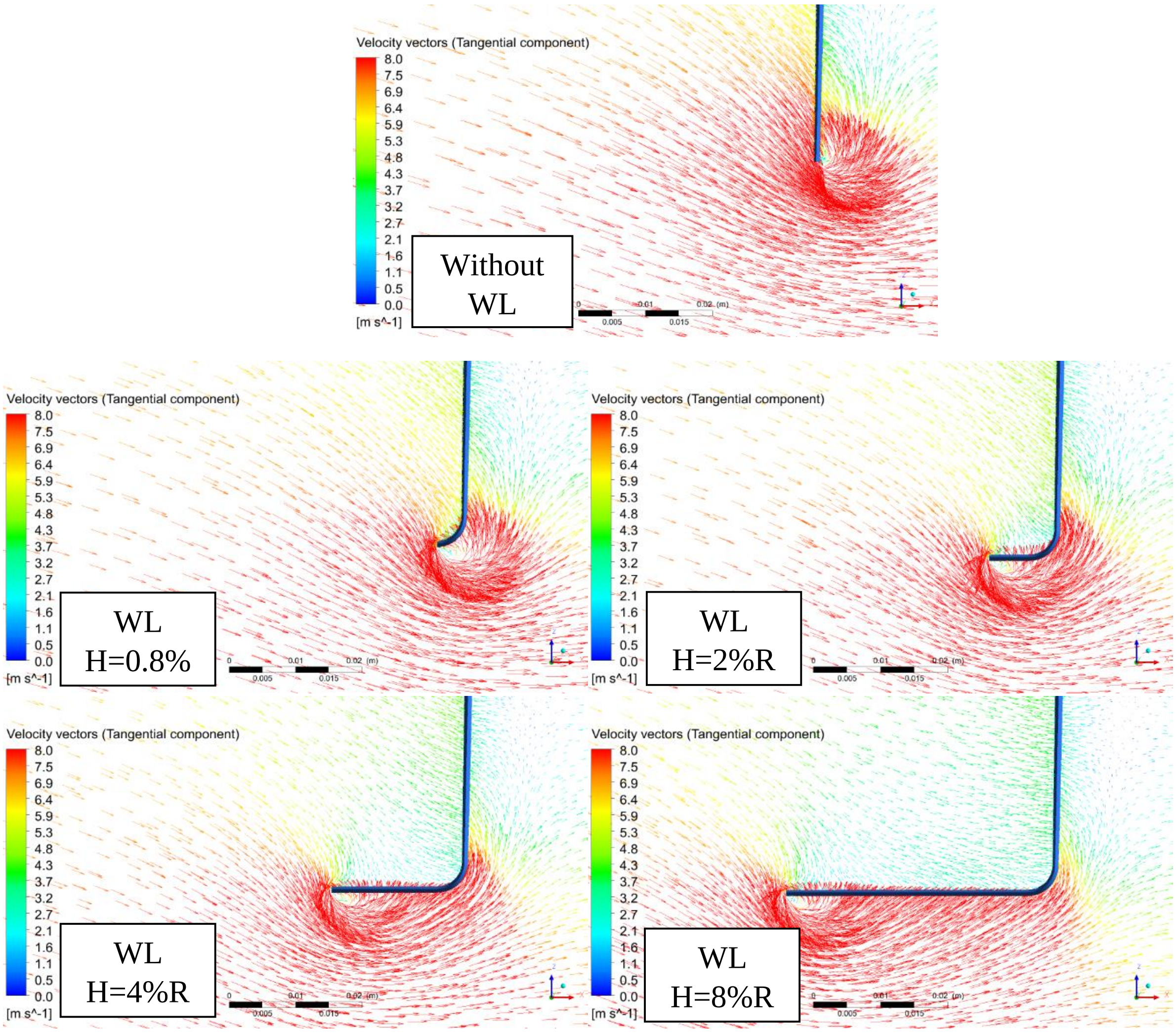

Figure 6.18: Tip vortex shape by tangential velocity vectors for upwind WLs with different heights and α_w= 0° at TSR=7

It is concluded from the previous results that the WL of H=0.8%R with toe angle 0° shows the highest C_{pw} values and lowest C_T values for all λ values.

6.3.5 Effect of winglet toe angle on the rotor performance

The present part of the study is performed on the wind turbine model with the WL of the best height (0.8%R) as proved before. Toe angle is the other important parameter studied. Toe angle is considered as the angle of attack (α_w) of the WL profile with respect to tangential velocity of air. All positive α_w winglets are upwind WL configurations while downwind WLs are of negative α_w as shown in Figure 6.19. The figure shows a sample of used winglets configurations with their toe angles. WL height is maintained constant for all cases and equal

0.8% R. Power and thrust coefficients values are calculated at the four tip speed ratios 4, 5, 6 and 7.

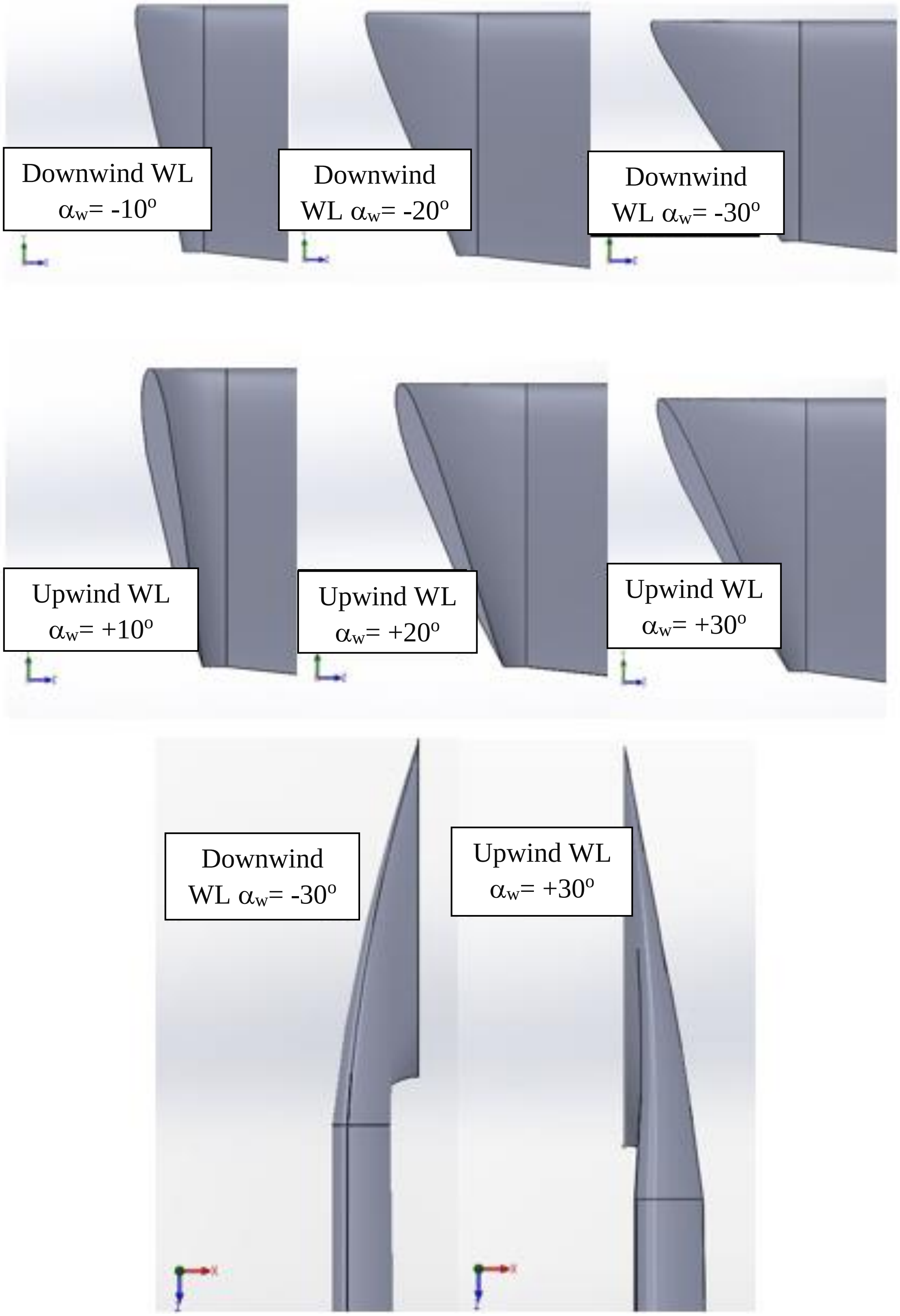

Figure 6.19: Winglets configurations with different toe angles and H=0.8%R

Upwind WLs configurations starting from α_w =0° show a very good performance for the rotor. Figure 6.20 and Figure 6.21 show a clear increase in C_{PW} and C_T for upwind WLs as compared to rotor without WL specially at λ=7. Augmentation in power is followed by increase in thrust as toe angle increases. Once α_w =0° WL is added, C_{pw} and C_T increase by 2% and 2.3% respectively at λ=4 and by 2.4% and 2.9% at λ=7. For +20° α_w WL, C_{PW} and C_T increase by 2% and 4.6% respectively at λ=4 and by 6 % and 9.8 % at λ=7. The WL of +30° α_w shows a lower power coefficient values up to λ=6. Therefore the WL of toe angle +20° α_w is recommended and considered as the best design used in the present study.

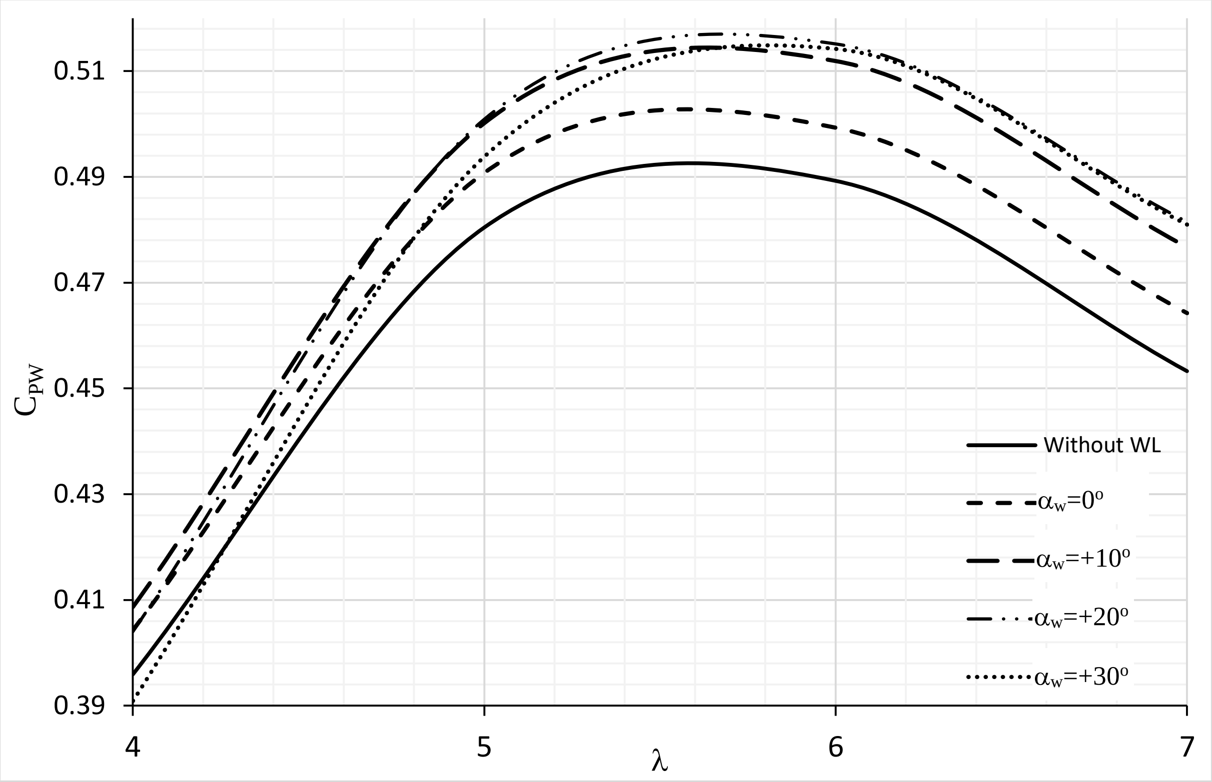

Figure 6.20: Variation of power coefficient using upwind WL with different toe angles and H=0.8%R at various values of λ

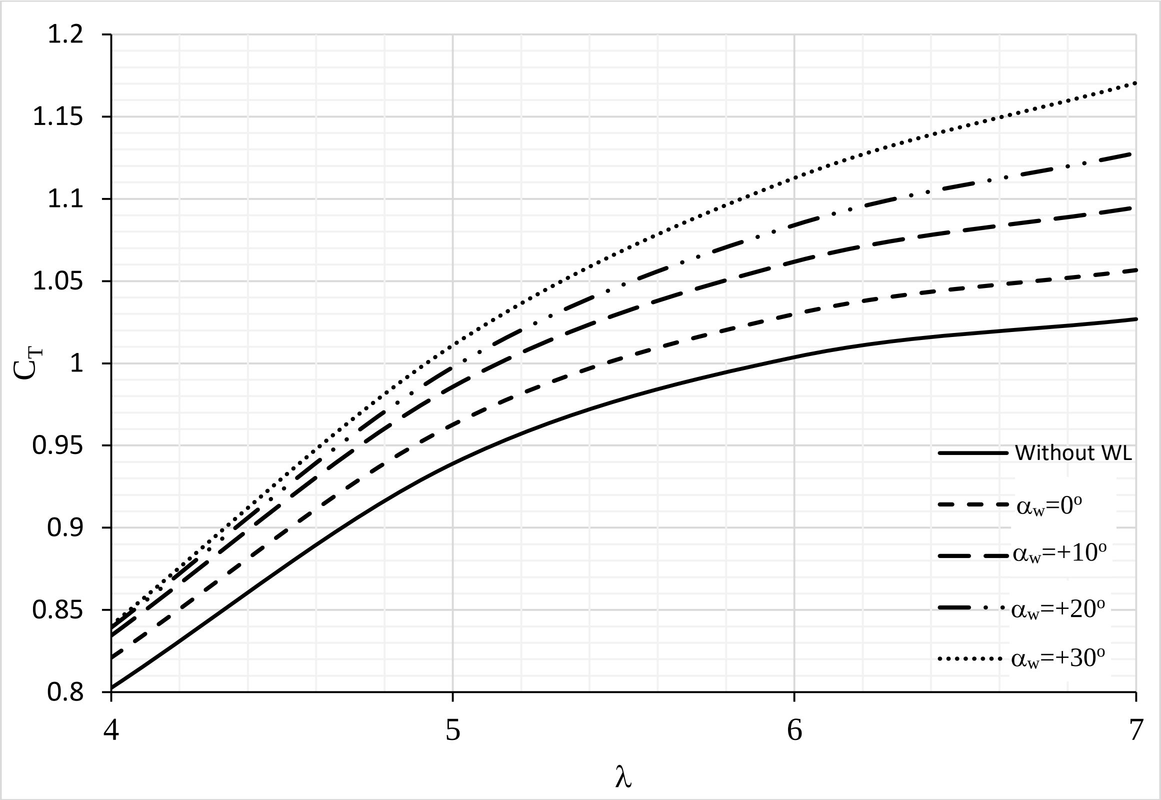

Figure 6.21: Variation of thrust coefficient using upwind WL with different toe angles and H=0.8%R at various values of λ

Upwind WLs produce high thrust due to its geometry as it is considered as an obstacle in front of wind flow. Upwind configurations are able to increase the extracted power due to tip vortex divergence as obviously shown in Figure 6.22. The used values of toe angle (positive values) make tangential flow stalls and directed to downstream by axial wind speed action. Stall phenomenon isn't preferred and should be avoided in WL design for planes [63] as they cause more thrust. In wind turbine case, stall phenomena cause induced drag which may cause a negative effect on extracted power. Axial wind speed reduces the effect of this phenomenon and pushes the tip vortex downstream far from the rotor as shown in Figure 6.22.

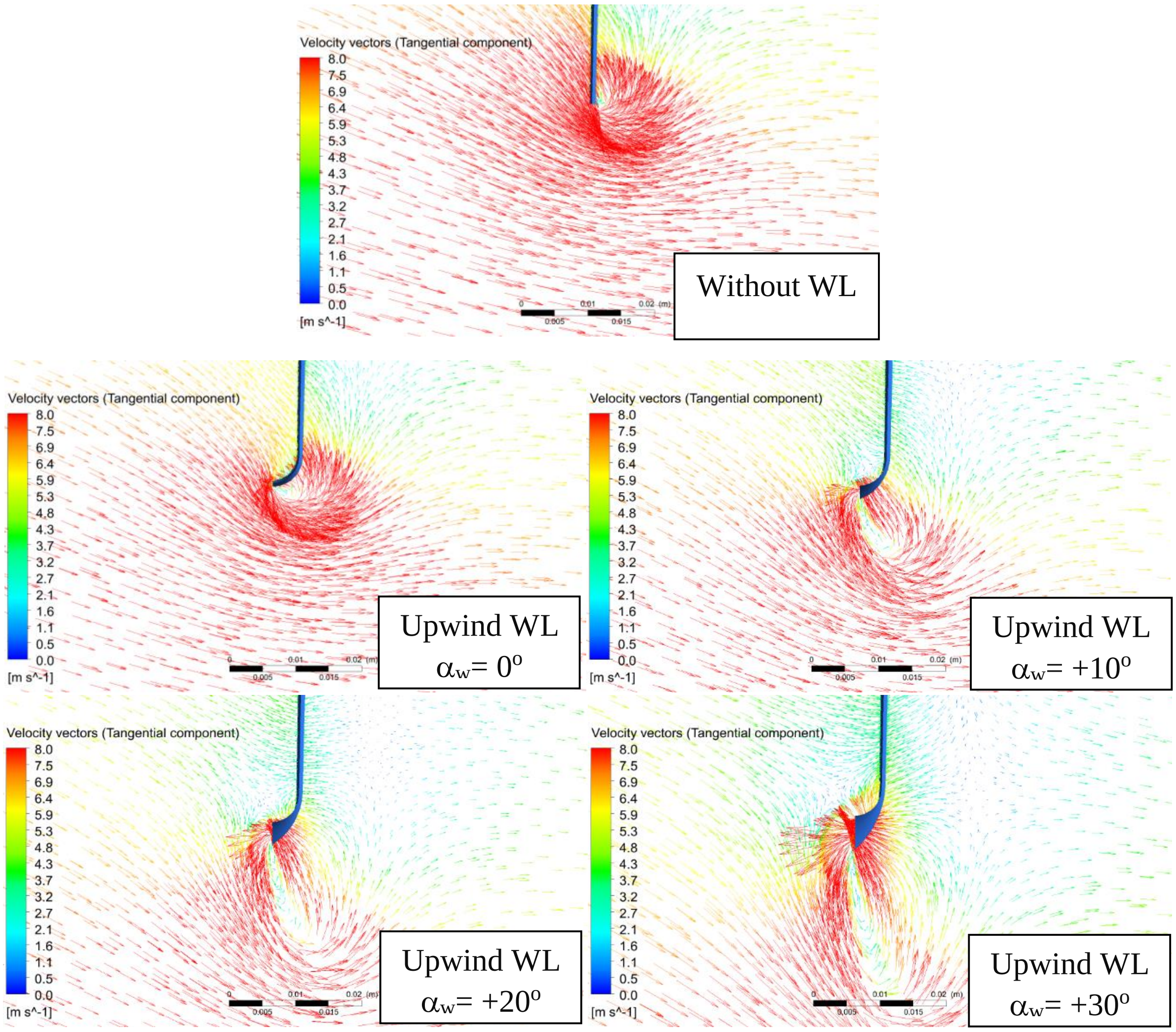

Figure 6.22: Tip vortex shape by tangential velocity vectors for upwind WLs with different toe angles and H=0.8%R at TSR=7

Figure 6.23 shows the effect of adding WLs with different negative toe angles on power coefficient. There is no augmentation in power due to adding WL with downwind configurations. The design of -10^o α_w shows almost the same performance of the rotor without WL up to $\lambda=6$ while it decreases the power by 1.7% at $\lambda=7$. WLs of $\alpha_w= -20$ and $\alpha_w= -30^o$ show that power coefficient decreases by tip speed ratio increase. It should be mentioned too that -10^o α_w downwind configuration have the same values of thrust coefficient for the rotor without WL. WLs of $\alpha_w = -20^o$ and $\alpha_w = -30^o$ decrease the thrust coefficient by tip speed ratio increase as noticed in Figure 6.24.

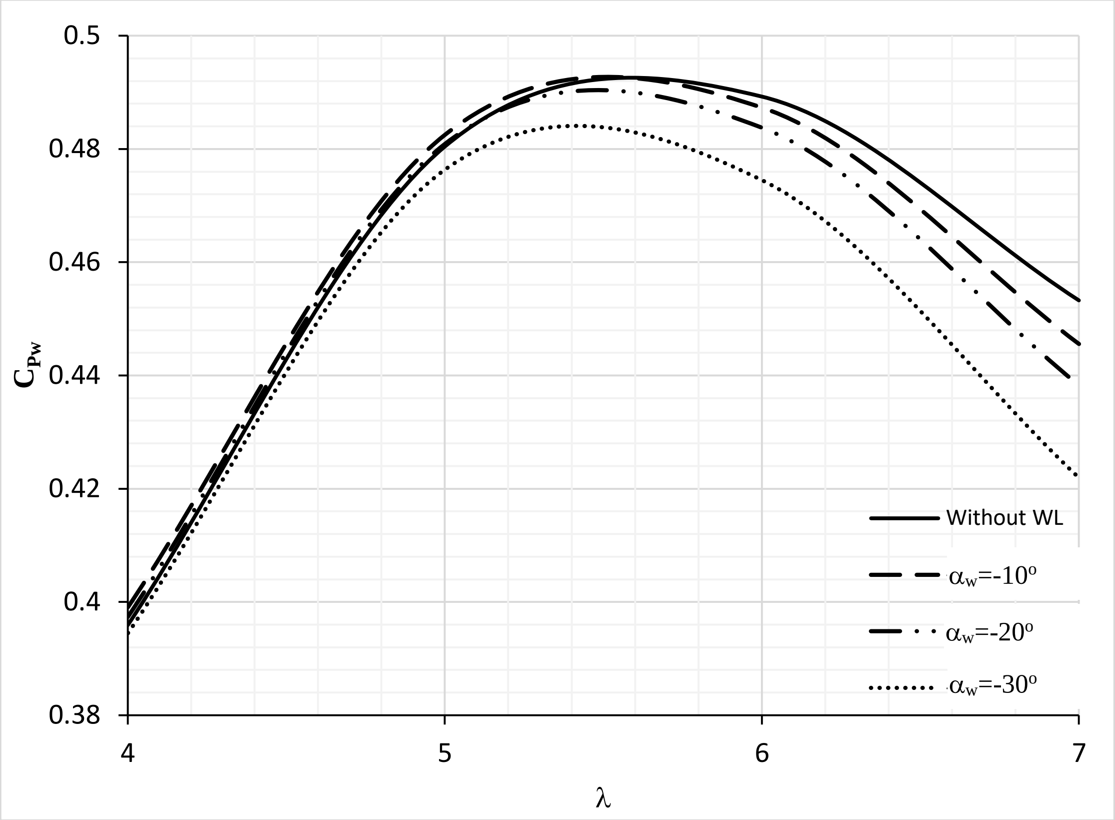

Figure 6.23: Variation of power coefficient using downwind WL with different toe angles and H= 0.8%R at various values of λ

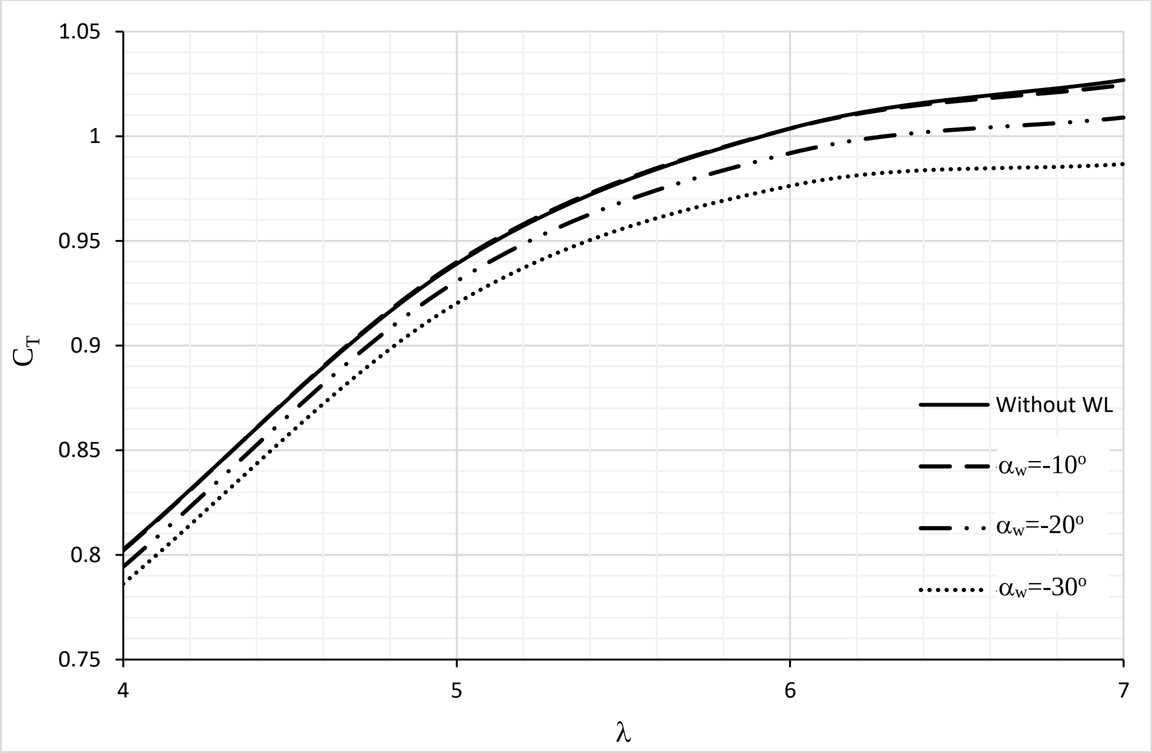

Figure 6.24: Variation of thrust coefficient using downwind WL with different toe angles and H=0.8%R at various values of λ

Figure 6.25 demonstrates tip vortex formation a round blade with and without WL. It shows vortex size around blade tip without adding WL covers up to about 1.5% R from blade tip. It confirms our previous results of the pressure coefficient curve with considerable reduction of pressure difference between high and low pressure sides starting from r/R =0.96 up to the blade tip as noticed in Figure 6.6. Downwind WLs strengthen the tip vortex and thus causes a reduction in C_{pw}. WLs of $\alpha_w = -10^o$, $\alpha_w = -20^o$ and $\alpha_w = -30^o$ increase the torque due to pressure difference by 2% and 3% respectively while they increase the drag torque by 6% and 12 % respectively .The power coefficient for downwind WLs decreases by λ increase. It is concluded that downwind WL isn't recommended

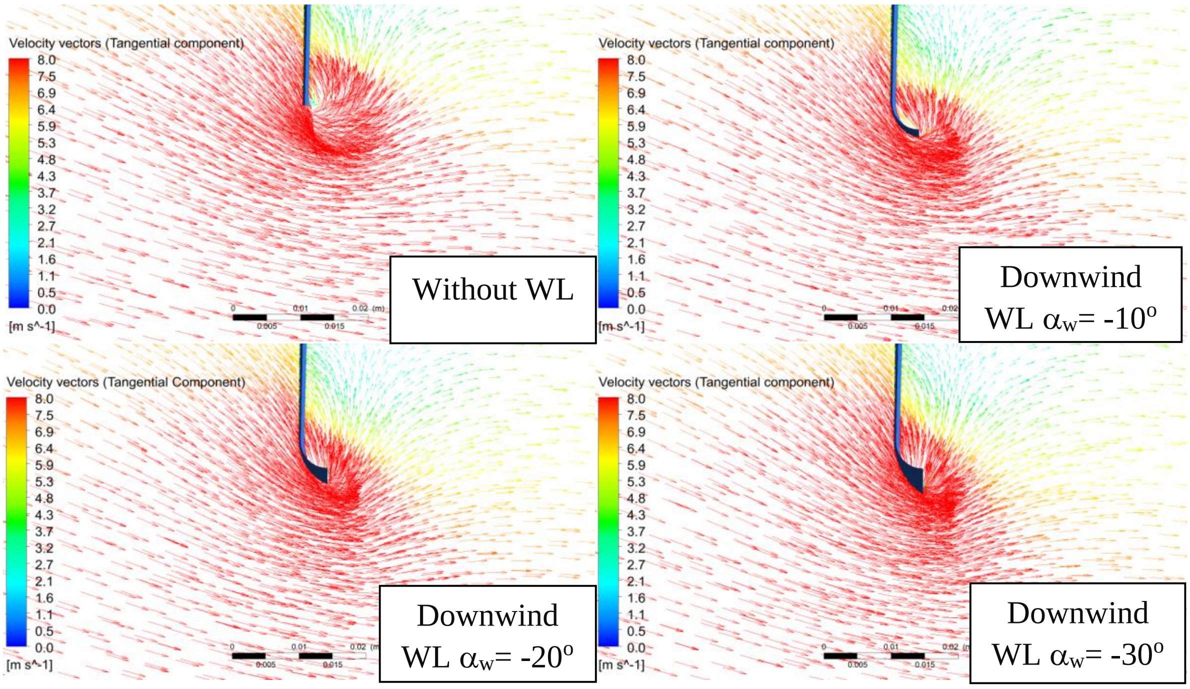

Figure 6.25: Tip vortex shape by tangential velocity vectors for downwind WLs with different toe angles and H= 0.8%R at TSR=7

6.3.6 Winglet effect on pressure coefficient distribution

Pressure coefficient distribution over the blade airfoil clearly shows the WL effect on the tip vortex. Figure 6.6 showed the effect of tip vortex on the last 6% of the blade length without WL. It is worth to compare these C_p results of the rotor with the most optimum WL of the study ($\alpha_w = +20^o$). Figure 6.26 shows the effect of adding the WL of $\alpha_w = +20^o$ on C_p distribution at the last four sections of the blade. The figure shows that adding WL of $\alpha_w = +20^o$ increases the pressure difference over the blade sections starting from r/R =0.94. The enhancement in the pressure difference increases and becomes more obvious near the blade tip. Therefore that is a conclusive evidence for the WL of $\alpha_w = +20^o$ action in diverging the tip vortex and pushing it away from the blade.

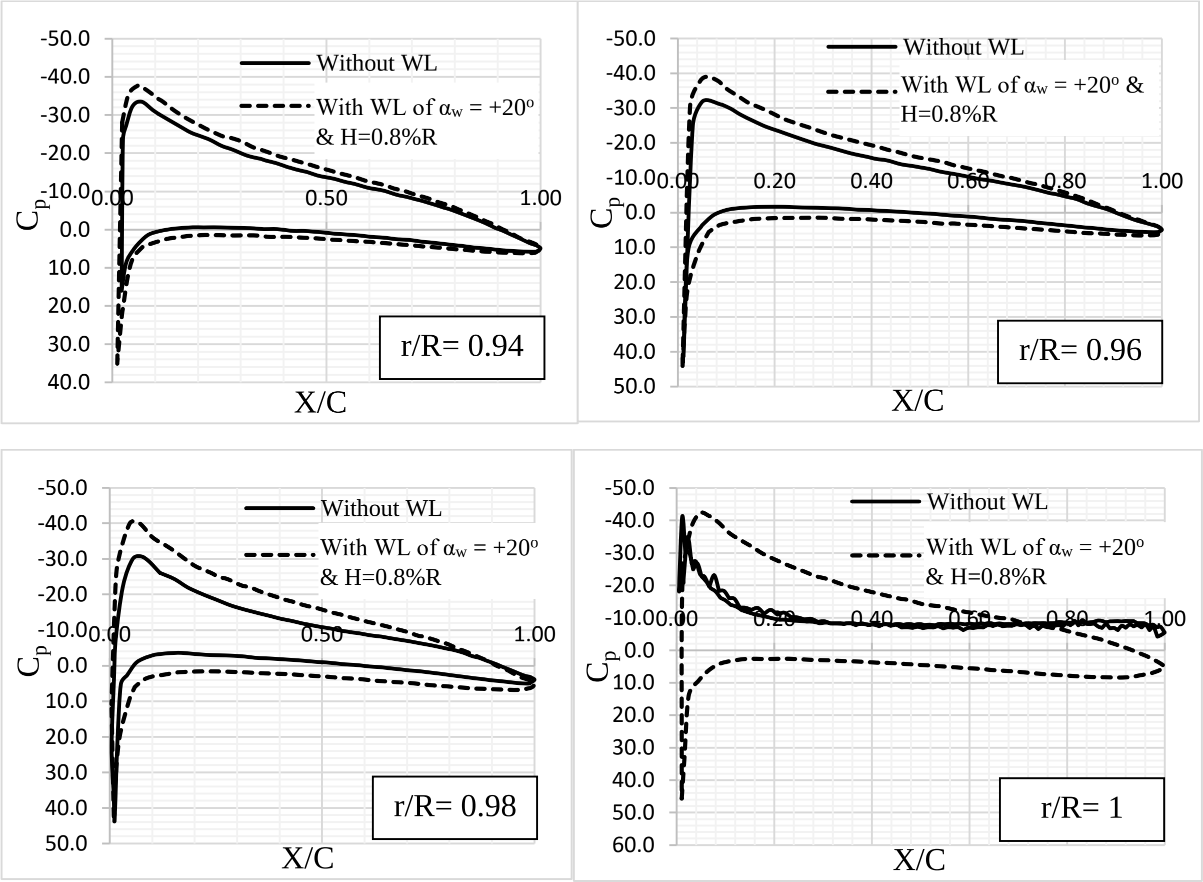

Figure 6.26: Pressure coefficient distribution over different sections at U=8m/s and λ=7

6.4 Wind turbine wake study

The wind turbine wake region can be divided to two regions namely near wake and far wake. The near wake extends from the rotor to approximately 2R downstream while the far wake region extends up to 20R or further; Sanderse [8]. The flow field in the near wake is considerably affected by the turbine geometry while the far wake flow isn’t sensitive to it.

The present section addresses the study of wind turbine wakes numerically with and without winglets. It is an investigation of the WLs effect on wake dynamics and stream-wise velocity deficit. The velocity deficit gives informations about wake expansion and rotor thrust. The present study covers the wake region up to 5.4R downstream the rotor.

6.4.1 Effect of WLs on velocity deficit

Four WLs are selected to study their effect on the rotor wake namely WLs of H=8%R, H=0.8%R, α_w=+20° and α_w=-30°. They are selected based on their performance, since the WL of α_w=+20° showed the best performance in the study while the WL of α_w=-30° showed the worst performance. For WL height study, the WL of H=0.8%R and α_w=0° showed better performance than the one of H=8%R.

Figure 6.27 shows the effect of adding WL of H=8%R on the velocity deficit (U_∞-U_w) profiles downstream the rotor at λ=7. Velocity deficit profiles give informations about the thrust that is created by the rotor. The WL of H=8% R caused an increase in thrust coefficient by 5.6% which is followed by increase in velocity deficit by 9% of the free-stream velocity at X/R= 0.1 in the case of λ=7. The maximum change in velocity deficit is pronounced at the outer portion of wake, at r/R from 0.8 to 1.1. The change in velocity deficit decreases by downstream distance from the rotor and the region at which the change is occurred expands till reach r/R=1.4. The expansion in the outer portion is occurred due to the expansion in the mixing region.

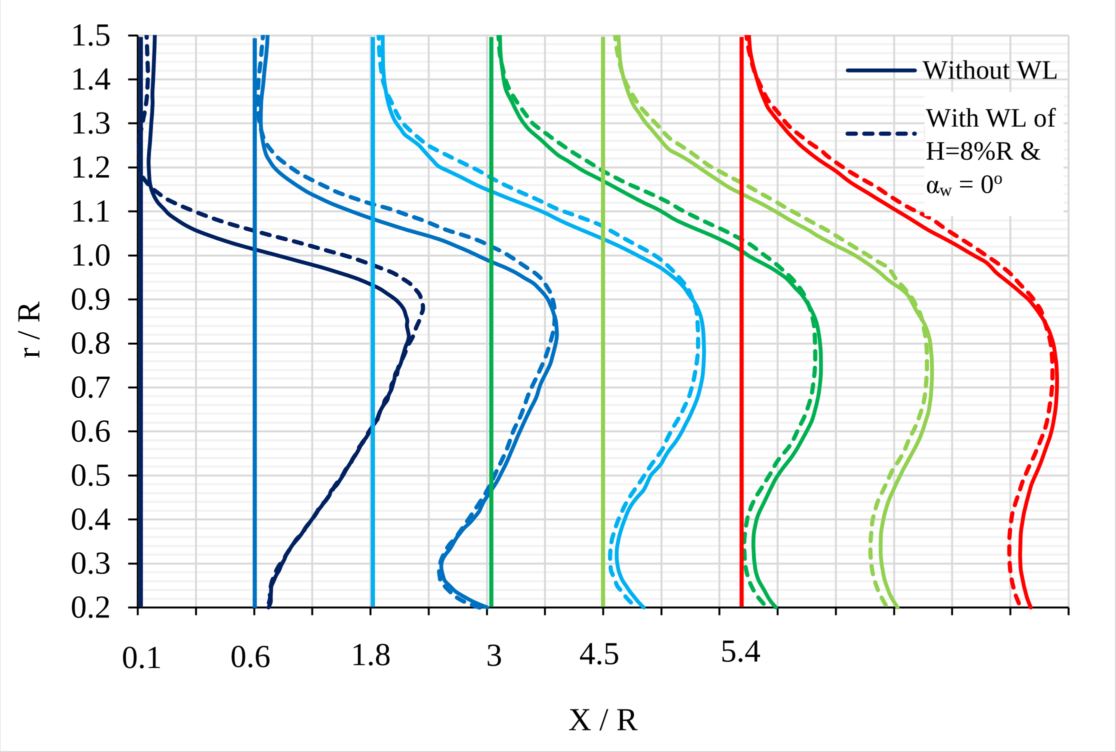

Figure 6.27: Stream-wise velocity deficit profiles for the rotor without WL and with WL of H=8%R and α_w= 0° at λ=7

Figure 6.28 shows the effect of adding WL of H=0.8%R on the velocity deficit profiles downstream the rotor at λ=7. It increases the velocity deficit by 4.2% of the free-stream velocity at X/R=0.1 downstream the rotor. From the C_T results, it increased the thrust by about 2.9% at λ=7. The WL of H=0.8% has lower velocity deficit than the one of H=8% R which is caused by the decrease in thrust.

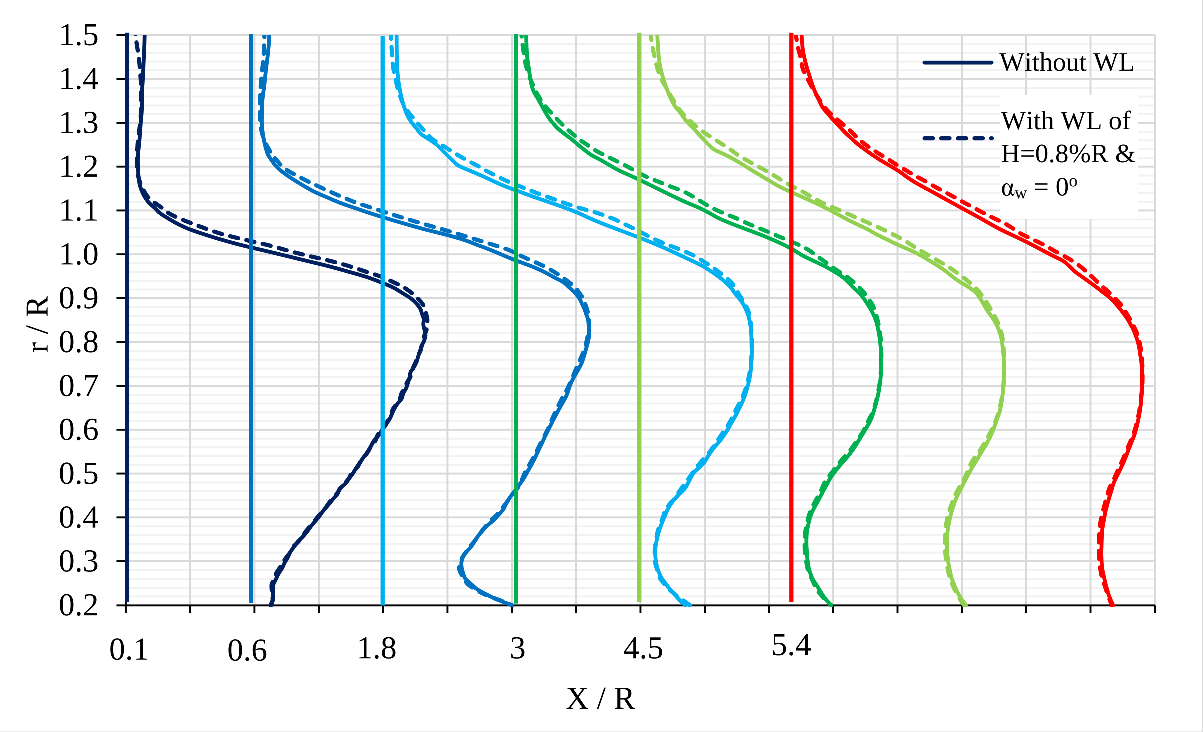

Figure 6.28: Stream-wise velocity deficit profiles for the rotor without WL and with WL of H=0.8%R α_w= 0° at λ=7

The WL of α_w =+20° increased thrust by 9.8% at λ=7 which is followed by increase in velocity deficit in the wake by 18% of the free-stream velocity as shown by Figure 6.29. The WL effect maintains constant downstream the rotor by expansion in the mixing region. The expansion increases in the case of this WL since, the mixing region is between r/R=0.7 and r/R=1.4 at X/R=5.4.

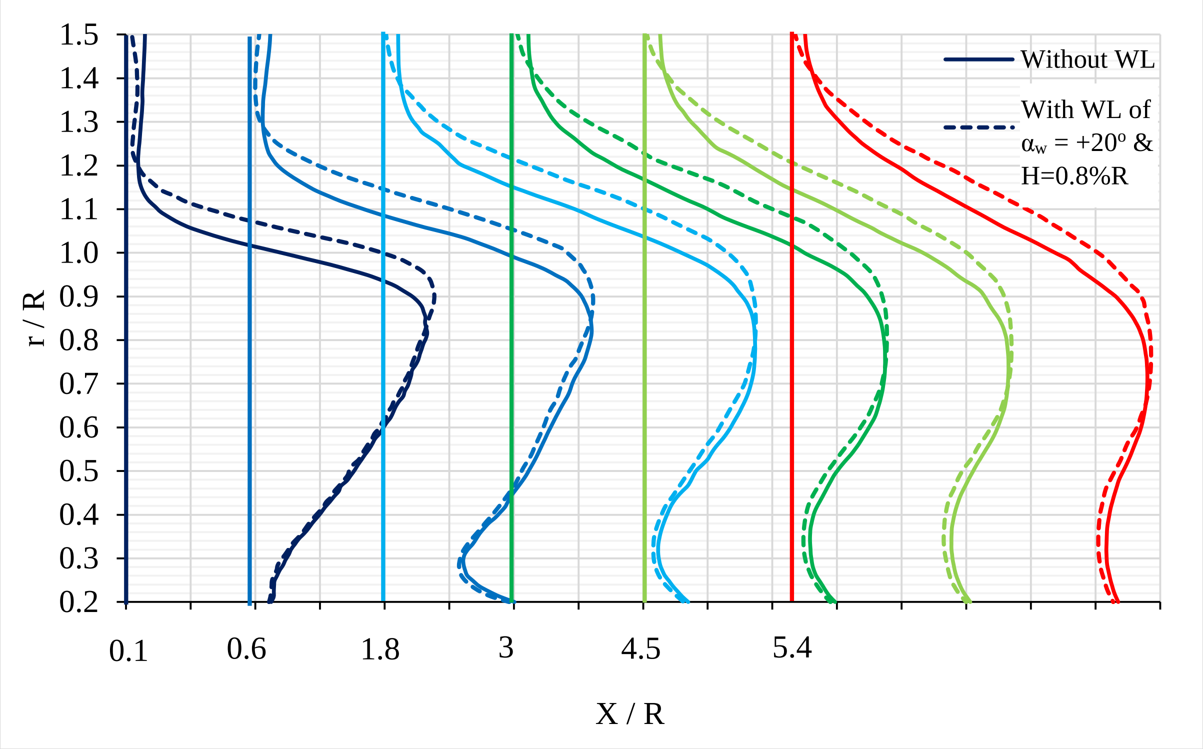

Figure 6.29: Stream-wise velocity deficit profiles for the rotor without WL and with WL of α_w= +20° and H=0.8%R at λ=7

Although the WL of α_w= -30^o decreased the thrust as discussed before, it increases the velocity deficit by 4.5% at λ=7 as shown by Figure 6.30. Since it is a downwind WL, it helps the flow to stream from upwind to downwind the rotor due to its curvature towards the downwind direction as shown previously by Figure 6.25. It reduces the high pressure concentration upwind the rotor, therefore it reduces the thrust.

The results of the velocity deficit are in a good agreement with Tobin et al. [24] except the case of WL of α_w= -30^o. The authors found a non-negligible increase in the velocity deficit profile in the near wake region due to 15% increase in thrust. The four WLs cause increase in the velocity deficit at the outer portion of the wake. It is called the wake mixing region which expands by the downstream distance from the rotor.

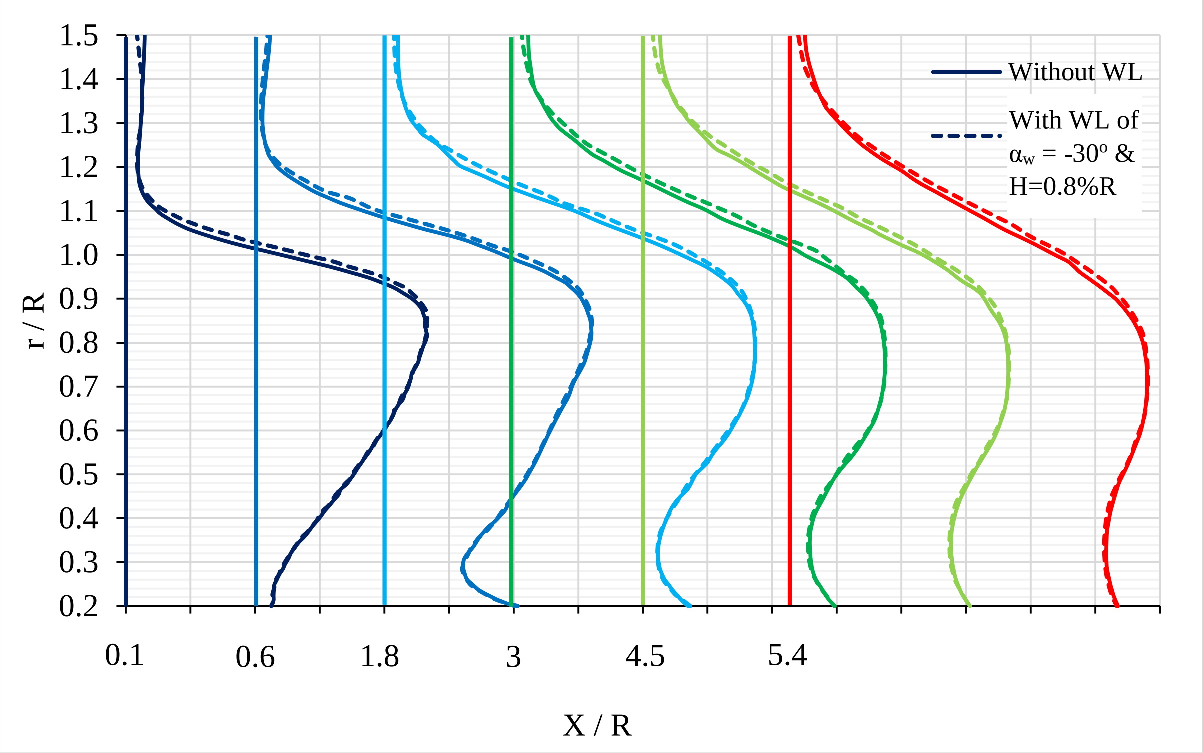

Figure 6.30: Stream-wise velocity deficit profiles for the rotor without WL and with WL of α_w= -30^o and H=0.8%R at λ=7

Wake mixing region is concentrated in the outer portion of the wake as shown by Figure 6.31. It is the region at which the Reynolds stresses are dominant. It is responsible for turbulent mixing and re-energizing process. For more details, Reynolds shear stress profiles should be studied and taken into consideration.

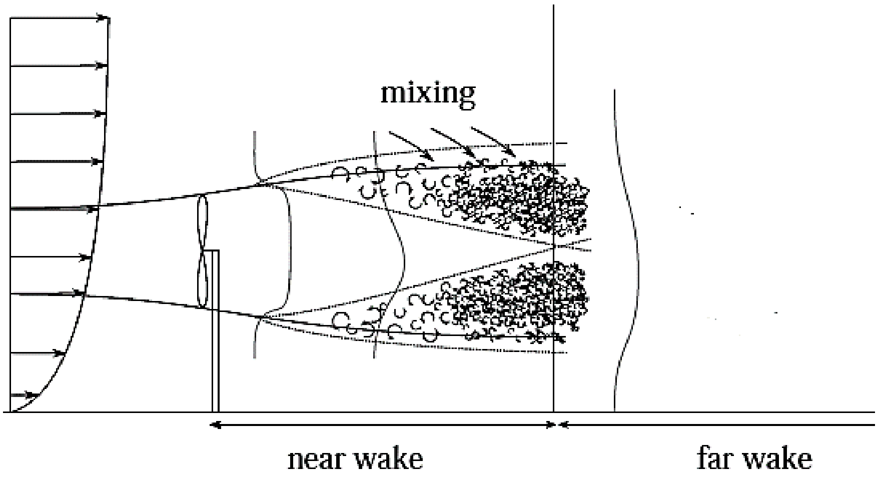

Figure 6.31: Wake mixing region and transition between near and far wake [8]

6.4.2 Effect of WLs on Reynolds shear stress

Reynolds shear stress profiles give more details about the mixing region. It is the region which separates between the free-stream and the inner wake region. Figure 6.32 shows the Reynolds shear stress profiles at different sections downstream the rotor without WL and with the WL of H=8%R. At downstream distance 0.1 R, shear stress profile shows maximum value at r/R=1 for the rotor without WL. The WL of H=8%R reduces the shear stress at the tip region by comparison to the rotor without WL and moves the point of maximum shear far away from the blade tip. The mixing region may be divided to two regions, one is upper than r/R=1.1 and the other one is lower than r/R=1.1. At the lower region, the rotor with WL of H=8%R decreases the shear stress while at the upper region, it increases the shear stress.

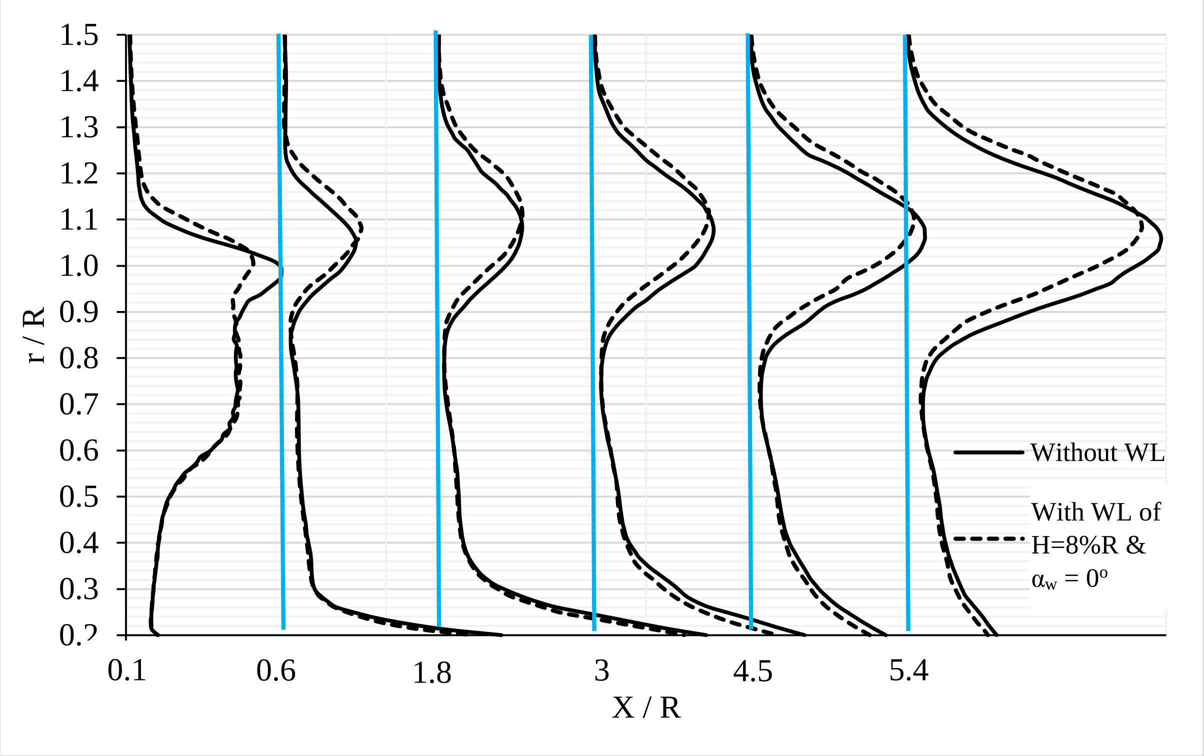

Figure 6.32: Reynolds shear stress profiles for the rotor without WL and with WL of H=8%R and α_w= 0º at λ=7

The WL of H=0.8% R shows the same Reynolds shear stress profile by comparison to the rotor without WL as shown by Figure 6.33. Although it doesn't affect the near shear profiles, it reduces the shear in the lower part of the mixing region at distances 4.5 R and 5.4 R.

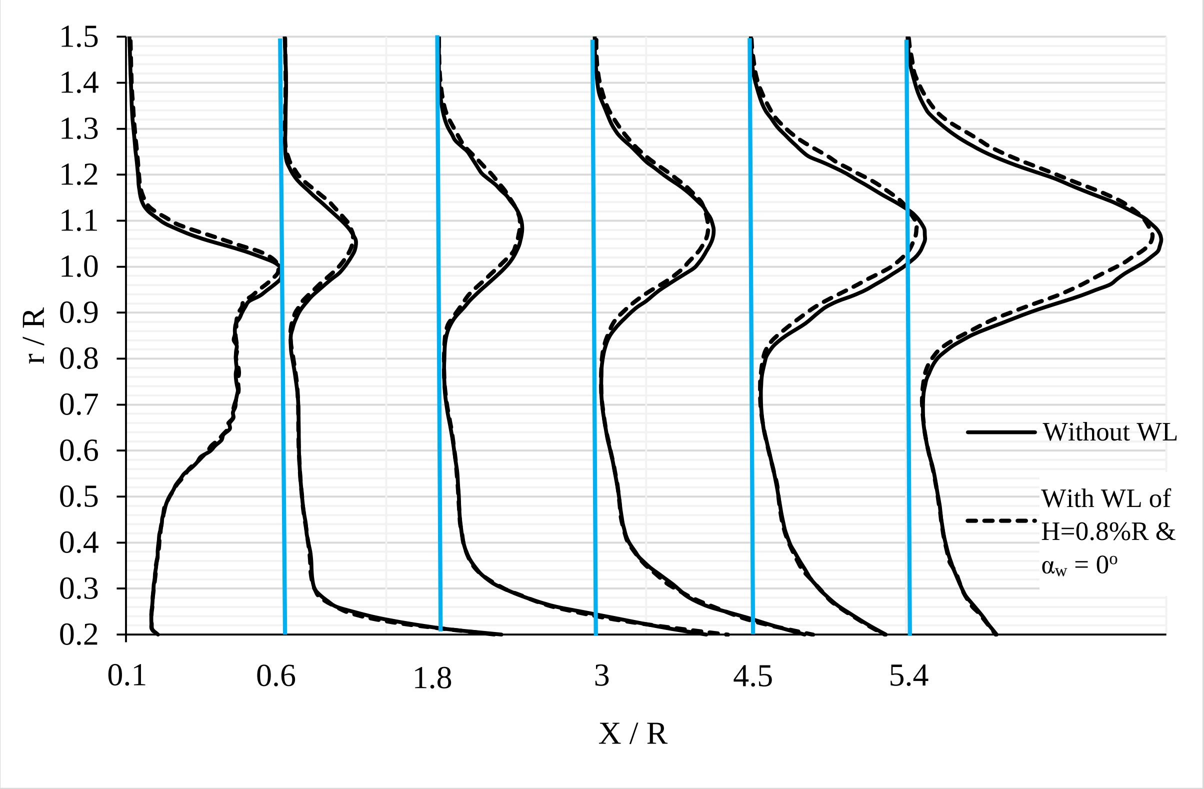

Figure 6.33: Reynolds shear stress profiles for the rotor without WL and with WL of H=0.8%R and α_w= 0º at λ=7

Figure 6.34 shows the influence of the WL of α_w= +20° on the shear stress profiles. It shows a noticeable increase in Reynolds shear stress peak near the rotor. The increase in shear is maintained in the upper part of the mixing region while the lower part shows an opposite decrease in the shear stress.

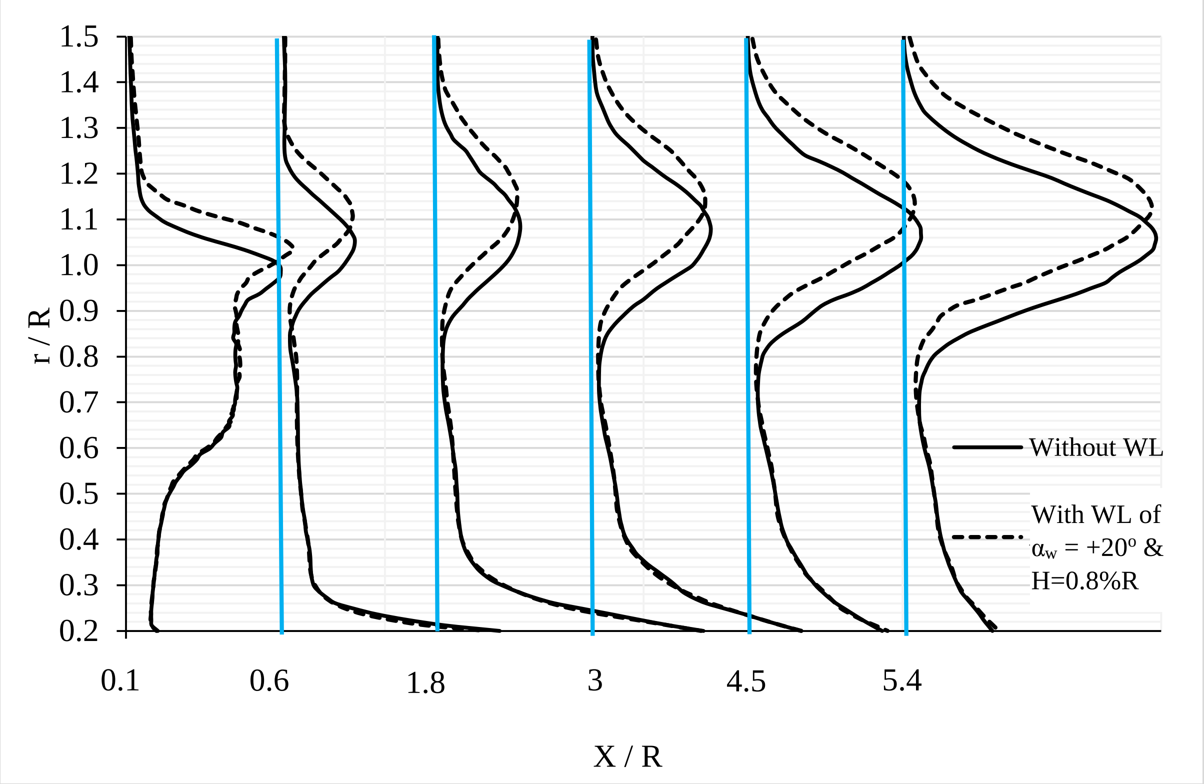

Figure 6.34: Reynolds shear stress profiles for the rotor without WL and with WL of α_w= +20° and H=0.8%R at λ=7

The WL of α_w= -30° shows the same Reynolds shear stress profiles by comparison to the rotor without WL as shown by Figure 6.35. Although it doesn't affect the near shear profiles, it reduces the shear in the lower part of the mixing region between the positions of X/R= 4.5 and X/R=5.4. It shows the same effect of the WL of H=0.8%R

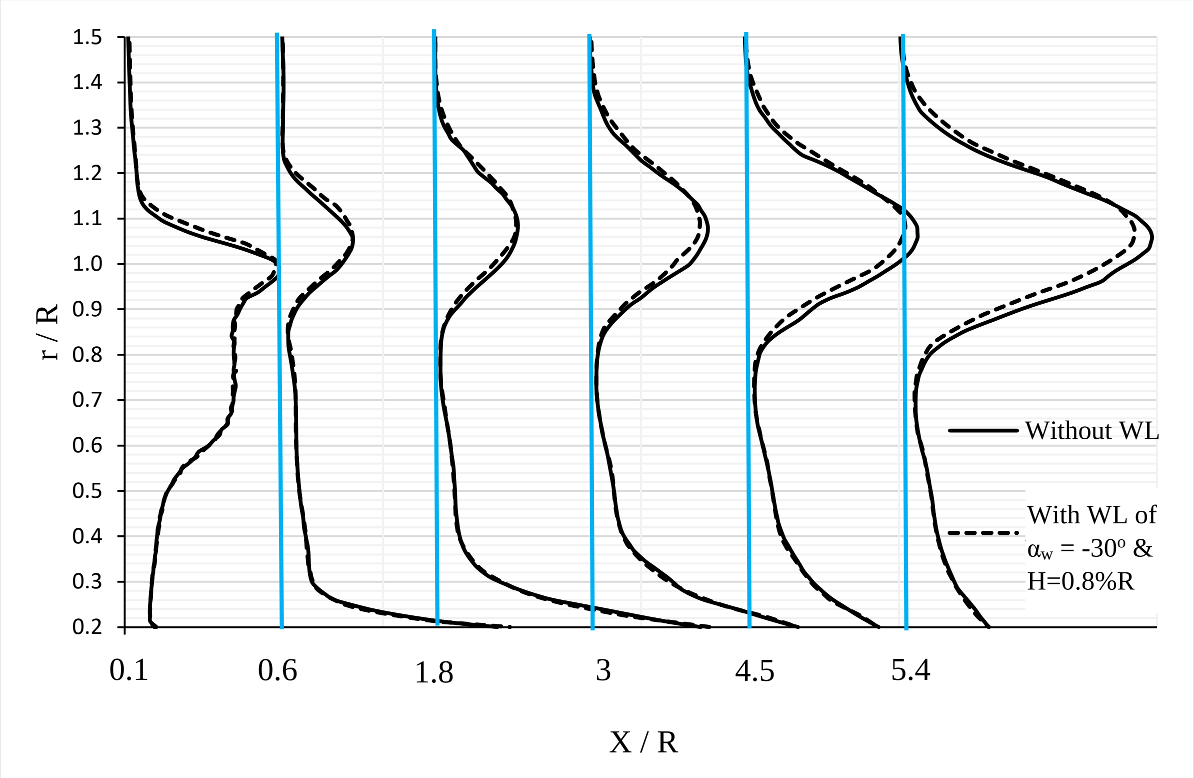

Figure 6.35: Reynolds shear stress profiles for the rotor without WL and with WL of α_w= -30° and H=0.8%R at λ=7

The maximum shear decreases by downstream distance up to distance 1.8 R and starts to increase again up to the studied distance. The mentioned observation is noticed for all cases. The section at X/R= 1.8 is considered the limit of the near wake of the present study and the far wake starts from this position. The present observation of wake division is in a good agreement with the wake division that was discussed by Jha et al. [64] in Figure 6.36.

The previous figures of Reynolds shear stress profiles downstream the rotor showed the effect of different WLs on the mixing region and near the rotor tip. The WL of α_w= +20° is proven to be the best WL used in the study since, it increases the width of mixing region and shear stress near the tip. The wake re-energizing process becomes easier by using it.

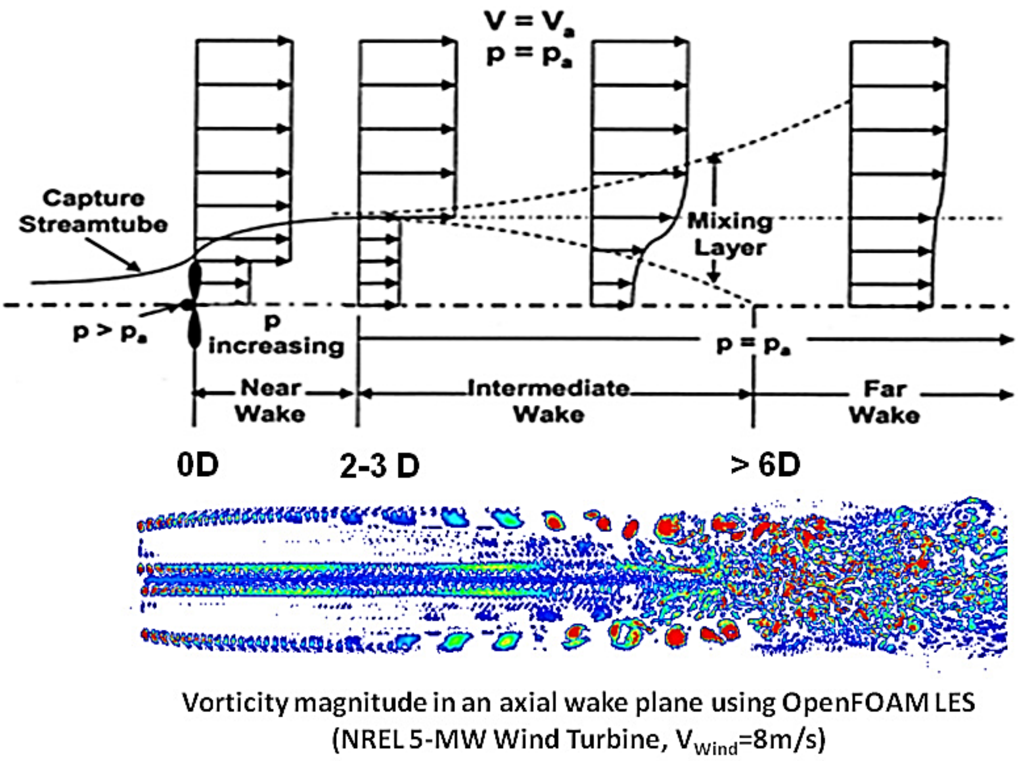

Figure 6.36: Wake regions divisions as discussed by Jha et al. [64]

6.4.3 Effect of WLs on tip vortices and wake expansion

For a more detailed discussion, tip vortices characteristics and wake expansion are discussed in the present section. The wake region is divided to three regions to study the tip vortices. The first region focuses on the tip vortex at azimuth angle 0^o which is just trailed from the tip trailing edge. The second region is the near wake by considering it ends by x/R = 2 as a result of the previous section. The third region is the far wake which is studied up to x/R =5.4.

Figure 6.37 shows the effect of adding the WL of H=8%R on the chord-wise vortex vorticity at azimuth angle 0^o. The vortex core is presented with the dark blue contours. The figure shows that the WL of H=8% R moves the vortex core by a distance equal to the WL height and reduces its vorticity by about 13% by comparison to the rotor without WL.

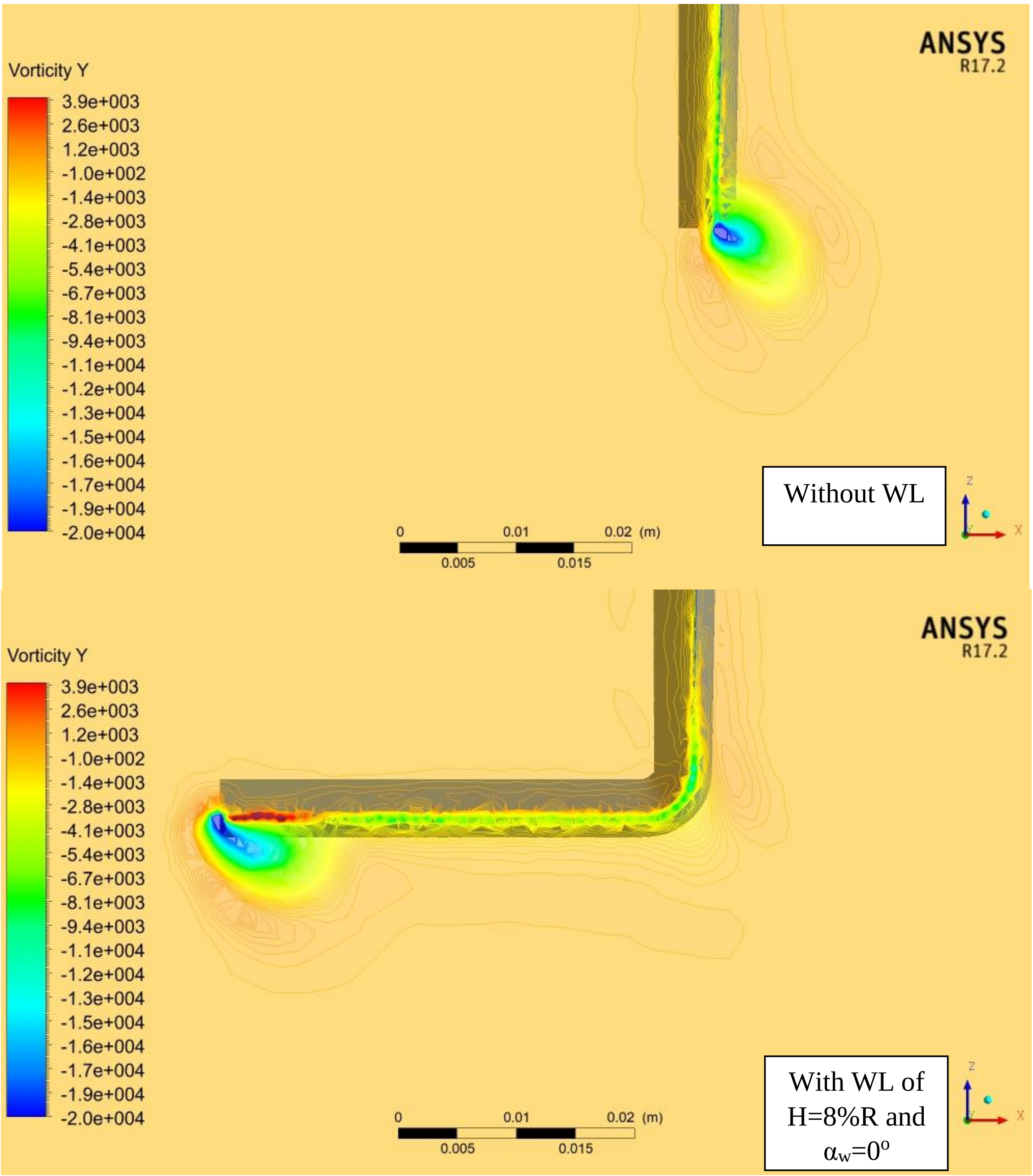

Figure 6.37: WL of H=8%R and α_w=0° effect on the chord-wise vorticity of the trailing vortex at azimuth angle =0° and λ=7

Figure 6.38 shows the trailed vortex core from the trailing edge which is represented by isosurface tool. The winglet is normal to the page and its effect isn't noticeable on the vortex intensity. It takes the vortex core away from the blade tip and makes it concentrate at the WL tip.

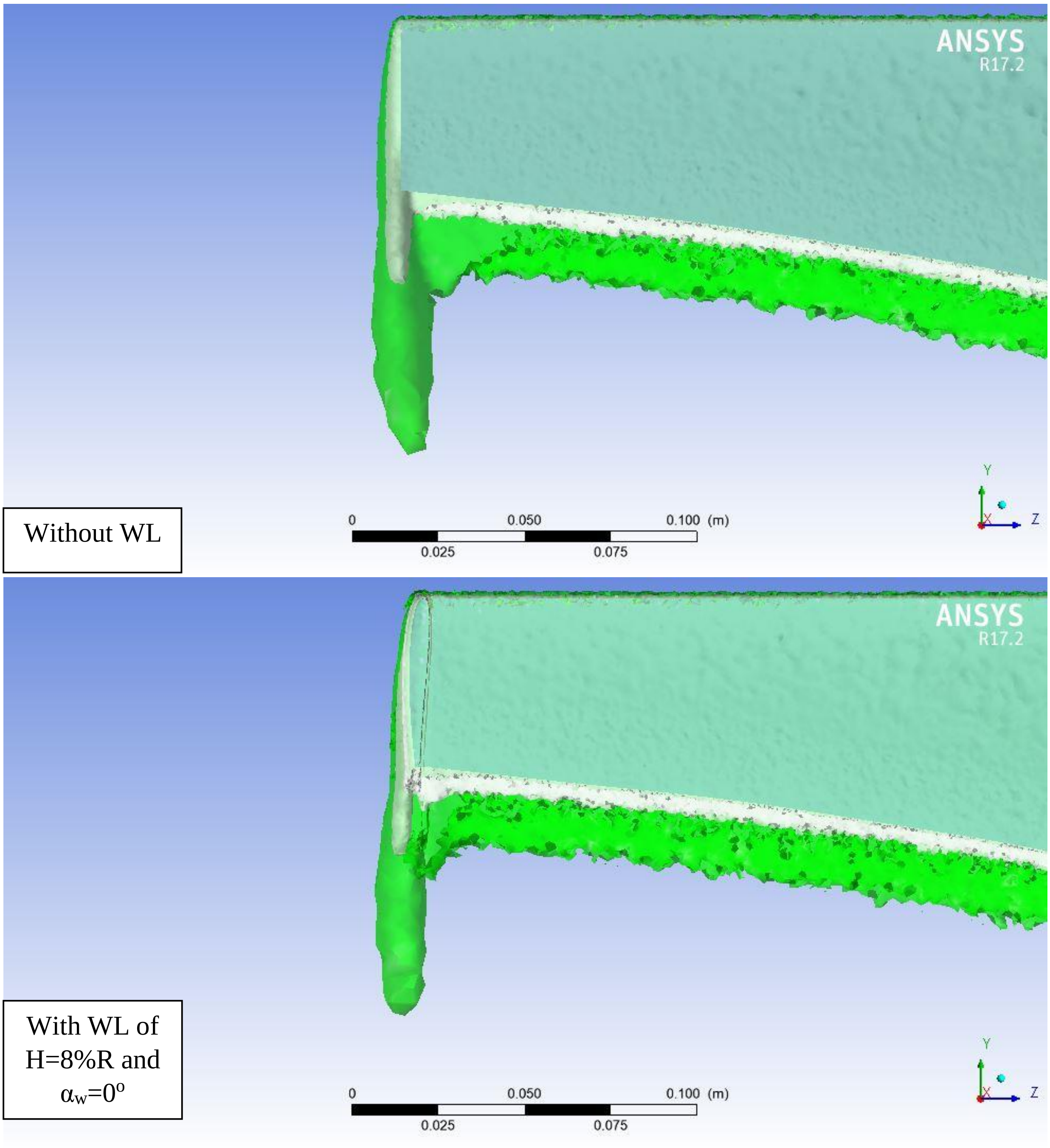

Figure 6.38: WL of H=8% R and $\alpha_w=0^o$ effect on the vortex core of the trailing vortex at $\lambda=7$ (White vortices: 4000 s^{-1}, Green vortices: 1000 s^{-1})

The WL of H=0.8%R performs the same job of the WL of H=8%R by taking the tip vortex core away from the blade tip as shown in Figure 6.39. It reduces the chord-wise vorticity by the same percent of the longer WL while it reduces the bound vortex effect by minimizing its height.

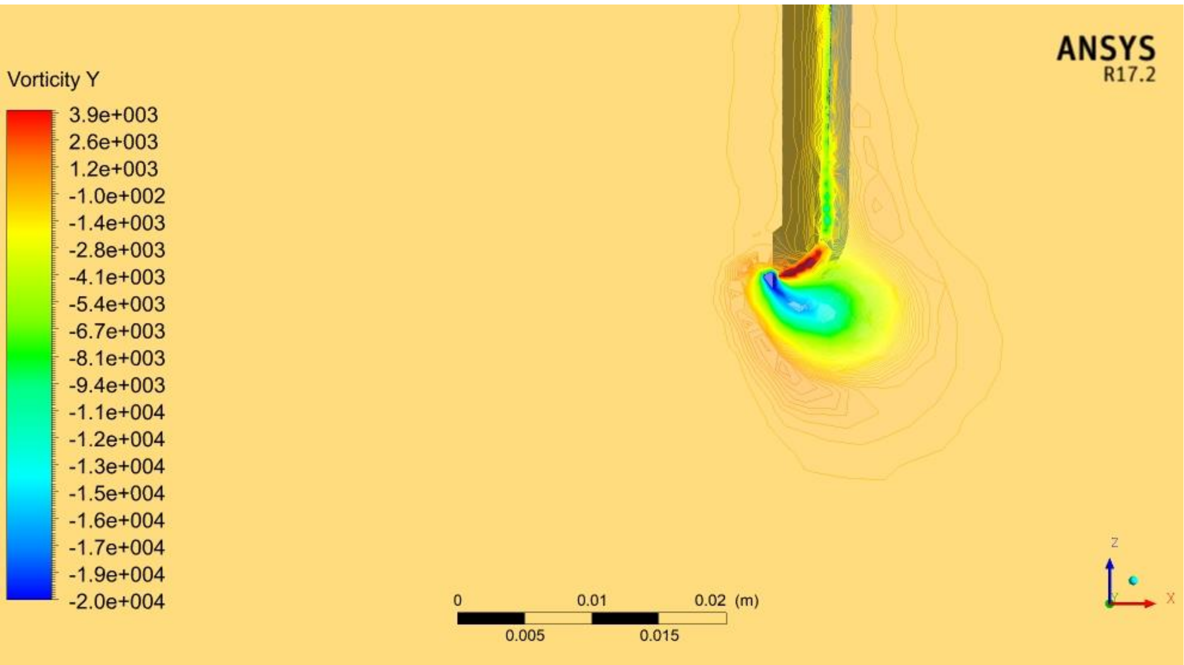

Figure 6.39: WL of H=0.8% R and $\alpha_w=0^o$ effect on the chord-wise vorticity of the trailing vortex at azimuth angle =0^o and $\lambda=7$

Figure 6.40 shows that the WL of H=0.8% R reduces the volume that is occupied by the vortex core along the blade tip chord. The same effect is previously demonstrated by the WL of H=8% R.

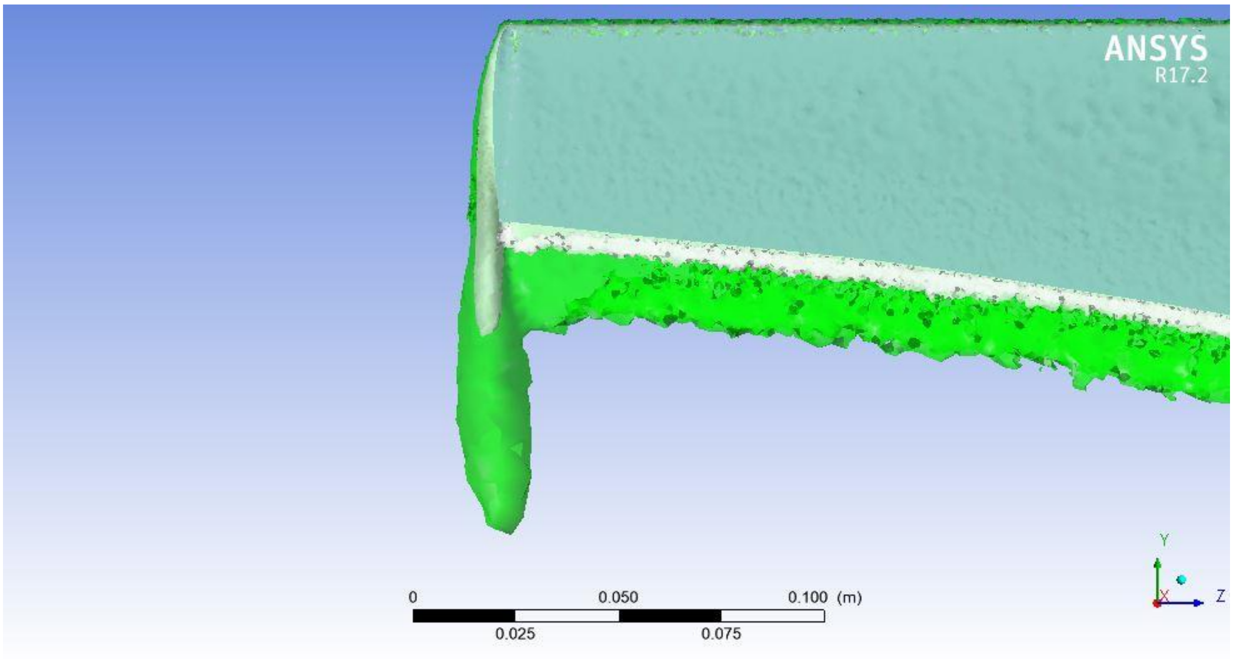

Figure 6.40: WL of H=0.8% R and $\alpha_w=0^o$ effect on the vortex core of the trailing vortex at $\lambda=7$ (White vortices: 4000 s^{-1}, Green vortices: 1000 s^{-1})

Figure 6.41 shows the effect of the WL of $\alpha_w=+20^o$ on the tip vortex diversion. Since it separate the tip vortex from the blade bound vortex and makes the vortex concentration far away from the blade tip. The chord-wise vorticity decreases by about 9% by comparison to the rotor without WL. Although it decreases the chord-wise vorticity component which is adjacent to the trailing edge, it increases the total vorticity of the trailed vortex. Figure 6.42 shows the trailed vortex separation from the WL leading edge. The early separation is occurred due to the tangential flow stall which forms a vortex with bigger size by comparison to the one of the blade without WL. The vortex is formed in the wake and far from the blade which enhances the near wake characteristics as will be discussed in the following section.

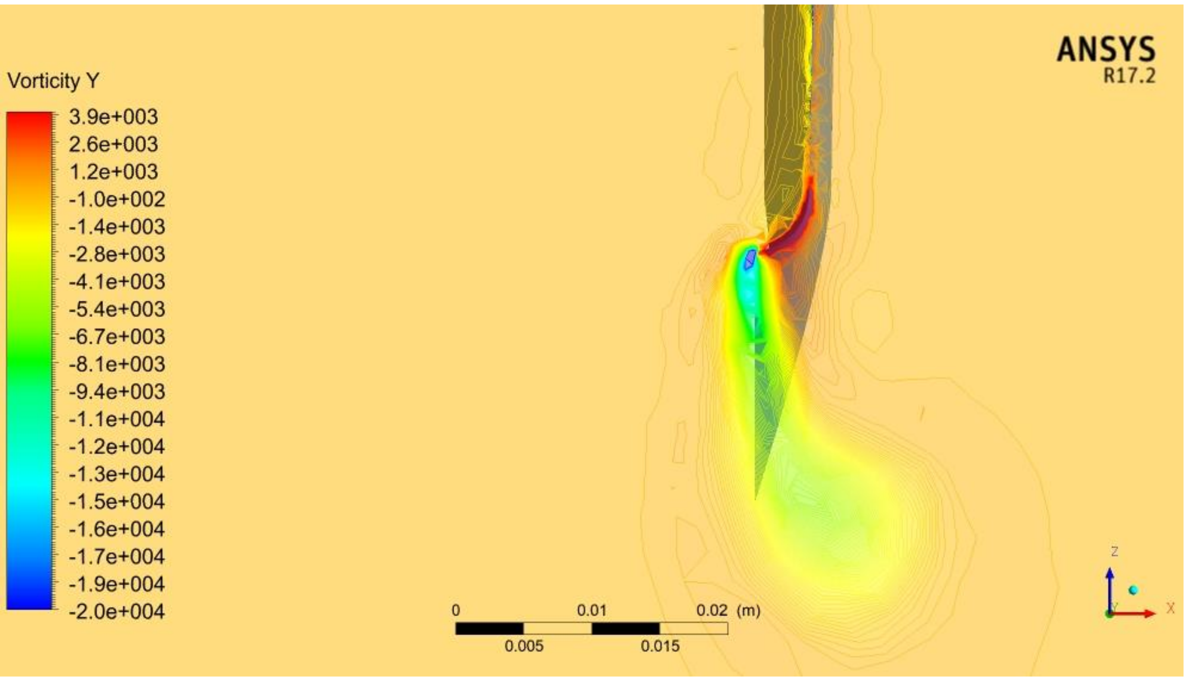

Figure 6.41: WL of α_w=+20º and H=0.8%R effect on the chord-wise vorticity of the trailing vortex at azimuth angle =0º and λ=7

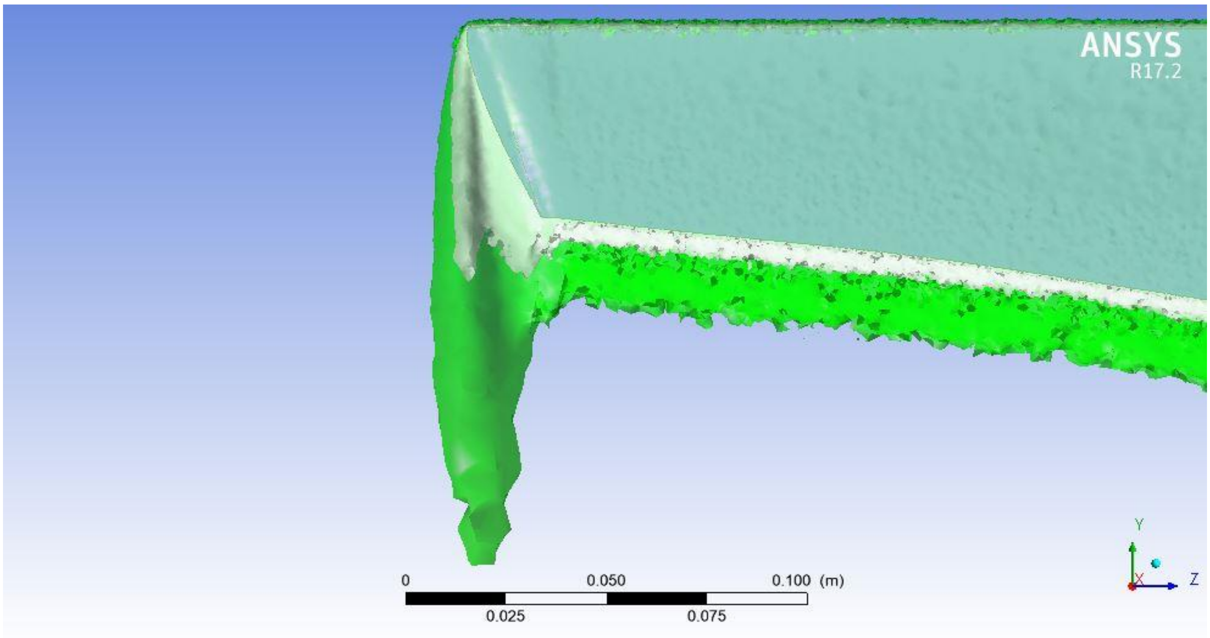

Figure 6.42: WL of α_w=+20º and H=0.8%R effect on the vortex core of the trailing vortex at λ=7 (White vortices: 4000 s^{-1}, Green vortices: 1000 s^{-1})

Figure 6.43 shows the effect of the WL of α_w=-30^o on the chord-wise vorticity component. Although it reduces the chord-wise component by about 25%, it makes the vortex core wider and expands along the trailing edge curvature. Figure 6.44 shows that the downwind WL helps the tip vortex core to concentrate at the tip of the blade. Since, the figure shows that the vortex core is shifted radially towards the direction of radius decrease.

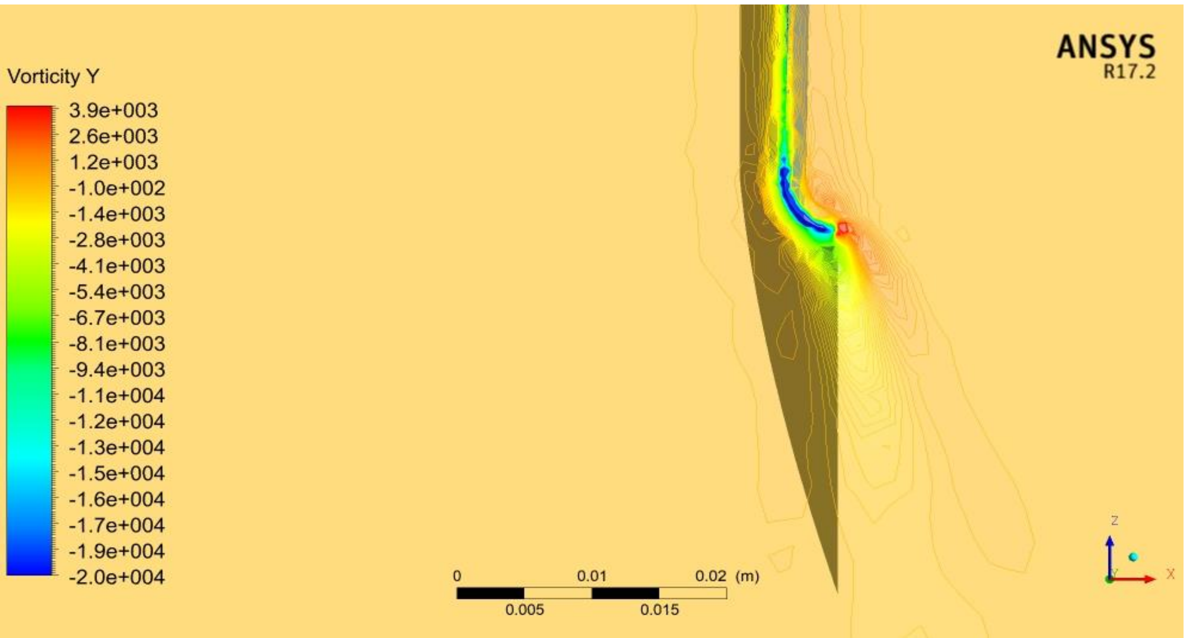

Figure 6.43: WL of α_w=-30^o and H=0.8%R effect on the chord-wise vorticity of the trailing vortex at azimuth angle =0^o and λ=7

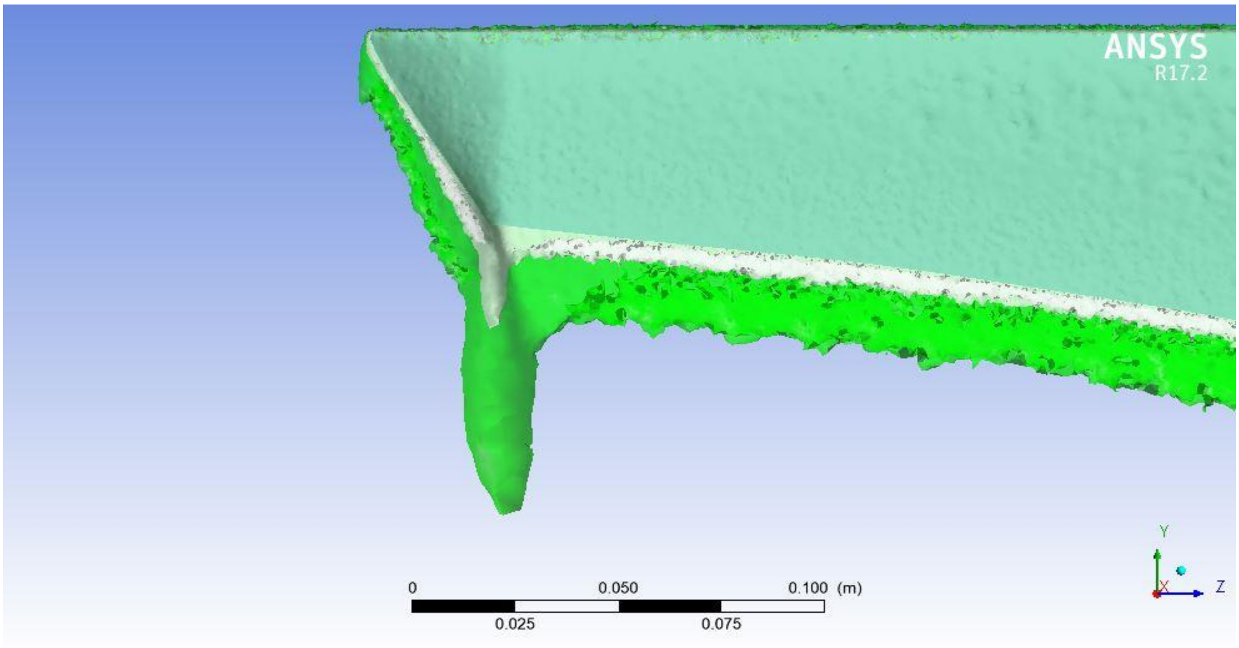

Figure 6.44: WL of α_w=-30^o and H=0.8%R effect on the vortex core of the trailing vortex at λ=7 (White vortices: 4000 s^{-1}, Green vortices: 1000 s^{-1})

The total vorticity values for different phases of the tip vortex helical path gives more informations about the wake characteristics. The helical path is obvious and can be presented with different vortices that are intersected with stream-wise plane up to vortex phase of 360°. Figure 6.45 shows the helical path in case of λ=7 for the rotor without WL and demonstrates the tip vortices merging after the azimuth angle of 360°.

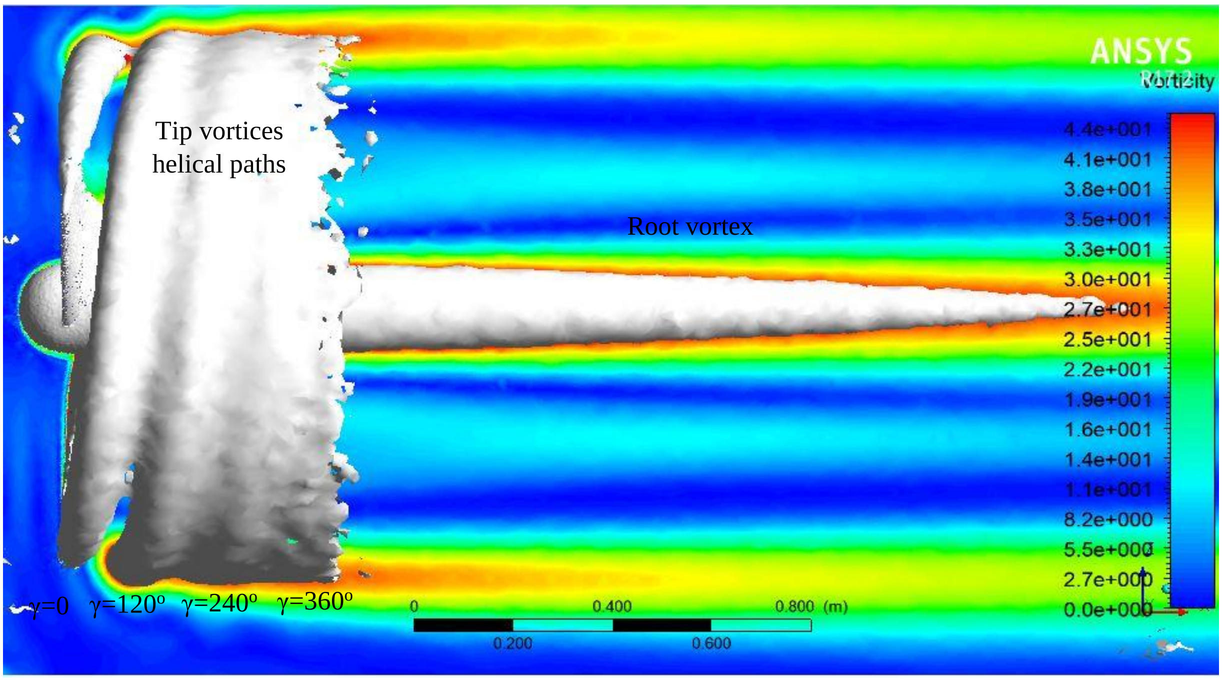

Figure 6.45: Tip vortices helical path up to vorticity value of 42 s^{-1} at λ=7 for the rotor without WL

Figure 6.46 shows the effect of the WL of H=8% R on the tip vortex age by vorticity values. Vorticity is normalized with respect to the chord length and free-stream velocity by $\frac{\omega\, c}{U_\infty}$. The WL increases the tip vortex vorticity at azimuth angle of 120° by about 4% by comparison to the rotor without WL. It shifts the vortices cores towards upstream due to its upwind extension. The increase in vorticity near the rotor for earlier vortex ages explains the reduction in Reynolds shear stress that was observed near the rotor in Figure 6.32. The tip vortex loses its strength by the downstream distance after azimuth angle 360° due to the higher stream-wise velocity deficits as shown before in Figure 6.27. Since the tip vortex rotation direction is clock-wise, the lower velocities in wake region and the higher velocities in free-stream make the vortices vorticity decreases as shown in Figure 6.47.

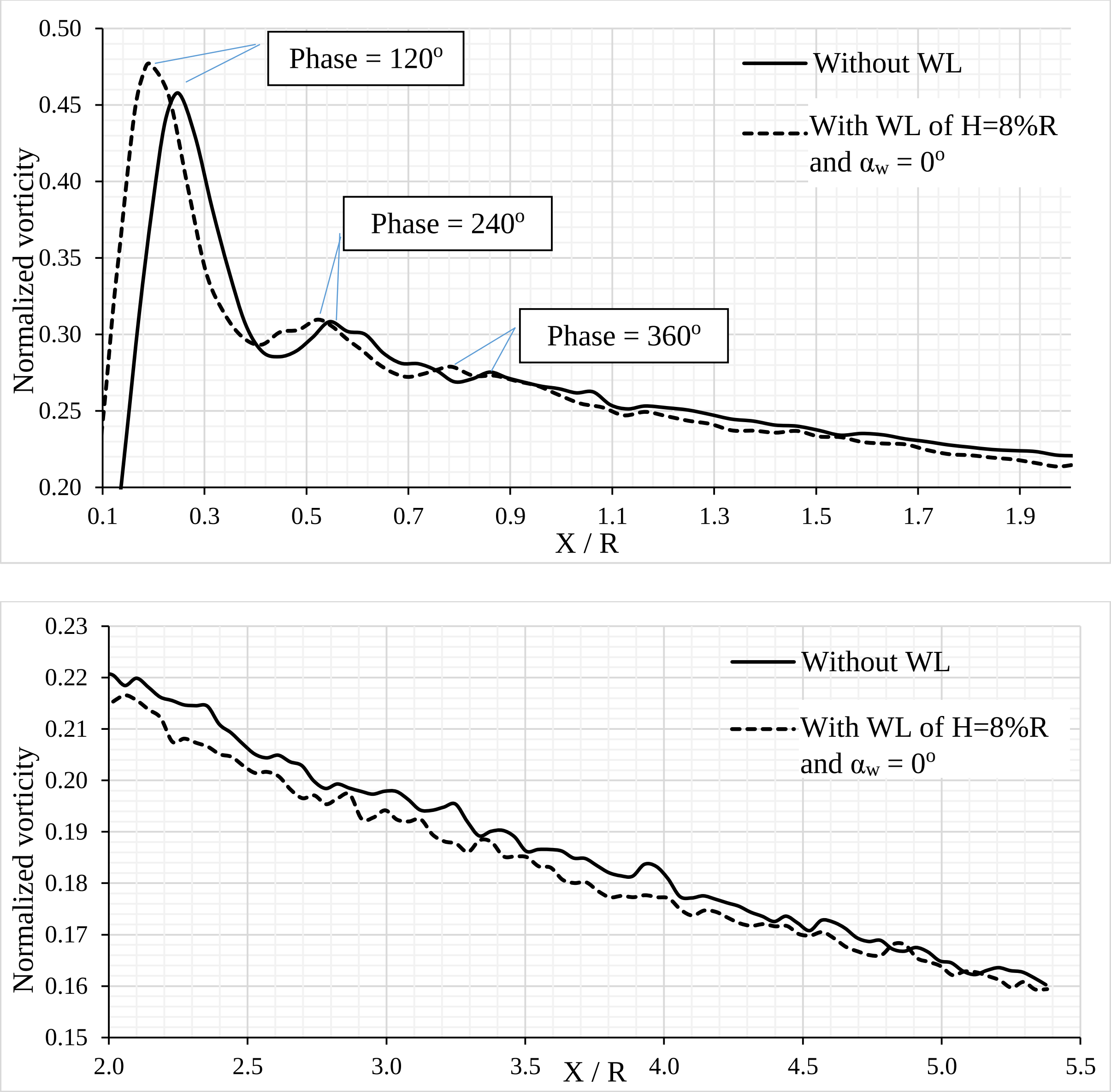

Figure 6.46: Effect of WL of H=8% R and α_w = 0º on tip vortex vorticity at λ=7

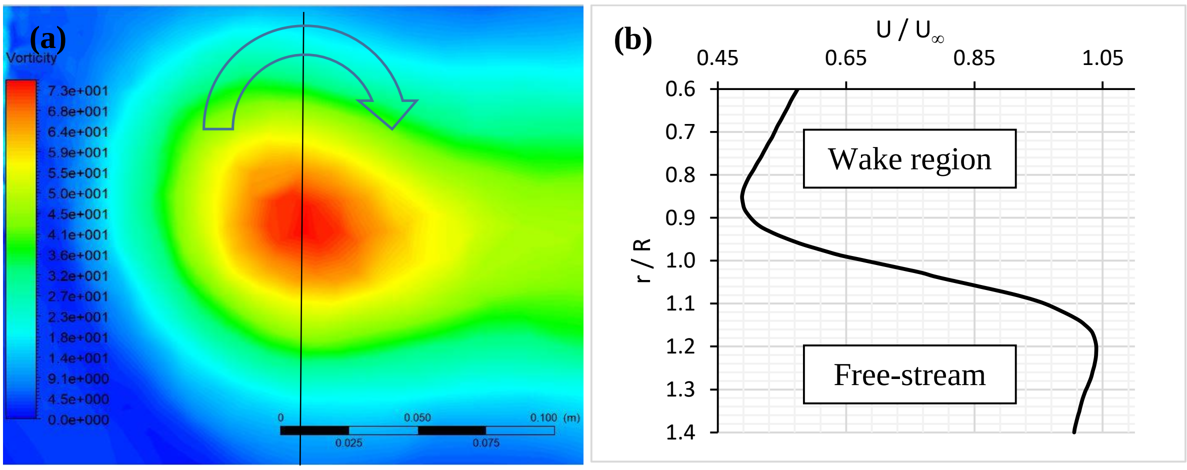

Figure 6.47: (a) Clock-wise tip vortex at azimuth angle = 120º and λ=7, (b) Axial velocity profile across the vortex

Figure 6.48 shows that the WL of H=0.8% R doesn't affect the vorticity of the near wake vortices. Since the trailed vortex is a result of the winglet tip only while in case of longer WL the trailed vortex is a result of the winglet tip and the winglet length bound vortex. Therefore the tip vortex that is produced by WL of H=0.8% has the same vorticity value of the tip without WL. The vortex phases after X/R=2 shows lower vorticity by comparison to the tip without WL. The decrease is occurred due to the little increase in thrust and velocity deficits as shown by Figure 6.28.

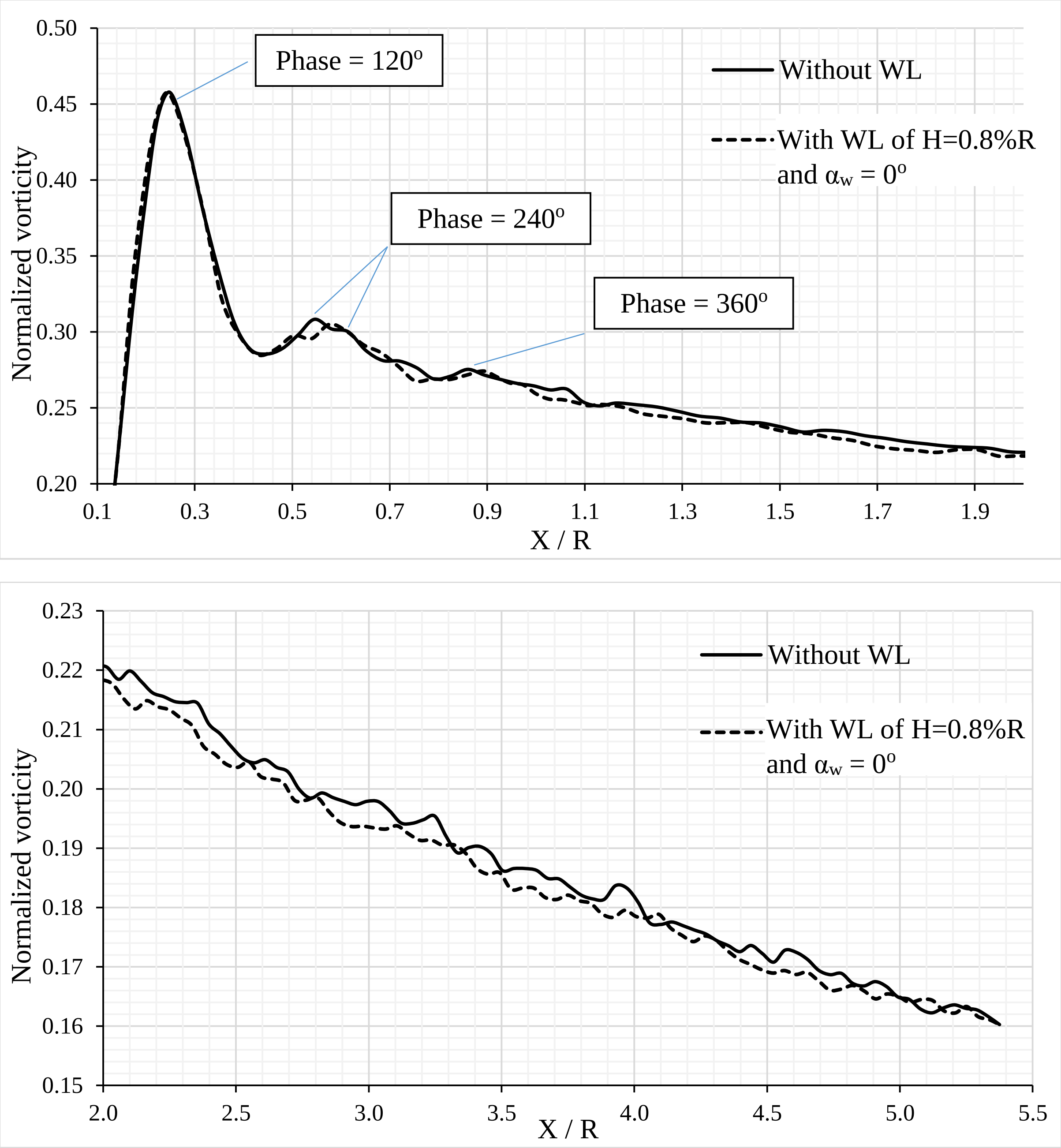

Figure 6.48: Effect of WL of H=0.8% R and α_w = 0° on tip vortex vorticity at λ=7

Although the WL of $\alpha_w = +20^o$ reduces the chord-wise vorticity as discussed before, it increases the trailed vortex due to the high angle of attack. It increases the vorticity of the trailed tip vortex at age 120^o by about 4%. The vortex of azimuth angle 120^o is located at X/R=0.2 position which showed a little lower Reynolds shear stress by comparison to the rotor without WL. The increase in vorticity value is suitable to the little decrease in Reynolds shear stress that was occurred at the same downstream position. Figure 6.49 shows a decrease in tip vortices vorticity downstream the position of X/R=2 due to the higher velocity deficits as discussed before.

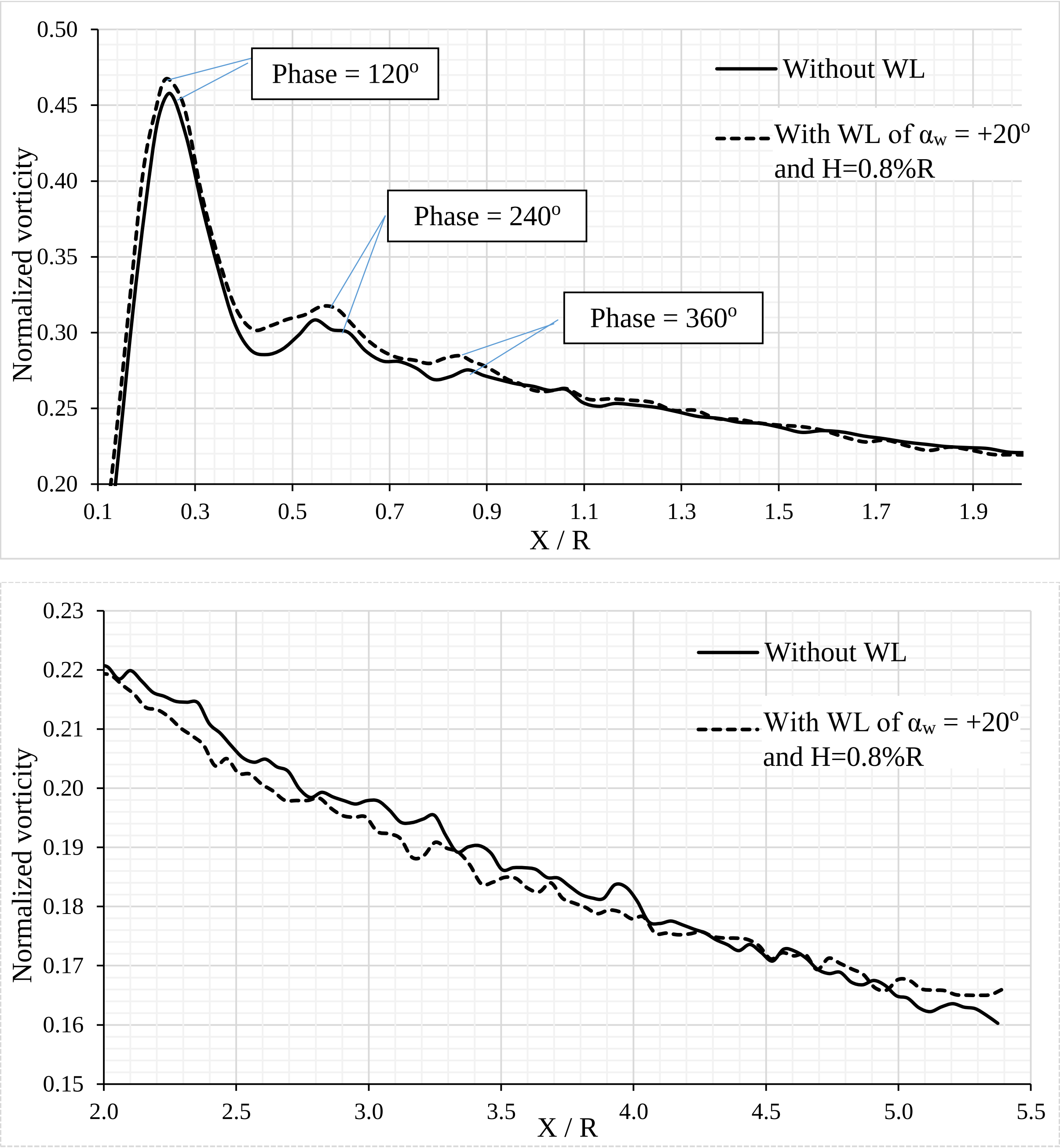

Figure 6.49: Effect of WL of $\alpha_w = +20^o$ and H=0.8%R on tip vortex vorticity at λ=7

Figure 6.50 shows the effect of the WL of α_w = -30° on the tip vortices vorticity. It shows a little decrease in the vorticity value by comparison to the case of blade without WL. Although it decreases the tip vortices vorticity, it makes the trailed vortex adjacent to the blade tip which adversely affects to the generated power.

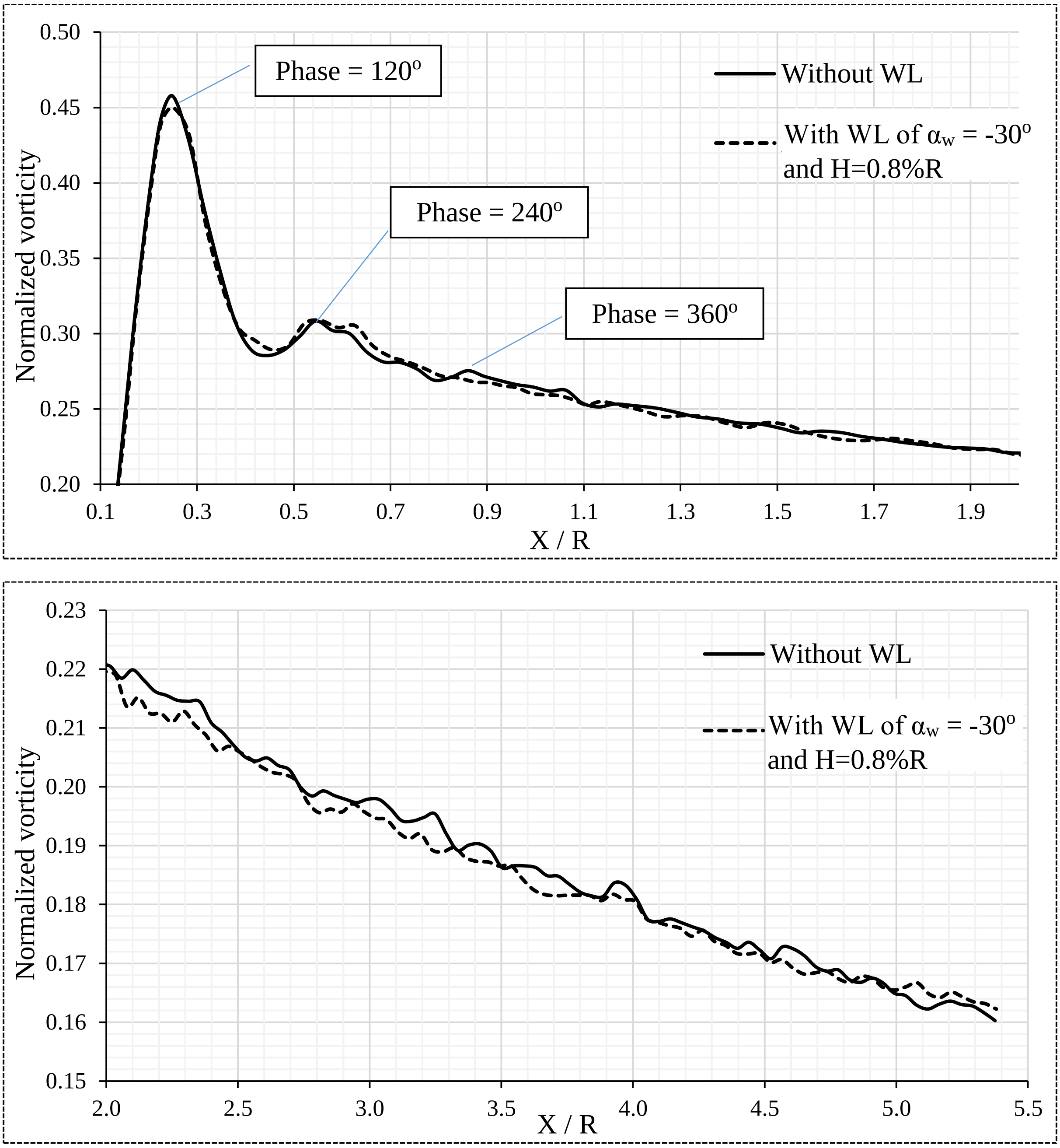

Figure 6.50: Effect of WL of α_w = -30° and H=0.8%R on tip vortex vorticity at λ=7

6.5 Experimental results

Experiments are performed on a model with the same geometry and dimensions of the simulated model to verify the effect of adding WL on the rotor performance. The generated wind from the wind tunnel is adjusted to be the same wind speed that was used in the numerical simulations (U=8m/s). The use of variable resistance gives the ability to change the electrical load of the circuit and thus changes the rotational speed of the rotor. The readings of rotational speed, electrical current and voltage are measured with appropriate devices as mentioned in Chapter 5. The generated electrical power is calculated for each rotational speed by multiplying the electrical voltage (V) by the electrical current (I). By taken into consideration that the generator efficiency is around 45% as calculated based on the manufacturer data (Chapter 5)

$$P_{elec.} = I \times V \quad \text{Watt} \tag{6.4}$$

Since, $P_{elec.}$: Electrical power in Watts

I : Electrical current in Amperes

V : Electrical voltages in voltages

The experiments are performed for the rotor without WL and four cases of the rotor with different WLs configurations. Two WLs of heights H=8%R and H=0.8%R at $\alpha_w=0^o$ are studied to verify that the rotor power is better for smaller height WL. The others are of $\alpha_w=+20^o$ and $\alpha_w=-30^o$ with H kept constant at 0.8%R. The cases are selected based on the numerical simulations results. Since, the WL of $\alpha_w=+20^o$ is the optimum WL in the study while the WL of $\alpha_w=-30^o$ has the worst effect on the rotor performance.

The readings for rotational speed, electrical current and voltage are recorded for each electrical load in case of the rotor without WL as follows (Table 6.1).

Table 6.1: Readings at different electrical loads in case of rotor without WL

Cases	R (Ω)	N (r.p.m)	I (A)	V (V)	Power (W)
1	0.22	80	0.58	0.5	0.29
2	0.44	88.4	0.59	0.8	0.472
3	0.66	97.5	0.61	1	0.61
4	0.88	157	0.78	2.3	1.794
5	1.1	670	3.14	9.5	29.83
6	1.32	746	3.19	11.2	35.728
7	1.54	762	3.05	12.8	39.04
8	1.76	786	2.93	13.5	39.555
9	1.98	831	2.77	14.7	40.719
10	2.2	854	2.75	15	41.25
11	2.42	865	2.7	16.1	43.47
12	2.64	895	2.61	17.1	44.631
13	2.86	910	2.54	17.5	44.45
14	3.08	918	2.48	18.8	46.624
15	3.3	932	2.44	19.5	47.58
16	3.52	950	2.37	20.4	48.348
17	3.74	953	2.3	20.5	47.15
18	3.96	960	2.26	21.6	48.816
19	4.18	981	2.27	21.9	49.713
20	4.4	1000	2.15	22.5	48.375
21	4.62	977	2.13	23	48.99
22	4.84	1018	2.08	23.6	49.088
23	5.06	1026	2.02	24	48.48
24	5.28	1047	2	24.6	49.2
25	5.5	1056	1.95	25	48.75
26	5.72	1050	1.88	25.2	47.376
27	5.94	1054	1.86	25.7	47.802
28	6.16	1081	1.85	26.3	48.655
29	6.38	1095	1.77	26	46.02
30	6.6	1093	1.74	26.5	46.11
31	6.82	1083	1.73	26.8	46.364
32	7.04	1095	1.69	27	45.63
33	8.04	1120	1.61	28.2	45.402
34	9.04	1136	1.53	29.4	44.982
35	10.04	1148	1.45	29.8	43.21
36	14.04	1183	1.26	31.5	39.69

6.5.1 Experimental effect of the WL with H=8%R and α_w =0º on the rotor performance

The readings for rotational speed, electrical current and voltage are recorded for each electrical load in case of adding the WL of H=8% R to the rotor as follows (Table 6.2).

Table 6.2: Readings at different electrical loads in case of rotor with WL of H=8% R and α_w =0º

Cases	R (Ω)	N (r.p.m)	I (A)	V (V)	Power (W)
1	0.22	74	0.54	0.4	0.216
2	0.44	83	0.57	0.7	0.399
3	0.66	92	0.57	1.1	0.627
4	0.88	114	0.62	1.6	0.992
5	1.1	136	0.68	2.1	1.428
6	1.32	185	0.79	2.8	2.212
7	1.54	795	3.14	13.2	41.448
8	1.76	814	2.98	14	41.72
9	1.98	840	2.9	14.9	43.21
10	2.2	870	2.84	16	45.44
11	2.42	907	2.73	17	46.41
12	2.64	903	2.64	17.4	45.936
13	2.86	916	2.55	18.1	46.155
14	3.08	927	2.46	18.8	46.248
15	3.3	947	2.4	19.5	46.8
16	3.52	956	2.33	20.3	47.299
17	3.74	982	2.28	20.6	46.968
18	3.96	995	2.23	21.2	47.276
19	4.18	1000	2.16	21.8	47.088
20	4.4	1010	2.11	22.5	47.475
21	4.62	1023	2.06	22.8	46.968
22	4.84	1025	2.04	23.3	47.532
23	5.06	1036	1.99	23.9	47.561
24	5.28	1040	1.92	24.3	46.656
25	5.5	1055	1.91	25	47.75
26	5.72	1062	1.87	25.2	47.124
27	5.94	1067	1.81	25.5	46.155
28	6.16	1072	1.81	25.9	46.879
29	6.38	1080	1.74	26	45.24
30	6.6	1100	1.72	26.9	46.268
31	6.82	1100	1.67	26.8	44.756
32	7.04	1111	1.67	27.8	46.426
33	8.04	1127	1.56	28.3	44.148

34	9.04	1135	1.47	29.5	43.365
35	10.04	1145	1.38	30.3	41.814
36	14.04	1200	1.22	32.1	39.162

The generated power by the DC generator are normalized with respect to the theoretical power of wind ($0.5\rho AV^3$) to get C_{pw}. Figure 6.51 shows that the WL of H= 8%R increases the C_{pw} up to λ=5.8 while starts to decrease it at higher tip speed ratios. The increase in WL height at higher tip speed ratios increases the drag on the blade tip and thus decreases C_{pw} as discussed before in numerical results. The experimental results are near and with agreement to those of the numerical study that are discussed before.

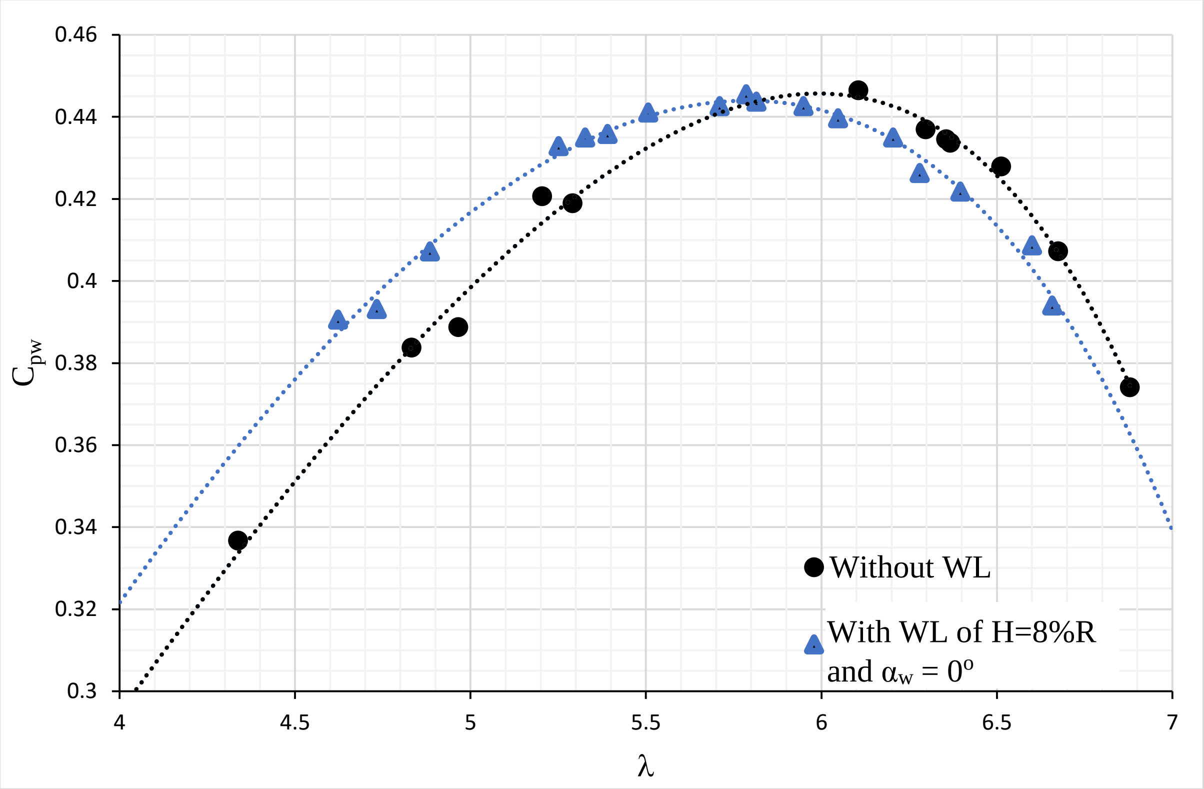

Figure 6.51: Experimental effect of the WL with H=8%R and α_w=0° on the rotor power coefficient

6.5.2 Experimental effect of the WL with H=0.8%R and α_w =0° on the rotor performance

The WL of H=0.8%R is the minimum height used in the study due to geometrical limitations as mentioned before. The readings for rotational speed, electrical current and voltage are recorded for each electrical load in case of adding the WL to the rotor as follows (Table 6.3).

Table 6.3: Readings at different electrical loads in case of rotor with WL of H=0.8% R and α_w=0°

Cases	R (Ω)	N (r.p.m)	I (A)	V (V)	Power (W)
1	0.22	69	0.55	0.4	0.22
2	0.44	78.5	0.56	0.8	0.448
3	0.66	99.4	0.6	1.3	0.78
4	0.88	138	0.7	2.1	1.47
5	1.1	155.7	0.76	2.6	1.976
6	1.32	740	3.18	11.8	37.524
7	1.54	783	3.05	13	39.65
8	1.76	796	2.91	13.9	40.449
9	1.98	840	2.85	14.9	42.465
10	2.2	850	2.76	15.5	42.78
11	2.42	865	2.68	16.5	44.22
12	2.64	900	2.58	17.6	45.408
13	2.86	909	2.48	18.3	45.384
14	3.08	935	2.41	19	45.79
15	3.3	955	2.34	19.6	45.864
16	3.52	965	2.26	20.5	46.33
17	3.74	1016	2.22	21.25	47.175
18	3.96	1030	2.23	21.9	48.837
19	4.18	1020	2.17	22.5	48.825
20	4.4	1038	2.1	22.7	47.67
21	4.62	1030	2.06	23.1	47.586
22	4.84	1040	2.02	23.8	48.076
23	5.06	1045	1.95	24	46.8
24	5.28	1063	1.92	24.5	47.04
25	5.5	1068	1.9	25.1	47.69
26	5.72	1072	1.86	25.4	47.244
27	5.94	1087	1.83	25.9	47.397
28	6.16	1085	1.79	26.1	46.719
29	6.38	1090	1.74	26.4	45.936
30	6.6	1118	1.75	27.2	47.6
31	6.82	1150	1.68	27.2	45.696

32	7.04	1111	1.64	27.5	45.1
33	8.04	1133	1.54	28.5	43.89
34	9.04	1156	1.46	29.8	43.508
35	10.04	1170	1.4	30.5	42.7
36	14.04	1200	1.21	32.3	39.083

Figure 6.52 shows that adding WL of H=0.8% increases C_{pw} for whole the range of λ. It improves C_{pw} by about 3% at $\lambda=6$. The present case confirms that the WL of suitable height to the generated tip vortex is able to push it away from the blade tip. There isn't need for longer WL heights since, longer heights increase drag as discussed before in the numerical results.

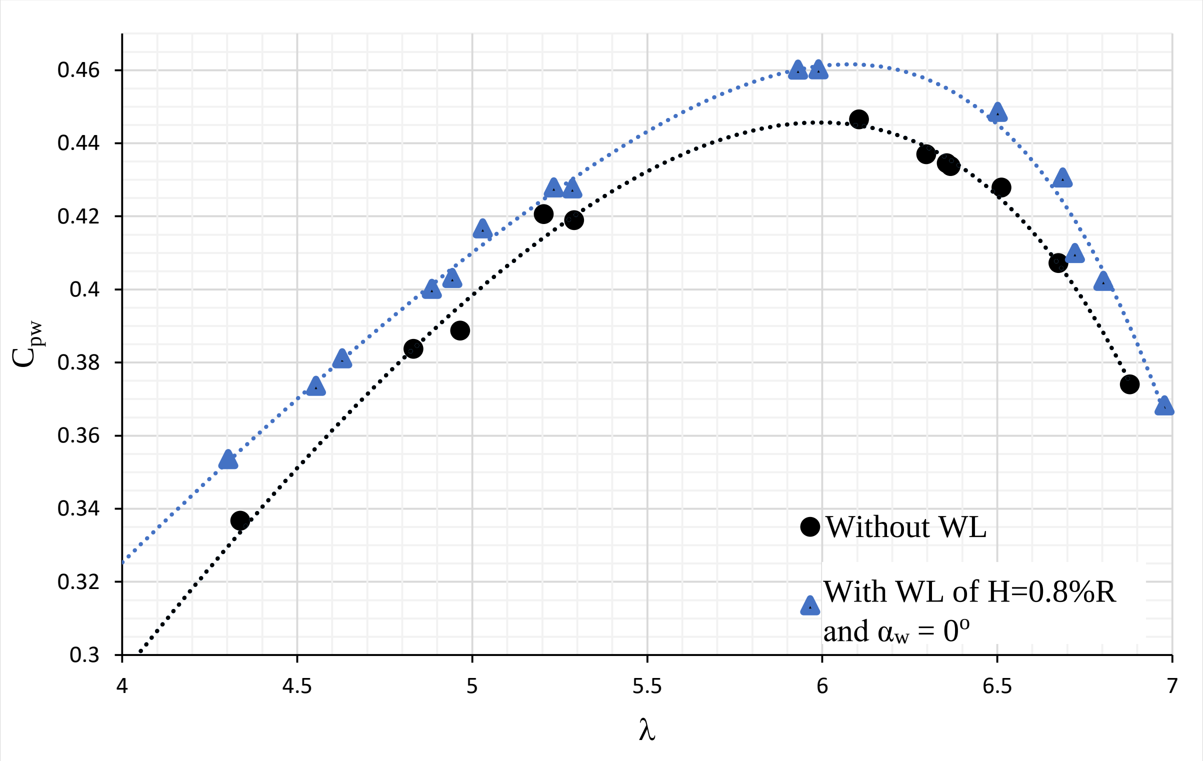

Figure 6.52: Experimental effect of the WL with H=0.8%R and α_w=0° on the rotor power coefficient

6.5.3 Experimental effect of the WL with α_w =+20º and H=0.8%R on the rotor performance

Experiments are carried out for the rotor with adding WL of α_w=+20º to the rotor while keeping H=0.8%R. The readings for rotational speed, electrical current and voltage are recorded for each electrical load in case of adding the WL to the rotor as follows (Table 6.4).

Table 6.4: Readings at different electrical loads in case of rotor with WL of α_w=+20º and H=0.8%R

Cases	R (Ω)	N (r.p.m)	I (A)	V (V)	Power (W)
1	0.22	72	0.58	0.5	0.29
2	0.44	91	0.62	1	0.62
3	0.66	135	0.65	1.4	0.91
4	0.88	131.5	0.72	1.9	1.368
5	1.1	246	1.16	4	4.64
6	1.32	743	3.34	11.5	38.41
7	1.54	770	3.22	12.5	40.25
8	1.76	812	3.15	13.9	43.785
9	1.98	840	3	15.1	45.3
10	2.2	878	2.91	15.9	46.269
11	2.42	898	2.82	17	47.94
12	2.64	902	2.74	18	49.32
13	2.86	908	2.65	18.5	49.025
14	3.08	947	2.59	19.5	50.505
15	3.3	960	2.56	19.8	50.688
16	3.52	992	2.48	20.5	50.84
17	3.74	990	2.39	21.1	50.429
18	3.96	998	2.31	21.6	49.896
19	4.18	1006	2.31	22.5	51.975
20	4.4	1018	2.22	23	51.06
21	4.62	1022	2.18	23.5	51.23
22	4.84	1032	2.16	24	51.84
23	5.06	1052	2.08	24.4	50.752
24	5.28	1065	2.06	24.6	50.676
25	5.5	1075	2.05	25.2	51.66
26	5.72	1060	1.98	25.5	50.49
27	5.94	1083	1.93	26.2	50.566
28	6.16	1085	1.88	26.1	49.068
29	6.38	1090	1.86	26.7	49.662
30	6.6	1095	1.82	27	49.14
31	6.82	1100	1.79	27.6	49.404
32	7.04	1112	1.75	28	49
33	8.04	1137	1.67	28.8	48.096

34	9.04	1150	1.56	29.7	46.332
35	10.04	1171	1.49	30.3	45.147
36	14.04	1200	1.3	32.4	42.12

Figure 6.53 confirms the results obtained numerically. Experimental power coefficient increased by 6.6% at λ=7 by using the WL of $\alpha_w = +20^o$. It is able to diverge the tip vortex from its origin of formation in addition to pushing it away from the blade tip.

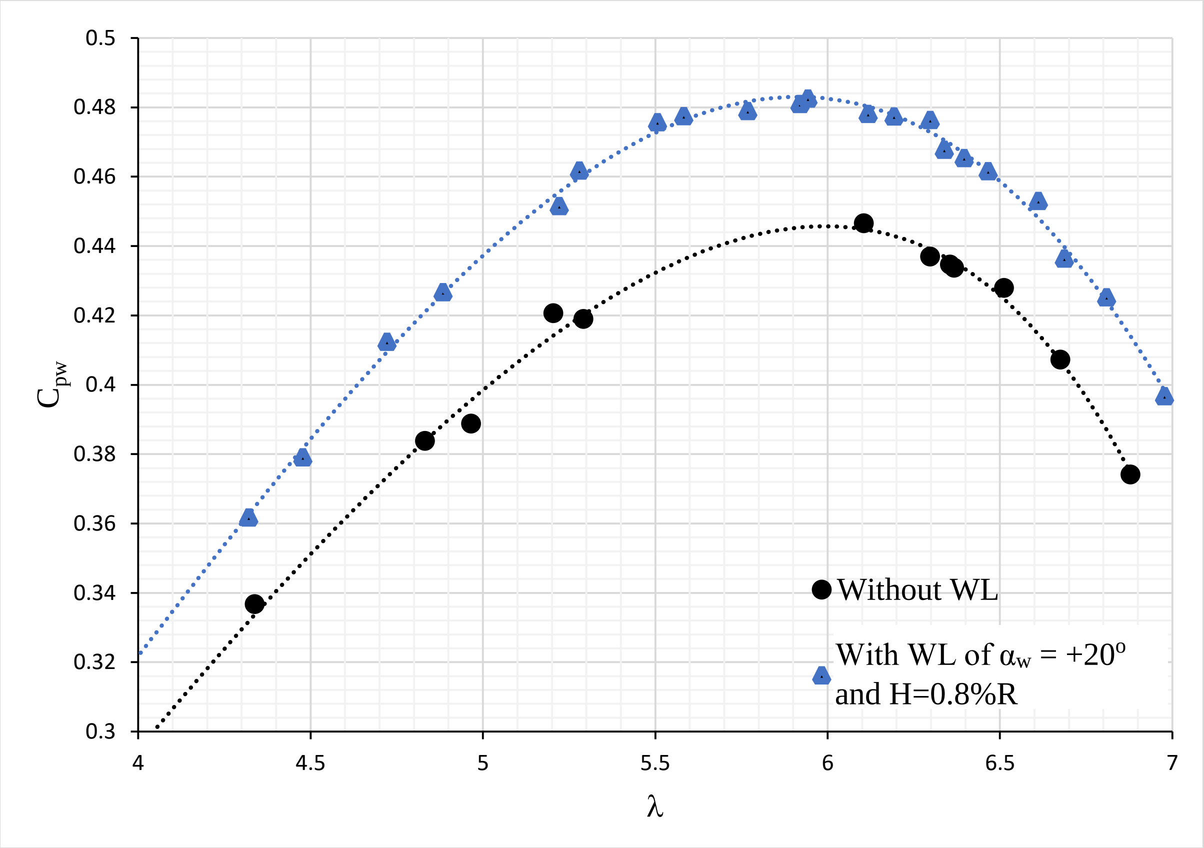

Figure 6.53: Experimental effect of the WL with α_w= +20° and H=0.8%R on the rotor power coefficient.

6.5.4 Experimental effect of the WL with α_w =-30^o and H=0.8%R on the rotor performance

Similar experiments are performed for the rotor by adding WL of α_w = -30^o. The readings for rotational speed, electrical current and voltage are recorded for each electrical load in case of adding the WL to the rotor as follows (Table 6.5).

Table 6.5: Readings at different electrical loads in case of rotor with WL of α_w= -30^o and H=0.8%R

Cases	R (Ω)	N (r.p.m)	I (A)	V (V)	Power (W)
1	0.22	76	0.59	0.5	0.295
2	0.44	87	0.61	0.8	0.488
3	0.66	94	0.6	1.1	0.66
4	0.88	129	0.72	1.9	1.368
5	1.1	146	0.76	2.4	1.824
6	1.32	178	0.88	2.8	2.464
7	1.54	767	3.16	12.8	40.448
8	1.76	790	3.03	13.6	41.208
9	1.98	821	2.88	14.4	41.472
10	2.2	850	2.81	15.5	43.555
11	2.42	872	2.71	16.5	44.715
12	2.64	890	2.62	17.2	45.064
13	2.86	895	2.53	17.8	45.034
14	3.08	915	2.48	18.5	45.88
15	3.3	928	2.41	19.3	46.513
16	3.52	945	2.32	19.9	46.168
17	3.74	960	2.3	20.5	47.15
18	3.96	970	2.25	21	47.25
19	4.18	984	2.19	21.2	46.428
20	4.4	990	2.18	22	47.96
21	4.62	998	2.09	22.3	46.607
22	4.84	1009	2.06	22.8	46.968
23	5.06	1011	2.02	23.2	46.864
24	5.28	1017	1.99	23.5	46.765
25	5.5	1021	1.91	23.8	45.458
26	5.72	1030	1.88	24.1	45.308
27	5.94	1050	1.84	24.5	45.08
28	6.16	1060	1.81	24.9	45.069
29	6.38	1050	1.77	25.2	44.604
30	6.6	1051	1.73	25.5	44.115
31	6.82	1058	1.71	26	44.46
32	7.04	1065	1.66	26.3	43.658

33	8.04	1088	1.56	27.3	42.588
34	9.04	1095	1.47	28	41.16
35	10.04	1110	1.41	28.9	40.749
36	14.04	1145	1.22	30.9	37.698

The results of C_{pw} also confirm the numerical findings for the same negative toe angle especially at higher tip speed ratios. Adding the WL of $\alpha_w = -30^o$ reduces the C_{pw} by about 10% at $\lambda=7$ as shown in Figure 6.54. At lower tip speed ratio range up to $\lambda=5.5$, the WL of $\alpha_w = -30^o$ shows a little improvement in C_{pw}.

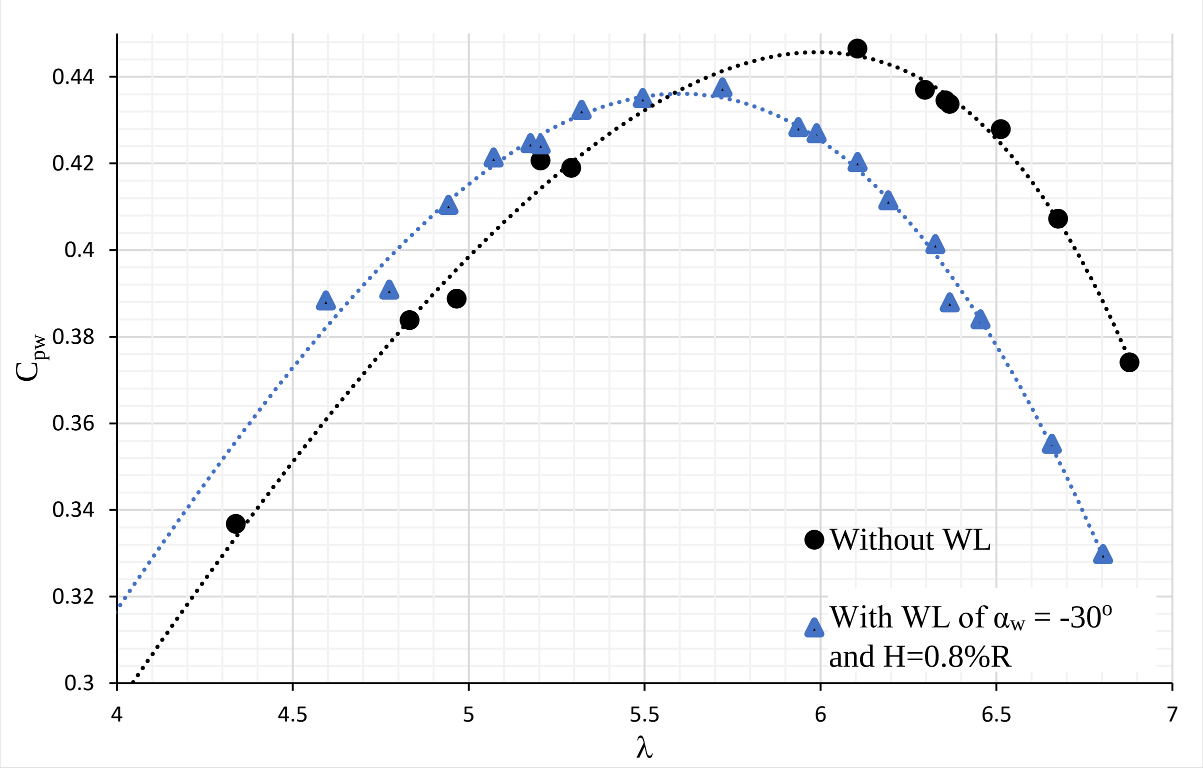

Figure 6.54: Experimental effect of the WL with $\alpha_w = -30^o$ and H=0.8%R on the rotor power coefficient

6.5.5 Comparison between numerical and experimental studies for WL of α_w=+20°

Although the present numerical model has been previously validated, the present experiments show that the experimental results confirm the numerical ones. Figure 6.55 shows the variations of power coefficient with tip speed ratios both experimentally and numerically. The numerical maximum power coefficient increases by about 6%. The discrepancy between the experimental values and numerical ones can be explained by the variation of upstream velocity created by the jet wind tunnel. Space limitations at the laboratory didn't allow enough jet length to reach uniform velocity profile upstream the turbine. Since the power is proportional to the wind speed raised to power three, the discrepancy of 6% in power can be produced by 1.8% of wind speed variation.

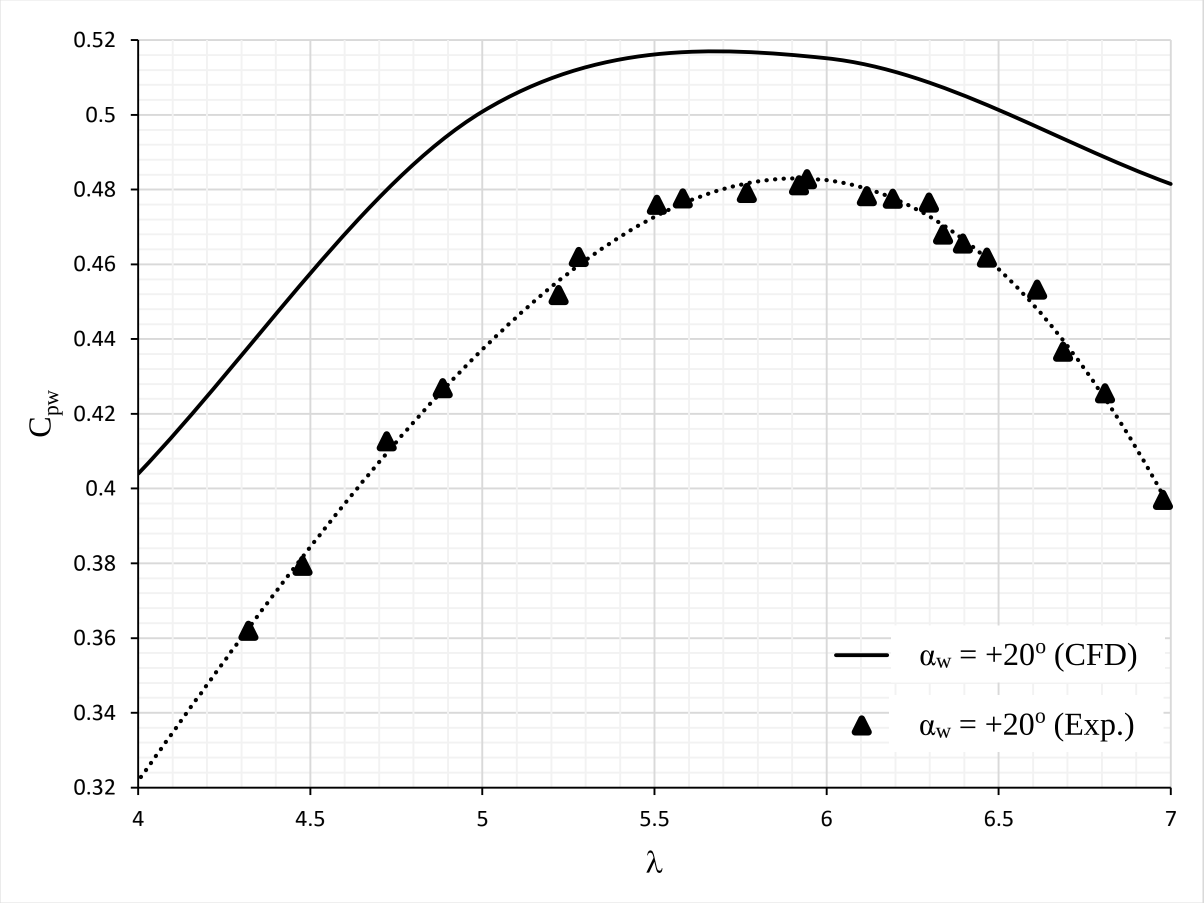

Figure 6.55: Comparisons between experimental values and numerical results for the rotor with WL of α_w=+20° and H=0.8%R

Chapter 7

Conclusions and Recommendations of Future Work

7.1 Conclusions

CFD model for flow in horizontal axis wind turbine has been developed and verified by comparisons with previous experiments and numerical models. The verified model is used to evaluate the effect of WL on the performance of horizontal axis wind turbine. Two main geometrical parameters namely WL height and toe angle are studied (Figure 1.12). In all numerical cases the cant angle is kept constant at 90^o.

The effect of WL height on the performance of wind turbine has been studied using four different values of H namely H=0.8%R, H=2%R, H=4%R and H=8%R with zero toe angle. The results showed that:

- The WL with height H=0.8%R gives the largest enhancement of power. It increases C_{pw} and C_T by 2.4% and 2.9% respectively at $\lambda=7$.
- WL height increase shows negative influence for C_{pw} and increase in C_T at higher values of λ. All WLs with different height succeeded in moving the vortex away from the blade. The WLs with larger height produce extra negative torque that reduces the net power coefficient.
- At higher tip speed ratios the rotor acts as a solid concave body opposite to flow in the case of higher WL heights. Extra higher pressure is concentrated before the rotor and the pressure difference is increased across the rotor as demonstrated by pressure contours and velocity vectors in Figure 6.16 and Figure 6.18. The pressure difference is the main reason for increasing C_T especially at higher values of λ.
- It is concluded from the previous results that the winglet of H=0.8%R with toe angle 0^o shows the highest C_{pw} values and lowest C_T values for all λ values. The velocity vector plots produced by CFD showed that the radial location of vortex core is independent of the WL height. The WL with minimum height namely H=0.8%R with toe angle 0^o performed its function by pushing the tip vortex centre away from the blade tip (Figure 6.18).

- The WL of height equals the tip vortex radius is the optimum one that can be used in the present study.

The effect of WL toe angle has been also numerically studied by considering fixed height 0.8% R. Three upwind and three downwind WLs toe angles are studied. The results showed that:

- The upwind WL of α_w =0^o and H=0.8%R increases C_{PW} and C_T by 2% and 2.3% respectively at λ=4 and by 2.4% and 2.9% at λ=7.
- The maximum improvement in C_{PW} is achieved by using upwind WL with α_w = +20^o and H=0.8%R. Since, C_{PW} and C_T are increased by 2% and 4.6% respectively at λ=4 and by 6 % and 9.8 % at λ=7. Further increase of positive toe angle does not improve C_{PW}. On contrary it causes a decrease of C_{PW} for lower tip speed ratios.
- It is found that downwind configurations aren't useful for wind turbine rotor. Downwind WL of α_w =-30^o decrease C_{PW} and C_T by 7% and 4% respectively at λ=7.
- The study proved that toe angle is an excellent parameter which can considerably affect the rotor performance.
- It is concluded that the increase in power coefficient is strongly related to the tip vortex location demonstrated by velocity vector plots produced by CFD.
- The upwind WL (positive toe angle) pushed the tip vortex center away from the blade tip and accordingly it increases the power coefficient while the downwind WL (negative toe angle) kept the vortex center at the blade tip and thus reduces the power coefficient.

The WLs of H=8%R, H=0.8%R at constant α_w=0^o and the others of α_w=+20^o, α_w=-30^o at H=0.8%R are selected for the numerical wake studies. The wake study focuses on three parameters namely velocity deficit, Reynolds's shear stress and tip vortices vorticity. It is found that:

- The WL of α_w=+20^o increases the velocity deficits by comparison to the rotor without WL as a result for thrust increase.
- It causes a higher Reynolds shear stress along the downstream distance up to X/R =5.4 at the mixing region by comparison to the other WLs.

- The decrease in the shear stress is a result of the increase in tip vortices vorticity at the same downstream positions by comparison to the rotor without WL.
- The results with WL of $\alpha_w=+20^o$ have the best effect on the wake, since higher Reynolds shear stress increases the chances for wake re-energizing.

Experiments are performed on the four selected WLs as a sample for CFD results verification. The results verify the effect of the tested WLs on the rotor performance. The rotor with WL of $\alpha_w=+20^o$ and H=0.8%R shows the same percent of power enhancement (6%) that is evaluated by present CFD results.

7.2 Recommendations of Future Work

- It is suggested to use WLs with different airfoil sections since, they play a crucial role in vortex formation and affect vortex diameter.
- The extension of the present model to simulate larger turbines is needed since it is expected that winglets are more effective for larger turbines.
- The extension of the present model to include the far wake region beyond X/R=5.4 is needed since the present results showed that the effect of winglet geometry exists in the far wake region.
- PIV could produce further information of the winglet effects on tip blade vortices and the turbine wake.

References

[1] IRENA, "Renewable Energy Outlook: Egypt," International Renewable Energy Agency, Abu Dhabi, 2018.

[2] A. Abdulrahman, "Computational and Experimental Study on Innovative Horizontal-Axis Wind Turbine Blade Designs," M.Sc. Thesis, The University Of Wisconsin-Milwaukee, Milwaukee, 2015.

[3] E. W. Golding, The Generation of Electricity by Wind Power, London, 1976.

[4] J. F. Manwell, J. G. McGowan and A. L. Rogers, Wind Energy Explained: Theory, Design and Application, John Wiley & Sons, 2002.

[5] Sandia National Laboratories, "Sandia Labs News Releases," 30 July 2012. [Online]. Available: https://share.sandia.gov/news/resources/news_releases/vawts.

[6] T. Burton, D. Sharpe, N. Jenkins and E. Bossanyi, Wind Energy Handbook, John Wiley & Sons, 2001.

[7] H. P. Blomhoff, "An Experimental Investigation of Wind Turbine Wakes," M. SC., Norwegian University of Science and Technology, 2012.

[8] B. Sanderse, "Aerodynamics of Wind Turbine Wakes," Energy Research Center of the Netherlands, 2009.

[9] S. B. Mattos, P. A. Macedo and H. D. Filho da Silva, "Considerations about Winglet Design," in *21st Applied Aerodynamics Conference,* Orlando, Florida, 2003.

[10] A. Farhan, A. Hassanpour, A. Burns and Y. G. Moltagh, "Numerical study of effect of winglet planform and airfoil on a horizontal axis wind," *Renewable Energy,* vol. 131, pp. 1255-1273, 2018.

[11] M. D. Maughmer, "Design of Winglets for High-Performance Sailplanes," *Journal of Aircraft,* vol. 40, no. 6, pp. 1099-1106, 2003.

[12] A. M. Berhe, "Aerodynamic Analysis of Finite-Span Wings," Msc. Thesis, McGill University, Montréal, Québec, 2003.

[13] G. W. Gyatt and P. B. S. Lissaman, "Development and Testing of Tip Devices for Horizontal Axis Wind Turbines," National Aeronautics and Space Administration , Cleveland, Ohio, 1985.

[14] G. Van Bussel, "A Momentum Theory for Winglets on Horizontal Axis Wind Turbine Rotors and some Comparison with Experiments," in *Fourth IEA Symposium on the Aerodynamics of Wind Turbines,* Rome, Italy, 1990.

[15] H. Imamura, H. Hasegawa and K. Kikuyama, "Numerical Analysis of the Horizontal Axis Wind Turbine with Winglets," *JSME International Journal,* vol. 41 Series B, pp. 170-176, 1998.

[16] M. Gaunna and J. Johansen, "Can Cp be increased by the used of winglets? - or - A Theoritical and Numerical Investigation of the Maximum Aerodynamic Efficiency of Wind Turbine Rotors with Winglets," in *46th Aerospace Sciences Meeting and Exhibit*, Reno, Nevada, 2008.

[17] J. Johansen and N. N. Sørensen, "Numerical analysis of winglets on wind turbine blades using CFD," in *European Wind Energy Conference and Exhibition*, 2007.

[18] P. M. Congedo and M. G. De Giorgi, "Optimizing of a wind turbine rotor by CFD modeling," in *2008 ANSYS Italian Conference: Inspiring Engineering and Sciences*, Venice, 2008.

[19] A. Gupta and R. Amano, "CFD analysis of wind turbine blade with winglets," in *ASME 2012 International Design Engineering Technical Conferences and Computers and Information in Engineering Conference*, Illinois, 2012.

[20] P. Saravanan, K. M. Parammasivam and S. Selvi Rajan, "Experimental Investigation on Small Horizontal Axis Wind Turbine Rotor using Winglets," *Journal of Applied Science and Engineering,* vol. 16, no. 2, pp. 159-164, 2013.

[21] D. Gertz, D. A. Johanson and S. Nigel, "Comparative Measurements of the Effects of a Winglet on a Wind Turbine," *Wind Energy - Impact of Turbulence,* vol. 2, pp. 121-126, 2014.

[22] M. A. Elfarra, N. S. Uzol and I. S. Akmandor, "Investigations on blade tip tilting for Hawt rotor blades using CFD," *International journal of green energy,* vol. 12(2), pp. 125-138, 2015.

[23] A. Ali, H. Chowdhury, B. Longanathan and F. Alam, "An Aerodynamic Study of a Domestic Scale Horizontal Axis Wind Turbine with Varied Tip Configurations," *Procedia Engineering*, vol. 105, pp. 757-762, 2015.

[24] N. Tobin, A. M. Hamed and L. P. Chamorro, "An Experimental Study on the Effects of Winglets on the Wake and Performance of a Model Wind Turbine," *Energies,* vol. 8, pp. 11955-11972, 2015.

[25] V. Klimchenko and A. R. Jones, "An Experimental Study of the Effects of Winglets and Serrations on the Wake of a Wind Turbine," in *53rd AIAA Aerospace Sciences Meeting*, Kissimmee, Florida, 2015.

[26] T. H. Hansen and F. Mühle, "Winglet Optimization for a Model-Scale Wind Turbine," *Wind Energy,* pp. 1-16, 2018.

[27] F. Zahle, N. N. Sørensen, M. K. McWilliam and A. Barlas, "Computational Fluid Dynamics-Based Surrogate Optimization of a Wind Turbine Blade Tip Extension for Maximising Energy Production," *Journal of Physics,* vol. 1037, pp. 1-10, 2018.

[28] Y. Ostovan, M. T. Akpolat and O. Uzol, "Experimental Investigation of the Effects of Winglets on the Tip Vortex Behaviour of a Model Horizontal Axis Wind Turbine using Particle Image Velocimetry," *Journal of Solar Energy Engineering*, pp. 1-34, 2018.

[29] B. Zhu, X. Sun, Y. Wang and D. Huang, "Performance characteristics of a horizontal axis turbine with fusion winglet," *Energy*, vol. 120, pp. 431-440, 2017.

[30] M. Khaled, M. M. Ibrahim and H. E. Abdel Hamed, "Investigation of a small horizontal-axis wind turbine performance with and without winglet," *Energy*, vol. 187, 2019.

[31] M. G. Khalafallah, A. M. Ahmed and M. K. Emam, "The effect of using winglets to enhance the performance of swept blades of a horizontal axis wind turbine," *Advances in Mechanical Engineering*, vol. 11, no. 9, pp. 1-10, 2019.

[32] F. Massouh and I. Doberv, "Exploration of the Vortex Wake behind of Wind Turbine Rotor," *Journal of Physics*, pp. 1-9, 2007.

[33] L. Vermeer, J. N. Sørensen and A. Crespo, "Wind turbine wake aerodynamics," *Progress in aerospace sciences*, vol. 39(6), pp. 467-510, 2003.

[34] I. Grant, M. Mo, X. Pan, P. Parkin, J. Powell, H. Reinecke, K. Shuang, F. Coton and D. Lee, "An Experimental and Numerical Study of the Vortex Filaments in the Wake of an Operational Horizontal-Axis Wind Turbine," *Wind Engineering and Industrial Aerodynamics*, vol. 85, pp. 177-189, 2000.

[35] J. P. Xiao, J. Wu, L. Chen and Z. Y. Shi, "Particle Image Velocimetry (PIV) Measurements of Tip Vortex Wake Structure of Wind Turbine," *Applied Mathematics and Mechanics*, vol. 32, pp. 729-738, 2011.

[36] H. Snel, J. G. Schepers and B. Montgomerie, "The MEXICO Project (Model Experiments in Controlled Conditions): The Database and First Results of Data Processing and Interpertation," *Journal of Physics*, vol. Conference Series 75 012014, 2007.

[37] H. Snel, R. Houwink and J. Bosschers, "Sectional Prediction of Lift Coefficients on Rotating Wind Turbine Blades in Stall," Netherlands Energy Research Foundation Petten, Netherlands, 1994.

[38] C. Zhang, "Aerodynamic, Structural and Aero-elasticity Modelling of Large Composite Wind Turbine Blades," Ph. D. Thesis, Loughborough University, London, 2013.

[39] C. E. Carcangiu, "CFD-Rans study of horizontal axis wind turbines," Ph.D. Thesis, University of Cagliari, Cagliari, Italy, 2008.

[40] W. Z. Shen, R. Mikkelsen, J. N. Sørensen and C. Bak, "Tip loss corrections for wind turbine computations," *Wind Energy*, vol. 8(4), pp. 457-475, 2005.

[41] A. Jimenez, A. Crespo, E. Migoya and J. Gracia, "Advances in Large-Eddy Smulation of a Wind Turbine Wake," *Journal of Physics*, vol. Conference Series 75 , pp. 1-13, 2007.

[42] S. WuBow, L. Sitzki and T. Hahm, "3D-Simulation of the Turbulent Wake behind a Wind Turbine," *Journal of Physics*, vol. Conference Series 75, pp. 1-8, 2007.

[43] C. J. Davis, "Computational Modeling of Wind Turbine Wake Interactions," M.Sc Thesis, Colorado State University, Fort Collins, Colorado, 2012.

[44] M. Bastankhah and F. Porté-Agel, "A new Analytical Model for Wind-Turbine Wakes," *Renewable Energy*, vol. 70, pp. 116-123, 2014.

[45] J. The and H. Yu, "A critical Review on the Simulations of Wind Turbine Aerodynamics Focusing on Hybrid RANS-LES Methods," *Energy,* vol. 138, pp. 257-289, 2017.

[46] G. J. W. Van Bussel, S. Mertens, H. Polinder and H. F. A. Sidler, "TURBY®:concept and realisation of a small VAWT for the built environment," Delft, Netherlands, 2004.

[47] "ANSYS FLUENT 15.0 Theory Guide," ANSYS Inc., 2009.

[48] H. K. Versteeg and W. Malalasakera, "An Introduction to Computational Fluid Dynamics: The Finite-Volume Method," Harlow: Longman Scientific & Technical, New York, 1995.

[49] F. R. Menter, "Zonal two equation k-ω turbulence models for aerodynamic flows," in *23rd Fluid Dynamics, Plasmadynamics and Lasers Conference*, Orlando, Florida, 1993.

[50] M. Lee, Y. C. Shiah and C. Bai, "Experiments and numerical simulations of the rotor-blade performance for a small-scale horizontal axis wind turbine," *Journal of Wind Engineering and Industrial Aerodynamics,* vol. 149, pp. 17-29, 2015.

[51] "UIUC airfoil coordinates database," University of Illinois, [Online]. Available: https://m-selig.ae.illinois.edu/ads/coord_database.html.

[52] P. D. Clausen and D. H. Wood, "Research and development issues for small wind turbines," *Renewable Energy,* vol. 16, no. 1-4, pp. 922-927, 1999.

[53] P. Giguere and M. S. Selig, "Low Reynolds number airfoils for small horizontal axis wind turbines," *Wind Engineering,* vol. 21, pp. 367-380, 1997.

[54] P. Giguere and M. S. Selig, "New airfoils for small horizontal axis wind turbines," *Wind Engineering,* vol. 120, 1998.

[55] S. J. Miley, "A catalog of low Reynolds number airfoil data for wind turbine applications," College Station: Department of Aerospace Engineering, Texas, 1982.

[56] P. S. Lissaman, "Low-Reynolds-number airfoils," *Annual Reviews of Fluid Mechanics* , vol. 15, pp. 223-239, 1983.

[57] M. Z. IQBAL and A. CHAN, "A study of the effect of element types on flow and turbulence characteristics around an isolated high-rise building," in *Eleventh International Conference on CFD in the Minerals and Process Industries*, Melbourne, Australia, 2015.

[58] M. Peri, "Simulation of flows in complex geometries: New meshing and solution methods," in *NAFEMS Seminar: Simulation of Complex Flows (CFD)*, 2004.

[59] R. V. Garimella, J. Kim and M. Berndt, "Polyhedral mesh generation and optimization for non- manifold domains," in *Proceedings of the 22nd International Meshing Roundtable*, 2014.

[60] "candhsurplus," Ametek, [Online]. Available: https://candhsurplus.com/2005catalog/02-dc-motors.pdf.

[61] D. Micallef, B. Akay, C. S. Ferreira, T. Sant and G. Bussel, "The origins of a wind turbine tip vortex," *Journal of Physics: Conference Series 555,* pp. 1-13, 2014.

[62] B. Maalouf, I. Dobrev and F. Massouh, "Vortex Structure in the Wake of a Wind Turbine Rotor," in *19eme Congres Francais de Mecanique*, Marseille, 2009.

[63] M. C. Queirolo, "Impact of morphing winglets on aircraft performance," M.Sc. Thesis, Delft University of Technology, 2018.

[64] P. K. Jha, E. P. N. Duque, J. L. Bashioum and S. Schmitz, "Unraveling the Mysteries of Turbulence Transport in a Wind Farm," *Energies,* vol. 8, pp. 6468-6496, 2015.

[65] S. J. Kline and F. A. McClintock, "Describing Uncertainties in Single-Sample Experiments," *Mechanical Engineering,* vol. 3, 1953.

[66] D. C. Maniaci and M. D. Maughmer, "Winglet Design for Wind Turbines Using a Free-Wake Vortex Analysis Method," in *50th AIAA Aerospace Sciences Meeting including the New Horizons Forum and Aerospace Exposition*, Nashville, Tennessee, 2012.

[67] M. Elfarra, "Horizontal Axis Wind Turbine Rotor Blade: Winglet and Twist Aerodynamic Design and Optimization Using CFD," Graduate School of Natural and Applied Sciences of Middle East Technical University, Ph.D. Thesis, 2011.

Appendix A
Uncertainty Analysis

A.1 Introduction

It is well known that the exact value of any independent or dependent variable is difficult to be measured. The difference between the measured one of any variable and its true (exact) value is defined as the uncertainty or the expected e.

Accumulation of the errors involved in calculating any parameter will cause the deviation of the final results from the actual ones. A more precise method of estimating uncertainty in experimental results has been presented by Kline and McClintock [65]. The method is based on carful specification of the uncertainties in the various primary experimental measurements, suppose the result dependent (R) is a given function of the independent variables

(x_1, x_2 , x_3, x_4 ,……………. ……………..x_n) .

Thus:

R= f (x_1, x_2, x_3, x4, ……x_n)

Let WR is the uncertainty in the result and w_{x1}, w_{x2}, w_{x3}, w_{x4}, w_{xn} are the uncertainties of the independent variables. The uncertainty in the result is given as:

$$WR=\pm\sqrt{(\frac{\partial R}{\partial x_1}wx_1)^2+(\frac{\partial R}{\partial x_2}wx_2)^2\ldots\ldots\ldots\ldots\ldots\ldots\ldots.+(\frac{\partial R}{\partial x_n}wx_n)^2} \quad (A.1)$$

A.2 Uncertainty in Power Coefficient (WC_{pw})

The experimental power coefficient is calculated based on the measured electrical current and voltage as mentioned before by the following equation.

$$C_{pw} = \frac{I\,V}{\eta_{mt}(0.5\rho A U_{\infty}^{3})} \qquad \text{(A.2)}$$

Since,

I : Electrical current (A)

V : Electrical voltage (v)

η_{mt}: Mechanical transmission efficiency = 0.45 (Chapter 5)

Therefore

$$C_{pw} = F\ (I, V, U_{\infty}) \qquad \text{(A.3)}$$

Let WC_{pw} is the uncertainty in the result and WI, WV, WU_{∞} are the uncertainties of the independent variables. The uncertainty in the result is given by

$$WC_{pw}=\pm\sqrt{(\frac{\partial C_{pw}}{\partial I}WI)^2 + (\frac{\partial C_{pw}}{\partial V}WV)^2 + (\frac{\partial C_{pw}}{\partial V}WU_{\infty})^2} \qquad \text{(A.4)}$$

Since the case of WL with α_w=+20° is the optimum case in the study, it is selected to make the uncertainty analysis. The experiment no. 19 in Table 6.4 is considered in the calculations due to the maximum power that is recorded.

The relative uncertainty of the measuring devices are $\frac{WI}{I} = \pm 2\%$, $\frac{WV}{V} = \pm 0.5\%$ and $\frac{WU_{\infty}}{U_{\infty}} = \pm 0.3\%$.

Therefore,

I = 2.31 ±0.0462 A

V = 22.5 ±0.1125 V

U_{∞} = 8 ±0.024 m/s

Hence,

$WC_{pw} = \pm 0.01$